The Effect of Electro-Magnetic Stirring on the Weld Microstructure of Aluminium Alloys

Master's Thesis

B. Yudharto Yudodibroto

August 2000

Supervisor: Dr. Ir. M.G. Mousavi
Dr. Ir. M.J.M. Hermans
Professor: Prof. Dr. G. den Ouden

Delft University of Technology
Department of Applied Sciences
Laboratory of Materials Science and Engineering
Welding and Non Destructive Testing Section

Abstract

This master's thesis deals with the effect of electro-magnetic stirring (EMS) on the weld metal microstructure during direct current (DC) Tungsten Inert Gas (TIG) welding of aluminium alloys. Applying electro-magnetic stirring during TIG welding produces a Lorentz force, which then leads to rotation of the molten metal in the weld pool. The rotational flow may yield refinement of the weld grain structure. The mechanism of the grain refining due to EMS is believed to be due to the increasing constitutional undercooling, the change in the direction of the maximum temperature gradient and increasing nuclei supply.

In this project the relationship between the weld microstructure and the stirring parameters has been studied. Special attention has been given to the effect of EMS on the weld microstructure of AA6060 and AA6061. Experiments have been carried out by means of the partial penetration Circular Patch Test and full penetration straight welding. Microstructural observation of the welds revealed that the grain refining effect is apparent at a low frequency of stirring and/or high magnetic field strength; but less effective at high stirring frequency and/or low magnetic field strength. It is suggested that these phenomena are related with the fluid flow in the weld pool. This suggestion is supported by the results of temperature measurements of the weld pool. The temperature gradient of the weld pool stirred at high frequency is higher compared to that stirred at low frequency. This indicates that during stirring with low frequency, the fluid flow velocity in the weld pool is higher compared to that with high frequency.

To study the fluid flow in the weld pool, a model of the metal liquid flow in the weld pool based on the Navier-Stokes equation was developed for unidirectional stirring of a stationary welding. By using this model, the fluid flow in the weld pool during alternating stirring can be predicted. The results indeed indicate that the fluid flow velocity in the weld pool during alternating stirring at high frequency is lower than that at low frequency. Based on the results of this approach, further observation of the fluid velocity indicates that the grain

refinement due to EMS during TIG welding takes place when the fluid flow in the weld pool starts to become turbulent.

The thesis is divided into five chapters. Chapter 1 gives a general introduction to the topic and a brief description of the scope of the thesis. In Chapter 2 the theoretical background is discussed. This discussion covers some topics such as aluminium welding, weld solidification, and also the principles as well as the effect of electro-magnetic stirring during welding. Chapter 3 deals with the experimental set-up, calibration and procedures. The experimental work includes the Circular Patch Test, used in the case of partial penetration welding, full penetration straight welding and temperature measurements. The development of the coil used in this project is also presented. In Chapter 4 the results of the experiments are presented and discussed. Besides the experiment results, a mathematical model to predict the fluid velocity in the weld pool is described. Finally, Chapter 5 presents some conclusive remarks and recommendations for future research.

Acknowledgements

During the course of this work I was supervised by Professor G. den Ouden, Dr. M.J.M Hermans and Dr. M.G. Mousavi. I am very grateful for their interests and their encouragement in all respects. I would also like to thank Dr. R. Koekoek for his advice to solve the mathematical problems; W.A.J. Brabander and F.J.A.M. Bosman for their contributions in the laboratory work; and also J.M. Kranenburg (Hans) and all my colleagues in TMC-3 group for their help during my work.

Finally, I am highly indebted to my wife Endang and our daughters Ardia and Rosma for their patience and support over the past years.

Table of Contents

Nomenclature

A	Cross sectional area	mm^2
B	Magnetic induction or magnetic field strength	Tesla (T)
C_0	Initial alloy's composition	wt %
C_L	Concentration of alloying element in liquid phase	wt %
C_S	Concentration of alloying element in solid phase	wt %
d	Welding depth	mm
F_L	Lorentz force	Newton (N)
G	Temperature gradient	$^0C.mm^{-1}$
HI	Heat input	$Joule.mm^{-1}$
i	Coil current	Ampere (A)
I	Welding current	A
j	Current density	$A.m^{-1}$
k	Equilibrium distribution coefficient	-
p	static pressure	Pascal (Pa)
Q	Available energy/heat developed by the heat source	Watt (W)
r	Radius	mm
R	Solidification rate	$mm.s^{-1}$
R	Weld pool radius	mm
R_e	Reynolds number	-
R_h	Hydraulic radius	mm
R_L	Local solidification rate	$mm.s^{-1}$
$s_{\phi(r,t)}$	Fluid velocity in the weld pool at steady state	$mm.s^{-1}$
SQ	Stirring quotient	$cycle.mm^1$
t	time	s
T	Temperature	^0C or ^0K
T_0	Ambient temperature	^0C or ^0K

T_a	Actual temperature in the liquid	^0C or ^0K
T_L	Liquidus temperature according to phase diagram	^0C or ^0K
T_m	Melting Point	^0C or ^0K
$u_{\phi(r,t)}$	Fluid velocity in the weld pool at transient state	$mm.s^{-1}$
U	Arc voltage	Volt (V)
v	Welding travel speed	$mm.s^{-1}$
v	fluid velocity	$mm.s^{-1}$
$v_{\phi(r,t)}$	Fluid velocity in the weld pool	$mm.s^{-1}$
WP	Wetted perimeter	mm
α	Angle between magnetic field vector B and current density vector j	degree (^{0})
α	Angle between the weld centerline and the solidification direction	degree (^{0})
β	Thermal expansion coefficient of the liquid metal	$m^3.K^{-1}$
η	Heat transfer efficiency	percent or %
η	Viscosity	Pa.s
ϕ	Angle between the interface normal and the <100> direction	degree (^{0})
λ_1	Primary dendrite arm spacing	mm
λ_2	Primary dendrite arm spacing	mm
ρ	Mass density	$kg.m^{-3}$
μ	Magnetic permeability	H.m-1
ν_B	Frequency of the magnetic field	Hz
ν_j	Frequency of the welding current density	Hz
ν_s	Stirring frequency	Hz
φ_B	Phase angle of the magnetic field	rad
φ_j	Phase angle of the magnetic field	rad
ω	Number of coil turns	-

Chapter 1. Introduction

The application of electro-magnetic stirring (EMS) during welding has been known for almost four decades. In 1962, Brown et al. [1] found that applying an alternating vertical magnetic field parallel to the arc axis could generate a Lorentz force in the weld pool, which then led to rotation of the molten metal alternatingly. As a result of the alternating rotational flow, grain refinement in the weld metal could be produced. Since then, a number of studies has been carried out on this subject for various metals. Most of these studies showed that the extent of grain refining is dependent upon the strength and the frequency of the alternating magnetic field. These results allow the use of EMS to improve the weld quality since finer grains provide better weld properties, for instance, they reduce the sensitivity to hot cracking.

However, it is still difficult to imply the extent of the industrial application of electro-magnetic stirring to achieve grain refinement [2]. In addition, although already a considerably amount of research has been performed on EMS, only little research has been performed in applying this technique during alternating current (AC) TIG welding of aluminium. Therefore, further study on EMS during welding is necessary.

In this project, the effect of EMS during DC TIG welding of aluminium-magnesium-silicon alloys have been investigated. The work is part of a continuing study in this field carried out at Delft University of Technology and was accomplished in the framework of a sixth-month Master's research project. Besides, it is a new project of the Netherlands Institute for Metals Research (NIMR). A particular aim of this work is to study the relationship between the electro-magnetic stirring parameters (magnetic induction or magnetic field strength as well as stirring frequency) and the weld metal microstructure of AA 6060 and AA 6061. The results may lead to the attainment of the optimum parameter for grain refining, which may satisfy its commercial application.

Recently, Gerritsen [3] has studied the effect of EMS during welding of AA 6082. In his studies, experiments were carried out by using an alternating welding current and an alternating magnetic field both at frequencies of around 50 Hz (this method has been studied earlier by de Vries [4] to weld an aluminium matrix composite). Under these conditions, besides the high-frequency component, which may be too fast for the fluid to follow, a low-frequency component arises, which induces low-frequency stirring. It is interesting to note that in that study EMS refined the grain structure particularly at low travel speed. At a higher travel speed, the effect of EMS was rather worsening the grain structure than improving it. Furthermore, no improved resistance to hot cracking in the case of stirred welds was found.

Since stirring the weld pool under alternating current (AC) TIG welding may produce a more complex phenomenon in the weld pool than that under DC TIG welding, the latter technique was used in this study. Under this condition, the stirring parameters and particularly, the stirring frequency can be accurately controlled. Therefore, an apparent relationship between stirring parameters and weld microstructure can be observed. Moreover, this might show whether high-frequency stirring is really too fast for the weld pool to follow or not. The results can then become a reference to further study the EMS during AC TIG welding.

In addition to the microstructure observations, temperature measurements of the AA 6082 weld pool were also carried out. The results might give an indication about the extent of the fluid mixing in the weld pool and variations of the temperature gradient due to stirring.

To get a better understanding about the fluid flow and its relationship with the stirring parameters, a model of the fluid flow in the weld pool based on the Navier-Stokes equation was developed. In the former study [4], a solution to predict the fluid flow in a stationary weld pool during unidirectional stirring at steady state has been given. In this study, the fluid flow equation of a similar situation (unidirectional stirring) but at the transient state was solved. The results may give a rough estimation about the fluid flow in the weld pool during alternating stirring.

Chapter 2. Theoretical Background

2.1. Introduction

This thesis deals with the influence of electro-magnetic stirring (EMS) on the microstructure of AA 6060 and AA 6061 welds. Therefore, it is necessary to pay attention to several topics relevant to the subject, such as aluminium welding, solidification of the weld metal and EMS. In this chapter, these topics are discussed. Firstly, an overview of TIG welding of aluminium alloys is given. The overview covers a discussion about TIG welding and weldability of aluminium alloys. Subsequently, solidification of weld metal is dealt with, which includes the solidification mechanism as well as the development of the macrostructure and the microstructure of the weld. Finally, the principle of the EMS during welding, its influence on the weld structure and its important parameters are described.

2.2. TIG Welding of Aluminium Alloys

2.2.1. TIG Welding

Tungsten Inert Gas (TIG) welding or Gas Tungsten Arc Welding (GTAW) has become indispensable as a tool for many industries because of the high quality weld produced and the low equipment costs [5]. Since the heat input is low and can be controlled precisely, TIG welding is suitable for welding small parts and thin plates. However, because of the limited heat input, the deposition rate of TIG welding is low [6]. A schematic diagram of the TIG welding set up is shown in Fig. 2.1 [6].

In TIG welding, the metal to be welded is melted by an electric arc. The arc is created between a non-consumable electrode and the workpiece of opposite polarity. If additional metal is required, filler metal can be added through a supplemental source (e.g. filler wire). Inert shielding gas (argon or helium or a mixture of both gases) is used to avoid environmental influence on the weld pool and the electrode. Having an excellent protection on the weld pool

and being a clean process makes that TIG welding can be applied to all metals including reactive metals like aluminium [5].

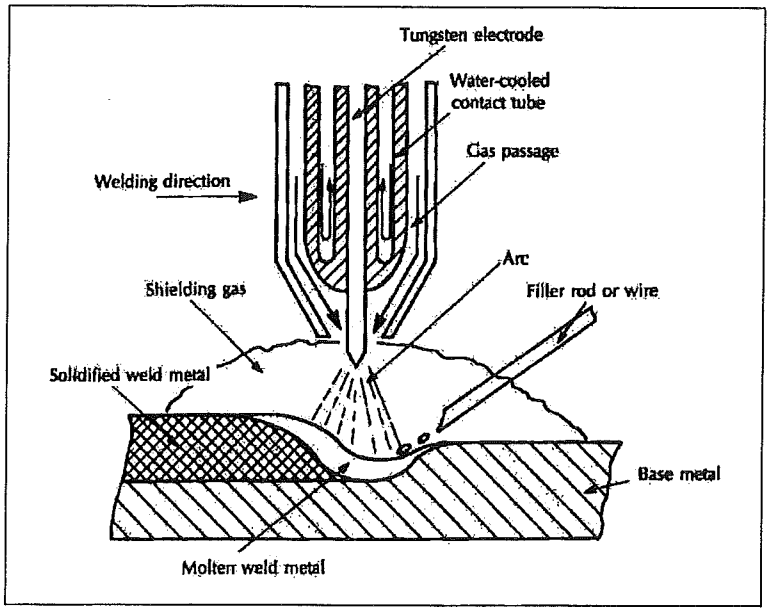

Fig. 2.1. Schematic diagram of TIG welding set up [6].

2.2.2. Weldability of Aluminium Alloys

Among the characteristics of aluminium and its alloys is the presence of a thin oxide film on its surface. This oxide has a high melting point (about 2050°C). Thus, the oxide is virtually insoluble in the molten aluminium, which in turn makes wetting by the molten weld metal difficult [5]. Additionally, since the oxide film is porous, it tends to trap moisture or other gaseous contaminants that can lead to weld porosity [6].

It is well established that the size and the shape of the weld pool depend on the magnitude and distribution of the heat input as well as the dissipation of the heat in the workpiece. In TIG welding, the available heat produced by the source is given by Q = UI, where Q is the energy developed (Watt), U is the arc voltage (Volt) and I is the current (Ampere). As part of the heat is lost to the environment during welding, the heat input to the base metal per unit length is defined by the following equation [6]:

$$HI = \eta \frac{UI}{v} \tag{2.1}$$

where HI is the heat input (Joule/mm), η the heat transfer efficiency (percent) and v the travel speed (mm/s). The influence of these parameters on the weld pool size and shape is depicted in Fig. 2.2. In general a higher heat input leads to a larger weld pool size.

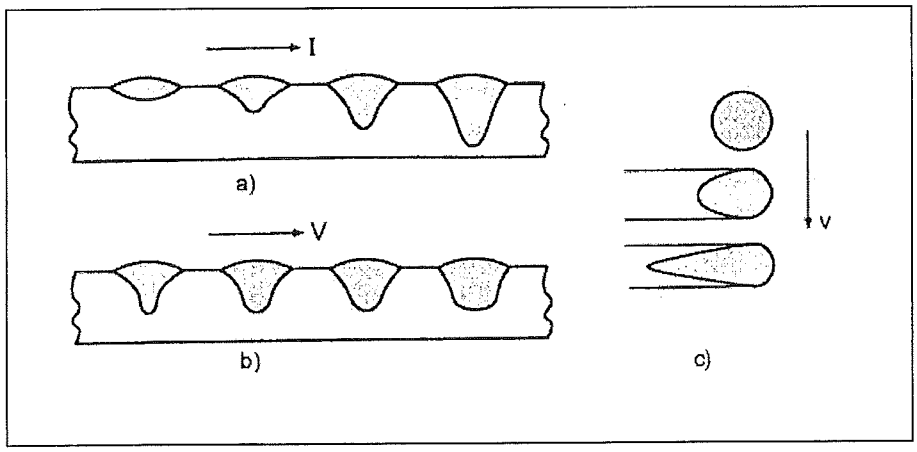

Fig. 2.2. Influence of welding parameter: (a) increasing welding current; (b) increasing voltage and (c) increasing welding travel speed on the weld pool shape [7].

Addition of the alloying elements to aluminium is usually aimed to improve the properties of the aluminium, for instance the mechanical properties. However, these additions may result to poor weldability of the alloy and appearance of welding defects such as hot cracks, liquation, etc. A hot crack, for instance, is a solidification defect, which occurs in the mushy zone trailing the weld pool. It can also be found in the crater where the welding arc is terminated [8]. The effect of the composition of some alloying elements on the crack sensitivity is shown in Fig. 2.3.

From Fig. 2.3, it is evident that the sensitivity to solidification cracking is the greatest at intermediate solute levels. During solidification, the solute is rejected from the solid due to its limited solubility. As a result, a low melting eutectic or solute rich liquid is produced which then forms a continuous film at the grain boundaries. With the presence of stresses such as caused by shrinkage or contraction due to thermal expansion, this film will be ruptured. In pure aluminium there is no low melting-point eutectic present at the grain boundaries, and thus no tendency to

form hot cracks. At much higher solute levels, the amount of low melting liquid is so large that the cracks can be healed. In between, the eutectic liquid is just enough to form the film but not enough to backfill the incipient cracks and therefore give a high tendency to produce hot cracks [9]. Having a higher coefficient of thermal expansion, aluminium alloys exhibit more incidents of hot cracking than mild steel [9].

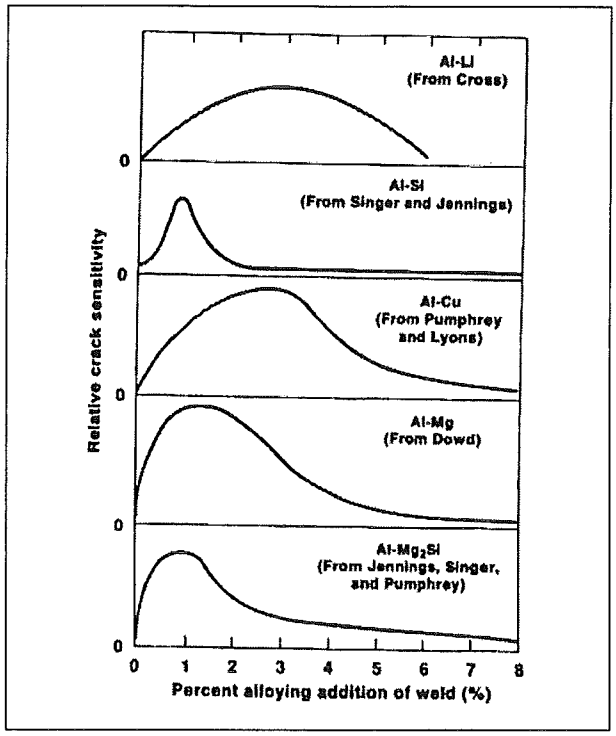

Fig. 2.3. Crack sensitivity of several binary aluminium alloys as a function of alloying element composition [9].

One of the approaches to minimise the susceptibility to hot cracking is by controlling the solidification structure, i.e. by refining the grain. As far as hot cracking is concerned, fine equiaxed grains are preferred over coarse columnar grains for several reasons. First, fine equiaxed grains have a greater ability to deform to accommodate contraction stresses. Second, more effective liquid feeding to the crack in fine-grained materials promotes healing. And third, the concentration of low melting point segregates is spread in a wider area as the area fraction of fine grains is larger than that of coarse grains, reducing the possibility of hot cracking to take place [9].

2.2.3. Welding of Aluminium Alloys

DC TIG welding, with electrode negative (DCEN) or electrode positive (DCEP), and AC TIG welding can be used to weld aluminium and its alloys. In DCEN mode, electrons are emitted from the electrode towards the workpiece. The electron bombardment generates a considerable heat on the workpiece and results in a deep weld penetration. Additionally, the emission of electron cools the electrode tip and prevents it from melting. To deal with the aluminium oxide layer, the workpiece must be thoroughly cleaned prior to welding [5].

When helium is used as a shielding gas during DCEN, the arc voltage obtained is appreciably higher than that when argon is used. Comparisons of the arc voltage obtained with helium and argon as a gas shielding is given in Fig. 2.4.

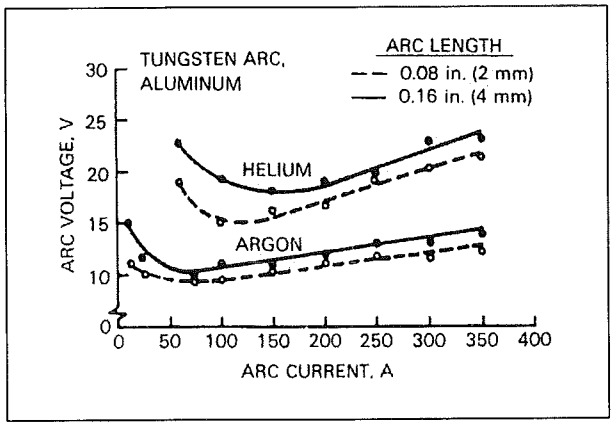

Fig. 2.4. Voltage-Current relationship with argon and helium as a gas shielding [5].

Following equation 2.1, helium offers more available heat to melt the metal compared to argon. The higher available heat favours the use of helium for welding thick or high thermal conductivity materials with DCEN. The disadvantage of helium is that its cost is higher compared to argon. Besides, since helium is lighter than either air or argon, the flow of helium must be about two or three times than that of argon to produce equivalent shielding effectiveness [5].

In DCEP mode, bombardment of large positive ions on the metal surface can easily remove the oxide layer. However, the penetration is shallower than in the case of DCEN.

Furthermore, the electrode in DCEP mode is heated by the bombardment of electrons. To prevent the electrode from melting, a larger electrode diameter or a lower welding current should be used. The shallower weld penetration and the limited heat input of DCEP make this technique suitable for welding sheet metals [5].

By using AC current the effects of DCEN and DCEP are combined. During the positive cycle of the current, the metal will be cleaned and during the negative cycle a deep weld penetration is obtained. Therefore, AC TIG welding is more favourable for aluminium welding [5].

2.3. Weld Metal Solidification

2.3.1. Solidification Mechanism

The transformation from liquid to solid may occur by a process of nucleation and growth. In fusion welding, the growth mechanism is dominant since a solid-liquid interface is always present. This mechanism may start by epitaxial growth from the fusion boundary and proceeds toward the weld centreline. During this process, the existing crystalline structure in the solid is extended with atoms from the melt without altering the crystallographic orientation [10].

As the grains grow into the bulk of the weld pool, their structure is controlled by a different mechanism known as competitive growth. Two factors influence the competitive growth mechanism, the temperature gradient and the easy growth direction. A higher temperature gradient indicates a higher heat removal and thus a higher driving force for solidification. Since the maximum temperature gradient exists in the direction perpendicular to the weld pool boundary, the grains tend to grow in this direction. In addition, individual grains tend to grow parallel to their crystallographic easy-growth directions. In cubic metals like aluminium, this is the <100> direction. Consequently, grains whose easy growth direction is parallel to the direction of the maximum temperature gradient will outgrow and crowd out other grains. Fig. 2.5.a illustrates both the epitaxial and the competitive growth mechanisms [10].

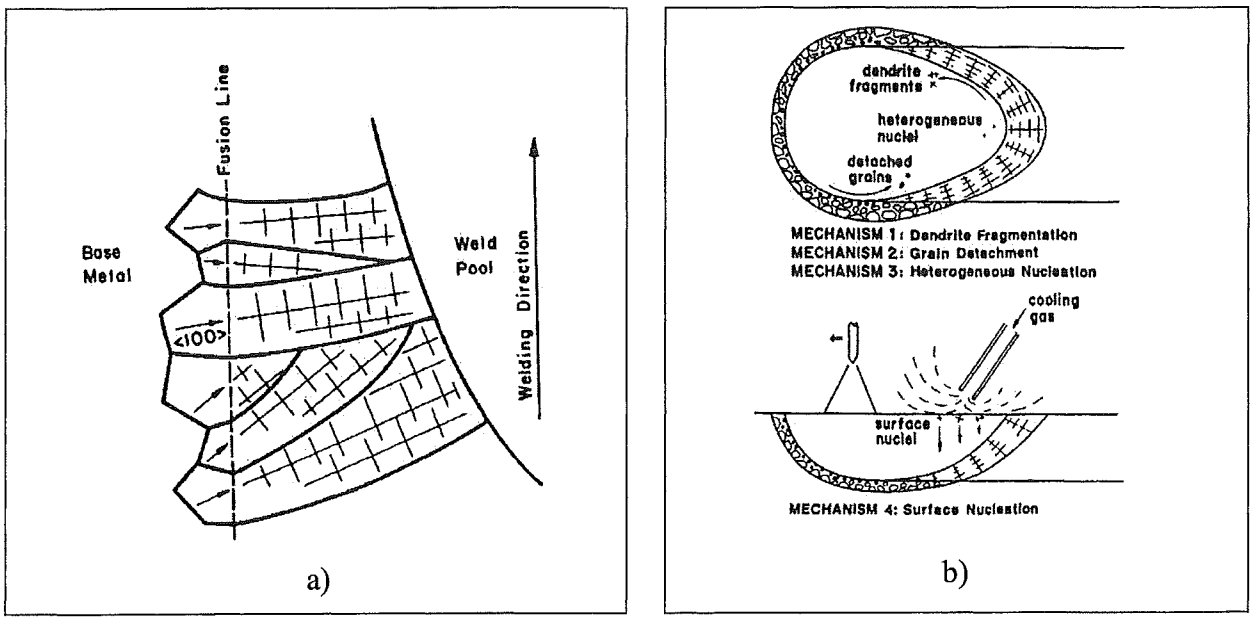

Fig. 2.5. a) Epitaxial and competitive growth and b) Nucleation during weld solidification [10].

As the solidification proceeds, new grains may nucleate, grow into the bulk weld metal and block the columnar grains that grow epitaxially from the fusion boundary. The higher the nucleation rate the finer the new grains formed. The nuclei in weld metal can be formed by several mechanisms: (1) dendrite fragmentation, (2) grain detachment, (3) heterogeneous nucleation and (4) surface nucleation. Fig. 2.5.b shows schematically these nucleation mechanisms [10].

Dendrite fragmentation can in principle be caused by weld pool convection. This process can take place in the mushy zone, the area at the trailing edge of the weld pool where the solidification starts. In this process, dendrite arms may break off by fluid flow or by remelting and are carried into the bulk weld pool. If they survive in the weld pool, they can act as nuclei for new grains [10]. It is interesting to note that this mechanism has been referred to most frequently as the grain refining mechanism for weld metals, even though no proof has been found [10].

By similar cause with dendrite fragmentation, grain detachment can occur in the partially melted zone. This zone is the region in the weld pool of an alloy in which the temperature of the base material rises between the liquidus (T_l) and solidus (Ts) lines. Grains in this zone that are

loosely held together by a liquid film can be brought into the bulk weld pool by the convection flow. They can act as nuclei and form new grains if they survive in the weld pool [10, 11].

Heterogeneous nucleation can occur when there is a significant number of foreign particles (inoculants) in the weld pool on which the atoms in the liquid can be arranged to form a crystal structure. Different from heterogeneous nucleation, homogeneous nucleation occurs when the nuclei are formed solely by the atoms of the liquid themselves. In welding, however, the heterogeneous nucleation will occur more easily and long before the homogenous nucleation [9].

Finally, surface nucleation takes place when the weld pool surface experiences a high cooling rate, for instance due to the cooling effect of the shielding gas. In this mechanism, solid nuclei can be formed at the weld pool surface and showers down due to their density, acting as nuclei for new grains [10].

2.3.2. Constitutional Undercooling

Constitutional undercooling plays an important role during solidification of weld metal. This can be explained by using Fig. 2.6.

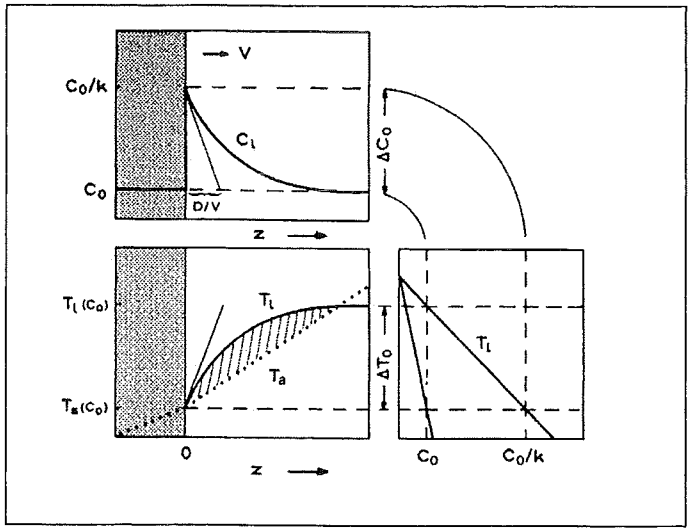

Fig. 2.6. Illustration of constitutional undercooling in solidification of an alloy: (a) solid-liquid interface; (b) phase diagram; (c) constitutional undercooling region shown by the cross hatched area [after ref. 12].

Consider the solidification of an alloy with a composition of C_o. Since the solute solubility is lower in the solid phase, during solidification, there is a substantial increase in the liquid concentration (C_L) ahead of the interface, which then decreases with distance z. If no fluid flow occurs and in the steady state situation, the maximum liquid concentration will be Co/k, where k is equilibrium distribution coefficient (k = Cs/Cl). The increasing concentration in the liquid phase decreases the effective liquidus temperature (T_L). Constitutional undercooling exists when the actual liquid temperature (T_a) is less than the effective liquidus temperature [12].

Commonly, the extent of constitutional undercooling is expressed as a ratio of temperature gradient G to solidification rate R or G/R [10]. A higher G/R value represents a lower constitutional undercooling. Hence, a lower temperature gradient increases the extent of the constitutional undercooling region as is shown in Fig. 2.7.

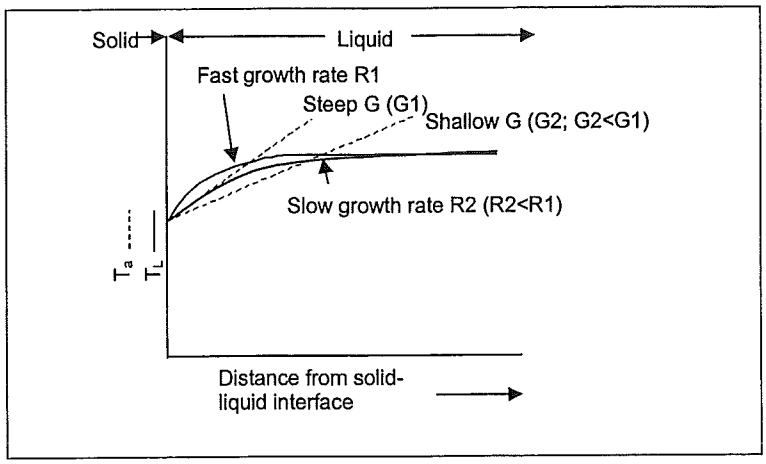

Fig. 2.7. Influence of solidification rate and temperature gradient on the extent of constitutional undercooling [after ref. 13].

Fig. 2.7 also shows that the solidification rate affects the constitutional undercooling by changing the solidification rate R. The faster the solidification rate the steeper the concentration gradient and the effective liquidus temperature [13]. Accordingly the constitutional undercooling is increasing with the solidification rate. In term of the G/R ratio, its value decreases with increasing R. It is well accepted that nominally, the solidification rate can be estimated from its relationship with the welding travel speed V by:

$$R = V.\cos\alpha \tag{2.2}$$

where α is the angle between the centreline of the weld and the solidification direction [13] (see Fig. 2.8.a). A more correct solidification rate during welding can be obtained by regarding the existence of the easy growth directions. Consider now a cubic crystal which grows along the steepest temperature gradient in the weld pool, as shown schematically in Fig. 2.8.b. If ϕ denotes the angle between the interface normal and the <100> direction, the relationship between the nominal growth rate R and the local growth rate R_L as given in equation 2.3 [after 14] exists. The local growth rate of the crystals R_L may then be higher than the nominal growth rate R [14].

$$R_L = \frac{R}{\cos\phi} = \frac{V\cos\alpha}{\cos\phi} \tag{2.3}$$

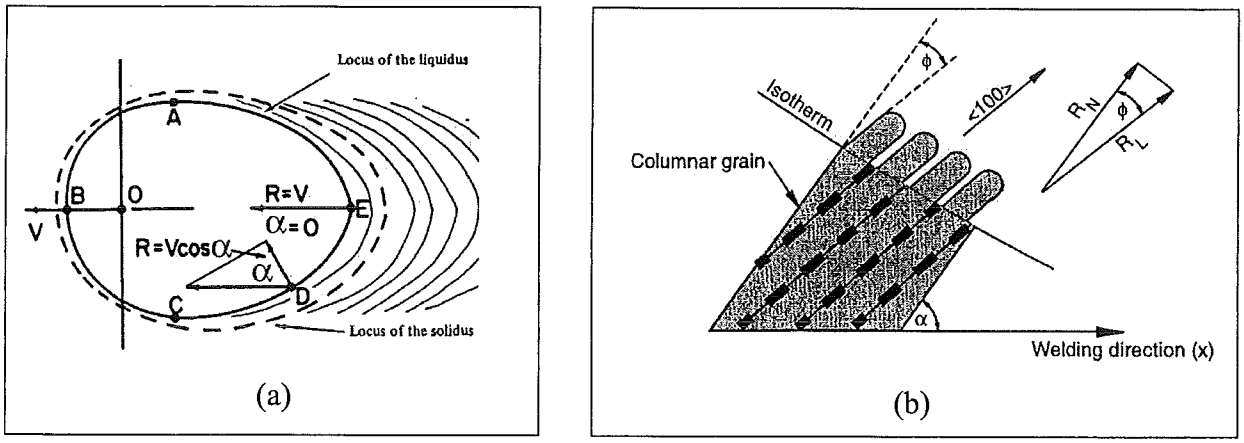

Fig. 2.8. a) Solidification rate R as a function of its position and of the travel speed [13] and b) definition of the local crystal growth rate R_L [14].

2.3.3. Weld Microstructure

During solidification of the weld metal, the solidification front can be planar, cellular or dendritic, depending on the alloying concentration and the degree of constitutional undercooling. The dependency of the grain substructure to the extent of constitutional undercooling parameter G/R and to the alloying concentration is schematically illustrated in Fig. 2.9. The figure shows that the weld substructure changes from planar to dendritic when the degree of the constitutional

undercooling in the weld pool increases. However, constitutional undercooling is not expected to be significant enough by itself to cause nucleation under normal welding conditions [15]. It was proposed that equiaxed grains in the fusion zone originate by a proper nuclei supply aided by constitutional undercooling [10, 16].

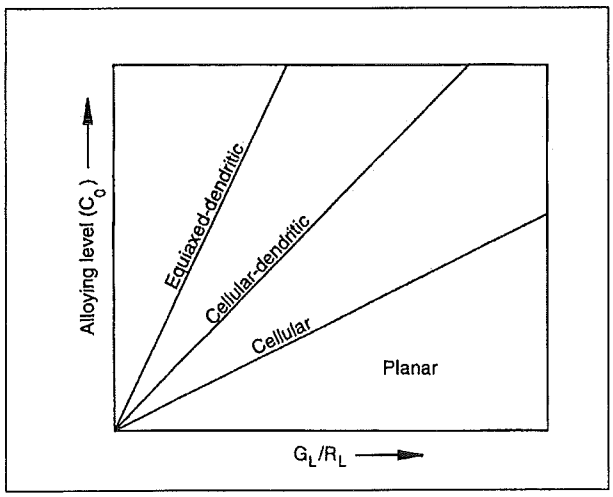

Fig. 2.9. Schematic dependency of the grain substructure on the alloying concentration and the constitutional undercooling [14].

Using equation 2.2, it can be seen that the solidification rate R is 0 at the sides of the pool since $\alpha = 90^{\circ}$ and is maximum at the weld centreline since $\alpha = 0^{\circ}$. On the other hand, the thermal gradient in the liquid (G) is maximum at the side of the pool and is minimum at the weld pool centreline. This situation results in a continuously decreasing G/R ratio from the fusion boundary to the weld centreline. Accordingly, the grain structures can vary from columnar in the fusion boundary to equiaxed in the weld centreline as shown in Fig. 2.10. It is further suggested that for a particular alloy system containing a fixed number of heterogeneous nucleation sites, the columnar to equiaxed transition (CET) occurs when the G/R ratio drops below a certain critical value [14].

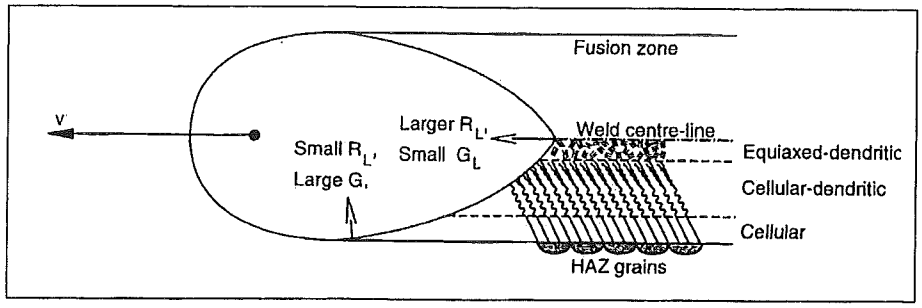

Fig. 2.10. Schematic diagram illustrating structural variations in the weld solidification microstructure across the fusion zone due to the variations of constitutional undercooling (G/R) [14].

As was explained, the formation of equiaxed grains takes place when a significant amount of heterogeneous nuclei is present aided by the constitutional undercooling. An increase in the number of suitable nuclei increases the fraction of the equiaxed region. From Fig. 2.11, it can be seen that, the intersection between the line joining the fusion boundary FB and centreline CL with the CET boundary defines the location of the CET or in other word defines the fraction of equiaxed grains in the weld. As the number of the suitable nuclei increases (N=100), the CET line moves toward the FB, indicates increasing fraction of equiaxed grains [17].

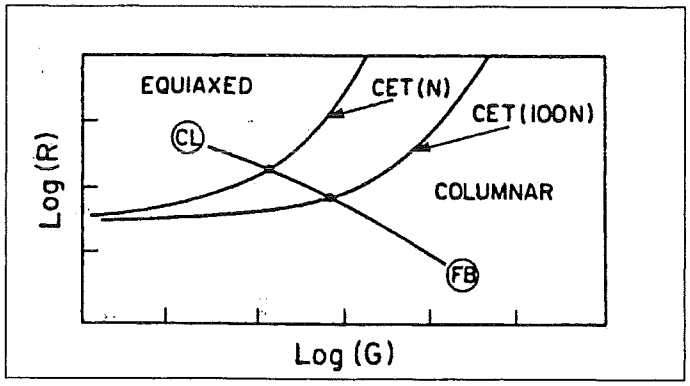

Fig. 2.11. The combined effect of variation of G and R across the fusion zone and the number of suitable nuclei N on the equiaxed fraction. CL = centreline, FB = fusion boundary, CET = columnar to equiaxed transition [17].

While the ratio of G/R governs the mode of solidification, the product of GR controls the scale of the solidification structure. Using a unit of °C/s, the product of GR is equivalent to the cooling rates. The greater the product GR, the finer the grain substructure (cellular, columnar dendritic and equiaxed dendritic structure). This is so because at a slow cooling rate, large dendrite arms can grow at the expense of the smaller ones [9]. The effect of temperature gradient G and solidification rate R on the scale of the grain structure is summarised in Fig. 2.12.

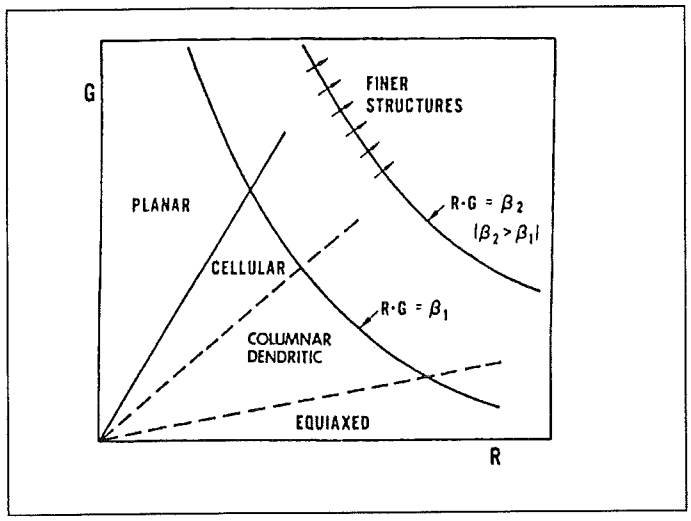

Fig. 2.12. Schematic of influence of the solidification rate R vs. temperature gradient G on the scale of the grain substructure [6].

Characteristic for the dendrite morphology is the dendrite arm spacing. It has been found that the dependence of the spacing of primary dendrite arms λ_1 and of secondary dendrite arms λ_2 on the temperature gradient G and solidification rate R are as follows [18, 14]:

$$\lambda_1 = a_1(G^2R)^{-1/4} \tag{2.4}$$

$$\lambda_2 = a_2(GR)^{-n} \tag{2.5}$$

where a_1 and a_2 are coefficients which depend on the alloy system, and n = 1/3 to 1/2. The definitions of primary and secondary dendrite arm spacing are given in Fig. 2.13.

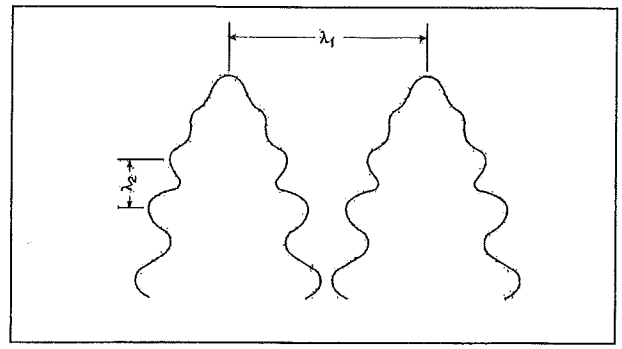

Fig. 2.13. Definition of primary λ_1 and secondary λ_2 dendrite arm spacing [14].

2.3.4. Weld Macrostructure

Fig. 2.14 shows several types of macrostructure that can be developed during solidification of TIG weld in aluminium alloys.

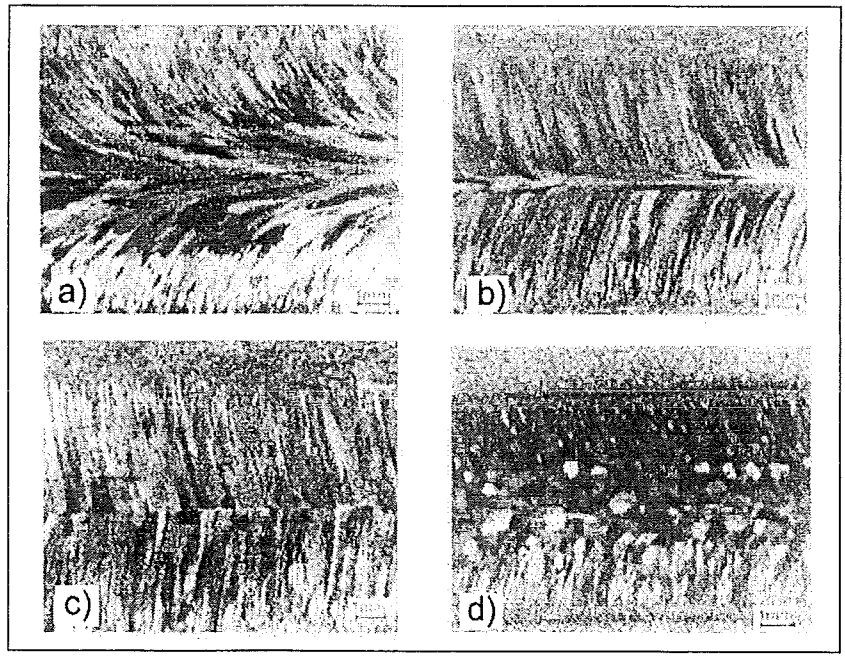

Fig. 2.14. Typical macrostructure of aluminium weld a) stray structure, b) axial structure, c) centreline structure and d) equiaxed structure [19].

It is explained that the formation of these structures is dependent on the welding parameters, particularly the travel speed [19]. At low travel speed, the weld pool shape is

elliptical. Since the epitaxial columnar grains grow in the direction of the maximum temperature gradient, which is perpendicular to the weld pool boundary and continuously changing from the fusion line towards the centreline, a stray structure will be developed. This structure is characterised by curved grains that extend from the fusion boundary and gradually become parallel to the welding direction at the centre of the weld [19].

When the travel speed is faster, the weld pool gets a shape which is somewhere between an ellipse and a teardrop. At this situation, elongated grains can grow along the weld centreline, forming an axial structure. At a very high travel speed, the shape of the weld pool is like a teardrop, so that the direction of the maximum temperature gradient is relatively constant along the weld boundary. As a result, the epitaxial columnar grains grow in a relatively constant direction and can meet in the centre of the weld creating a distinct centreline [19]. Moreover, with increasing travel speed, the solidification rate R is also increasing (equation 2.2) and so is the constitutional undercooling. Aided by proper nuclei, equiaxed structure, in which equiaxed grains scatter in a band along the weld centreline can be formed.

2.4. Electro-magnetic Stirring during TIG Welding

In this section, a discussion about the application of EMS during welding is given. Firstly, the effect of the magnetic field on the weld pool is described, followed by a discussion of the mechanism by which EMS refines the grain structure. After that, the parameters that influence the results of EMS application will be reviewed.

2.4.1. The Principle of Electro-magnetic Stirring during Welding

The principle of EMS during welding is based on the interaction between the welding current and the imposed magnetic field, which generates a Lorentz force. This is shown in Fig. 2.15.

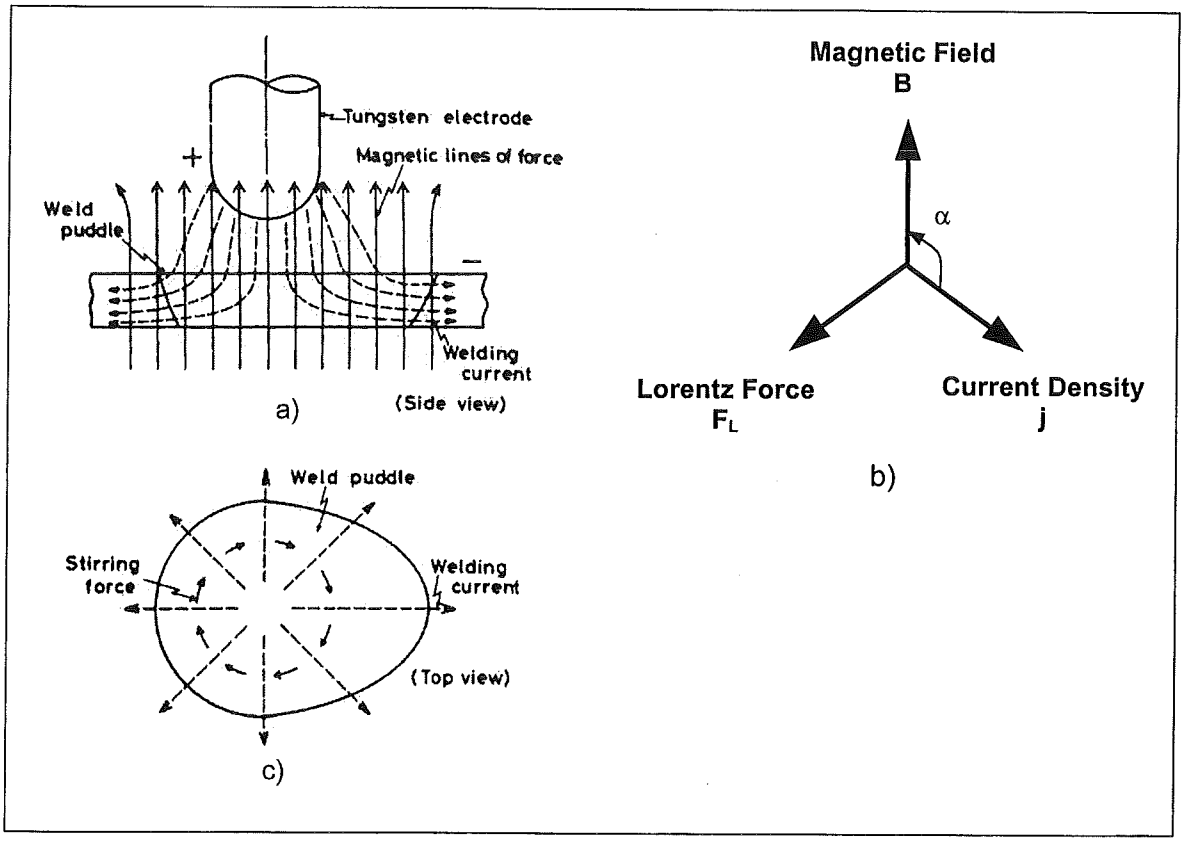

Fig. 2.15. Schematic representation EMS during arc welding (a) the direction of the welding current and the magnetic field; (b) the direction of Lorentz force; (c) annular flow in the weld pool [from 20 and 3].

During TIG welding, the welding current is considered to spread radially in the workpiece. When an external magnetic field is applied axially (the direction of the magnetic field is parallel to the arc axis) a Lorentz force $\vec{F}_L$ is produced and is represented by:

$$\vec{F}_L = \vec{j} \times \vec{B} \qquad (2.6)$$

where $\vec{j}$ is the current density and $\vec{B}$ the magnetic field. The direction of the Lorentz force follows the Fleming's left-hand rule (Fig. 2.15.b), perpendicular to both $\vec{j}$ and $\vec{B}$ towards the direction of a corkscrew when rotated over the smallest possible angle from j axis to B axis. The magnitude of the Lorentz force is represented by:

$$F_L = j.B.\sin\alpha \qquad (2.7)$$

in which α is the smallest angle between the electric current density and the magnetic inductance vectors. Since the electric current flows more horizontally at the weld boundary, α and therefore the magnitude of the Lorentz force is increasing from zero at the weld pool centre to maximum at the weld boundary. However, the Lorentz force in this direction is also reduced due to the divergence of the current in radial outward direction.

2.4.2. The Effects of an Axial Magnetic Field on the Weld Pool Flow

Principally, there are four different forces that drive the convective flow in the weld pool during conventional (unstirred) TIG welding [21]:

1. indigenous electro-magnetic forces or Lorentz forces due to the interaction of the welding current and the induced magnetic field in the weld pool;
2. buoyancy forces due to the density variations of the liquid-metal density caused by the temperature variation in the weld pool;
3. marangoni forces or surface tension forces induced by gradients in temperature and also affected by the addition of surface activating agents such as O, S, Se and Te;
4. aerodynamic drag forces as a result of plasma jet and shielding gas flow along the weld pool surface.

Individually, each driving force leads to either a radial-outward directed flow that results in a relatively wide and shallow weld pool, or a radial-inward flow, which gives a deep and relatively narrow weld pool [21] (see Fig. 2.16).

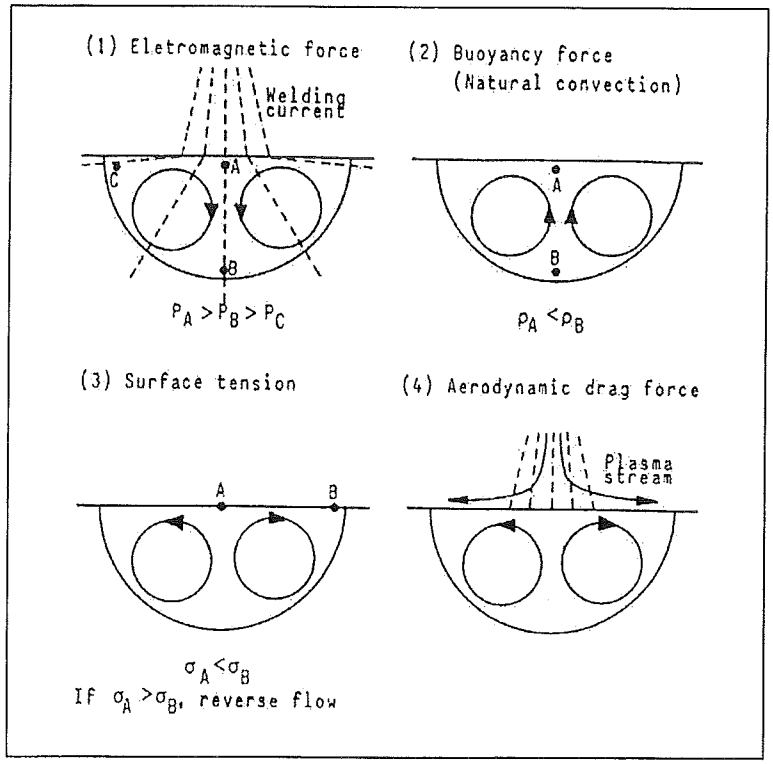

Fig. 2.16. Convection pattern in the weld pool due to: a) self induced electro-magnetic force, b) buoyancy force, c) surface tension and d) aerodynamic drag force [21].

Commonly weld pool convection is a result of the combination of all those four different forces. This gives a very complex convection pattern. Two important equations to simulate the convection in the weld pool are the equation of continuity of mass and the Navier-Stokes momentum equation. For fluids of constant mass density and viscosity, these equations can be presented as follows [22, 23]:

$$\text{Continuity: } \nabla.v = 0 \tag{2.8}$$

$$\text{Momentum: } \rho\left(\frac{\partial v}{\partial t} + v.\nabla v\right) = -\nabla p + \eta\nabla^2 v - \rho\beta g(T - T_0) + jxB \tag{2.9}$$

where v is the fluid velocity, ∇p the static pressure force, $\eta\nabla^2 v$ the viscous force, $\rho\beta g(T-T_0)$ the buoyancy force and jxB the Lorentz force.

Considering cylindrical co-ordinates and neglecting the buoyancy force, the Navier-Stokes equation (equation 2.9) can be expressed in its radial (r), azimuthal (ϕ) and axial (z) components [23]:

Radial (r) component:

$$\rho\left(\frac{\partial v_r}{\partial t} + v_r \frac{\partial v_r}{\partial r} + \frac{v_\phi}{r}\frac{\partial v_r}{\partial \phi} - \frac{v_\phi^2}{r} + v_z \frac{\partial v_r}{\partial_z}\right) = -\frac{\partial p}{\partial r} + \eta \nabla^2 v\big|_r \qquad (2.10)$$

Azimuthal (ϕ) component:

$$\rho\left(\frac{\partial v_\phi}{\partial t} + \frac{v_r}{r}\frac{\partial r v_\phi}{\partial r} + v_z \frac{\partial v_\phi}{\partial z} + \frac{v_\phi}{r}\frac{\partial v_\phi}{\partial \phi}\right) = -\frac{1}{r}\frac{\partial p}{\partial \phi} + j_r x B_z + \eta \nabla^2 v\big|_\phi \qquad (2.11)$$

Axial (z) component:

$$\rho\left(\frac{\partial v_z}{\partial t} + v_z \frac{\partial v_z}{\partial z} + \frac{v_\phi}{r}\frac{\partial v_z}{\partial \phi} + v_r \frac{\partial v_z}{\partial_r}\right) = -\frac{\partial p}{\partial z} + \eta \nabla^2 v\big|_z \qquad (2.12)$$

It can be seen from the last three equations, the only equation that contains the Lorentz force is the one for the azimuthal component. Therefore, in the case of EMS, the Lorentz force causes the liquid in the weld pool to rotate. The rotation can be clockwise or anti-clockwise depending on the direction of the magnetic field and on the welding current. Solving equation 2.11 for a steady state situation (dv/dt=0) with constant B (this means in unidirectional rotation), de Vries [4] concluded that the rotational flow rate can reach a value of 12 m/s. A lower fluid velocity in the weld pool (about 500 mm/s) was estimated by Malinowski et al. [24], based on their experiments. Still, this velocity is higher than the most important self-flow in the weld pool due to the surface tension (about 0.1 m/s). Therefore it is believed that the Lorentz force dominates the self-flow.

2.4.3. Unidirectional Stirring

EMS can provide both a unidirectional and an alternating stirring action. Applying a constant axial magnetic field of sufficient magnitude during DC TIG welding generates unidirectional stirring. By this action the liquid metal is pushed to one side of the weld boundary creating an asymmetrical weld pool shape and a so-called ditch-dike effect (Fig. 2.17). This effect is more pronounced with a stronger magnetic field. Usually the ditch-dike effect is not

wanted and can be solved by using an alternating magnetic field. Regarding the grain refining effect, an investigation by Matsuda et al. [20] leads to a result that unidirectional stirring does not produce grain refinement, except in the case of materials which are very susceptible for grain refinement.

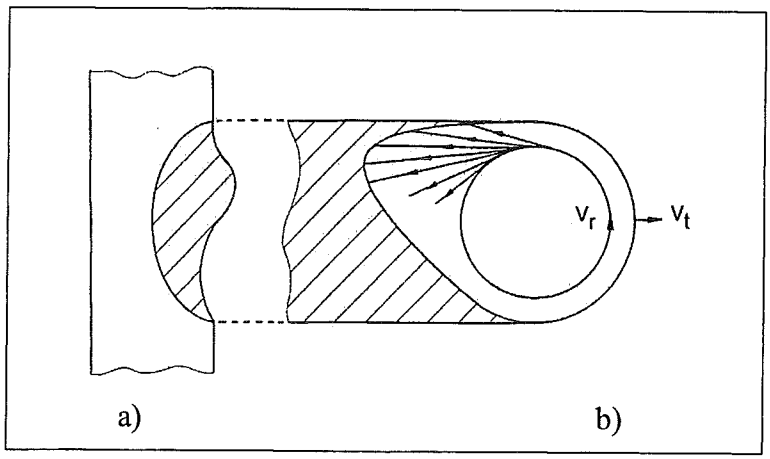

Fig. 2.17. Illustration of the weld pool in the presence of a constant magnetic field, v_t = travel speed; v_r = annular flow velocity of the liquid metal: (a) cross section and (b) top view show the ditch dike effect and the asymmetrical weld pool shape [24].

2.4.4. Alternating Stirring

Alternating rotational flow can be produced when either the magnetic field or the welding current alternates. In this type of flow, the liquid metal is moved to either side of the weld boundary during each half-stirring cycle. With increasing frequency, the ditch-dike effect as well as the asymmetric weld pool shape gradually disappears. Ripples on the weld surface mark this effect. The number of the ripple lines per unit length is dependent on both stirring frequency and welding travel speed, and can be examined using a so-called stirring quotient (SQ) term, which is defined as [3]:

$$SQ = \nu_s / v \tag{2.13}$$

where ν_s is stirring frequency and v travel speed. Fig. 2.18 shows schematically the ripple lines on the weld bead surface due to alternating stirring and the definition of the stirring quotient.

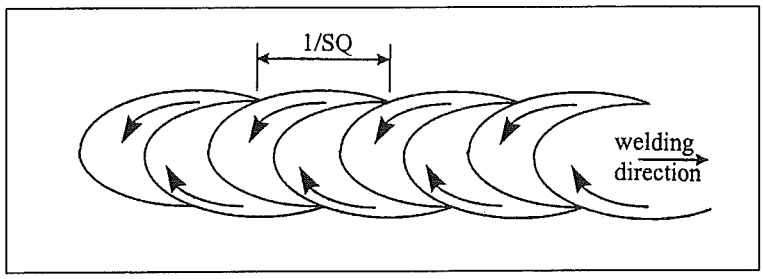

Fig. 2.18. Schematic presentation of the ripple lines on the weld bead surface due to alternating stirring and the definition of stirring quotient [3].

Studies [24, 25] concluded that at a high stirring frequency, the inertia of the liquid metal might hinder the rotational flow. This situation makes the application of magnetic stirring during aluminium welding with alternating current, which commonly works with 50 Hz current, difficult. It is suggested [4] that to solve this problem, an alternating magnetic field which frequency is slightly higher than the current frequency can be used. A solution to calculate the Lorentz force has been developed by using a triangular-wave magnetic field and a square-wave current density. This solution is given in the form of Fourrier series as follows [3, 4]:

$$F_L(t) = jB\sin(\alpha)\frac{32}{\pi^3}\sum_{n=1}\sum_{m=1}\frac{1}{(2n-1)}\frac{1}{(2m-1)^2}\left\{\frac{1}{2}\sin\left[2\pi\left[(2n-1)v_j+(2m-1)v_B\right]t+(\varphi_j+\varphi_B)\right]+\right.$$

$$\left.\frac{1}{2}\sin\left[2\pi\left[(2n-1)v_j-(2m-1)v_B\right]t+(\varphi_j-\varphi_B)\right]\right\} \qquad (2.14)$$

where $F_L(t)$ is the Lorentz force as a function of time, α the smallest angle between the magnetic field and the current density, m and n numerical indices, ν_j the frequency of the welding current, ν_B the frequency of the magnetic field, t the time while φ_j and φ_B are the phase of the welding current and the magnetic field respectively. Equation 2.14 expresses that the Lorentz force consists of sinusoidal waves with a high frequency component ($\nu_j + \nu_B$) and a low frequency component ($\nu_j - \nu_B$). This is depicted in Fig. Fig. 2.19.

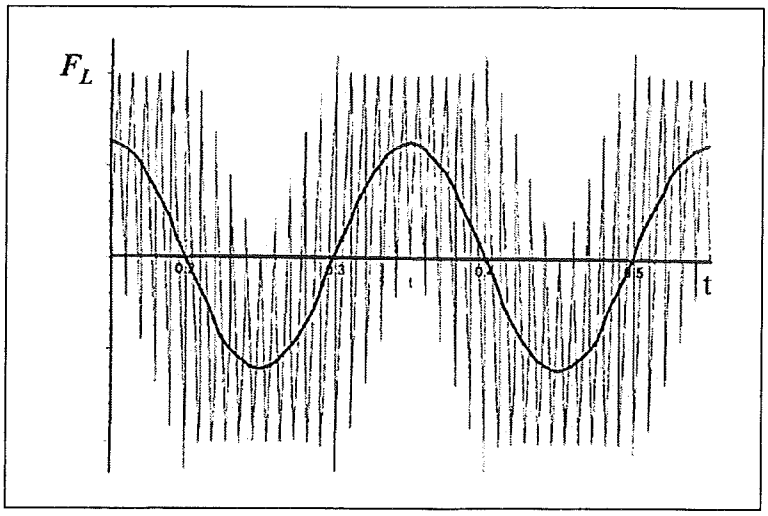

Fig. 2.19. Schematic representation of Lorentz force versus time as a result of interaction between alternating current and alternating magnetic field. The low frequency component is represented by the thick line [3].

If $\nu_j = \nu_B$ and $\varphi_j - \varphi_B = 0$, continuous rotation will be achieved. On the other hand, a slight difference between ν_j and ν_B generates a stirring action on the weld pool with a stirring frequency of $\nu_s = \nu_j - \nu_B$. By taking the magnetic field frequency slightly higher than the current density frequency, an interference of high frequency components of the magnetic field with the current can be prevented [4].

2.4.5. Grain Refinement Mechanism due to EMS during TIG Welding

The alternating rotary flow of the molten metal during EMS in TIG welding favours grain refining by: reducing the temperature gradient, increasing nuclei supply and changing the direction of the steepest temperature gradient.

Investigations [24, 26, 27, 28] suggested that the temperature gradient in the weld pool decreases due to EMS. The decrease of the temperature gradient is associated with the changes of the temperature-distribution in the weld pool. The rotational flow carries the superheated metal to the outer part of the pool and transports the cooler metal to the pool so that the heat will be absorbed as latent heat of melting, creating a larger weld pool. An illustration of weld-pool

temperature changes due to EMS on Kh18N9T steel is shown in Fig. 2.20. Without EMS, the temperature in the centreline of the Kh18N9T steel weld is higher compared to the temperature at the fusion line (Fig. 2.20.b.i). During EMS, the temperature at both locations become equal, representing a reduction of the temperature gradient (Fig. 2.20.b.ii). A lower temperature gradient reduces the G/R ratio and thus increases constitutional undercooling. As has been explained before, with proper nuclei this yields grain refinement.

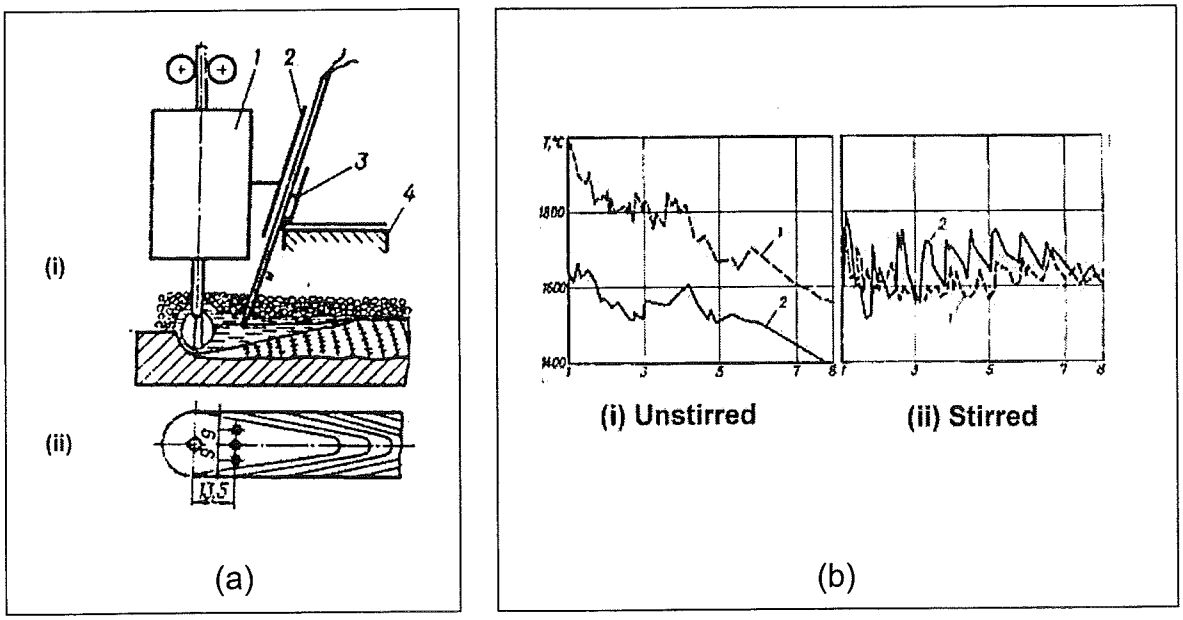

Fig. 2.20. (a) Temperature measurement set-up (i) side view and (ii) top view, 1-welding torch with coil, 2-guides, 3-moving part with thermocouple, 4-stationary part;
(b) Diagram of temperature distribution in the weld pool of Kh18N9T steel during TIG welding (i) without stirring and (ii) with stirring. Line 1 shows the temperature at the weld centreline, while line 2 shows the temperature near the weld pool boundary [27].

In addition to the effect on the constitutional undercooling, EMS is also believed to increase the number of nucleation sites that might be associated with dendrite fragmentation and grain detachment [1, 20, 26]. Both mechanisms have been explained in the previous section. Of these phenomena, Matsuda [20] suggested that the increase in the number of nucleation sites is mainly caused by the fragmentation of cellular dendrite arms. This mechanism has been confirmed in the case of refining ingot casting. However, as the dendrite spacing in weld metals

is finer than in ingot casting, dendrite fragmentation by EMS may be difficult to take place [26]. Fine dendrite spacing makes fluid penetration to the dendrite network difficult. Different from dendrite fragmentation, grain detachment during EMS is more likely to take place [26].

Another way by which EMS may cause grain refining is associated with the directional changes of the steepest temperature gradient in the weld pool. During EMS the hottest metal liquid moves alternatingly along either weld boundary. Thus, each time the liquid flow changes its direction, the direction of the steepest temperature gradient in front of the solidification front will also change accordingly. Since grains prefer to grow along the direction of the maximum temperature gradient, grains will grow until reaching the ripple line, at which, the stirring action changes the direction, and then will be suppressed by new favourably oriented grains. Fine equiaxed grains are produced when the distance between ripple lines is short, or in another word, the grain length is identical with the grain width [20].

2.4.6. Parameters of EMS during TIG Welding

Studies [1, 20, 24, 25, 29, 30] have shown that the result of EMS during TIG welding is affected by several factors, the most important factors being the stirring frequency and the magnetic field strength.

It was found that the optimum stirring frequency for grain refining is proportional to the welding travel speed [20]. This is because at this condition the distance between the ripple lines, which represents the length of the grain structure is equal to the width of the grain. However, it was also found that at high welding travel speed (v=500 mm/min and 1000 mm/min) EMS did not obviously change the microstructure compared to the one in the unstirred weld [20]. This might be due to the formation of a teardrop shaped weld pool at higher travel speed that hinders the stirring at the back of the weld pool [20]. Generally the optimum stirring frequency to obtain grain refining is in the order of 2 to 15 Hz. Using the quantity SQ, Gerritsen [3] found that grain refining of AA6082 called for SQ=2.5 mm^{-1} (ν_s is about 10 Hz). Furthermore, it was observed that the optimum stirring frequency is also dependent on the magnetic field strength and the alloy system [30].

The degree of the grain refinement is increasing with the magnetic field strength. This is most likely due to the increasing Lorentz force (equation 2.8). However, study showed that there is an upper limit of magnetic field intensity, which was found to be about 30 mT, to prevent a burn-through weld bead [20] or a rough weld surface [30]. This upper limit is lower in the case of a slow welding speed and/or a high welding current [20].

2.5. Summary of Current Knowledge

Some topics that are related with EMS during TIG welding of aluminium alloys have been reviewed in this chapter. Based on this review, the following conclusion can be drawn.

1. A finer equiaxed weld structure offers a better resistance to hot cracking than coarser columnar grains.

2. Applying an external axial electro-magnetic field during TIG welding yields a Lorentz force, which leads to rotation of the liquid metal in the weld pool.

3. Unidirectional stirring of the weld pool produces an asymmetrical weld shape as well as a so-called ditch-dike effect.

4. Alternating stirring of the weld pool favours grain refining and diminishes the ditch-dike effect. The optimum stirring frequency for grain refinement has been found to be in the order of 2 to15 HZ, depending on the magnetic field strength. It has also been observed that a higher magnetic field strength is effective to the grain refinement, but there is a limit to prevent a formation of unsound rough weld bead surface or a burn-through.

5. It is believed that alternating stirring of the weld pool during TIG welding favours grain refining by: reducing the temperature gradient, increasing nuclei supply and changing the direction of the steepest temperature gradient.

Chapter 3. Experimental approach

3.1. Materials used

The materials used in this study were AA 6060, 6061 and 6082. All materials were extruded except AA 6061 which was rolled plate. The nominal chemical compositions of these materials are given in Table. 3.1.

Table. 3.1. Chemical composition in % weight of AA 6060, 6061 and 6082.

	Cu	Cr	Fe	Mg	Mn	Ni	Pb	Si	Sn	Ti	Zn
AA 6060[1)]	0.04	<0.01	0.21	0.51	<0.01	<0.01	<0.01	0.38	<0.01	0.02	0.02
AA 6061[2)]	0.15-0.40	0.04-0.35	0.7	0.8-1.2	0.14	...	...	0.4-0.8	...	0.15	0.25
AA 6082 [3)]	0.05	0.01	0.38	0.92	0.65	<0.01	<0.01	0.86	<0.01	0.02	0.01

1) Analysed by using X-ray Fluorescence (Philips PW1480).

2) Data from ref. 31.

3) Data from ref. 3.

The use of AA 6060 in this study is primarily due to its high sensitivity to hot cracking. In addition, AA 6060 represents a low alloy material and thus the grain refining process by electromagnetic stirring can be studied with minimum influence of alloying elements. Therefore, the hot cracks can be well reproduced and the effect of the grain refining on reducing the hot crack sensitivity can be appropriately revealed. In comparison with AA 6060, AA 6061 is less susceptible to hot cracking. In fact the latter alloy is one of the most popular aluminium alloys used for welded structure along with a proper filler wire [32]. Of the three alloys used, according to Mousavi [8], AA 6082 exhibits the least sensitivity to hot cracking. A comparison of the weldability in term of total crack length of AA 6060, 6061, 6082 and two 7xxx series of aluminium alloys by means of the Circular Patch Test (CPT) is given in Fig. 3.1 [8].

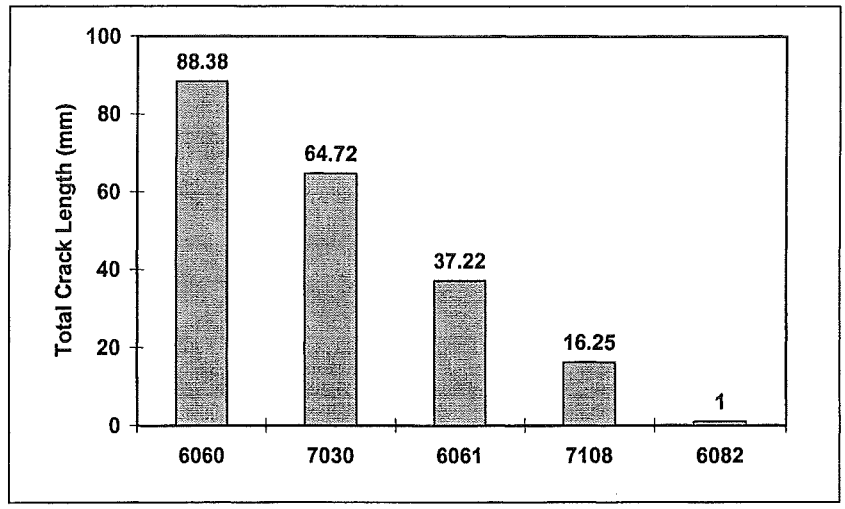

Fig. 3.1. CPT weldability ranking of 5 mm thick commercial aluminium extrusions (except for AA6061, which was a 7 mm cold rolled plate) [8].

Several types of specimen were made with the dimensions given in Table. 3.2.

Table. 3.2. The dimension of the specimens and the applicable experiment.

Specimen	Material	Dimensions (t x w x l) (mm x mm x mm)	Welding experiment
Type 1	AA 6060 - T6	10 x 52 x 52	Circular Patch Test (CPT)
Type 2	AA 6060 as received	10 x 80 x 180	Straight bead on plate – partial penetration
Type 3	AA 6060 T6	3 x 100 x 250	Straight bead on plate – full penetration
Type 4	AA 6061 as stored	15 x 100 x 150	Straight bead on plate – partial penetration
Type 5	AA 6082 as stored	3 x 80 x 200	Temperature measurement – full penetration

The T6 heat treatment (for specimen type 1) was carried out by means of a Heraeus RL200 air circulated oven using the following procedure:

(1) solution heat treating at T = 524°C for 30 min;

(2) quenching in water to room temperature;

(3) precipitation heat treating at T = 185°C for 5 hours;

(4) cooling to room temperature.

Before welding, the type 1 specimens were ground down to grit 600, while other specimens were ground using 120 grit sandpaper.

3.2. Circular Patch Test

In this study a Circular Patch Test (CPT) or more specifically a circular bead weld test method was employed primarily to get reproducible data of the hot cracking susceptibility. Additionally, this method also offers a simple operation and a low cost of fixture and sample production. This intrinsic weldability test relies on a self-restraint induced by the specimen design and fixturing constraint [8].

The procedure followed, consisted of producing an autogenous partial-penetration circular weld (about 340-degree angular movement and 30 mm in diameter). After completion part of the weld, the radial and circumferential strains will reach a maximum though not necessarily simultaneously. At some point, the strain is sufficient enough to initiate a centreline crack. Once initiated, this centreline crack usually propagates behind the weld pool until the welding is terminated. It is assumed that at any instant, the circumferential strains are larger than the radial strains. Therefore, transverse crack should appear before centreline (longitudinal) cracks [33, 34]. Fig. 3.2 shows the CPT apparatus used in this study, while Fig. 3.3 gives the detail dimensions of the apparatus as well as the specimen.

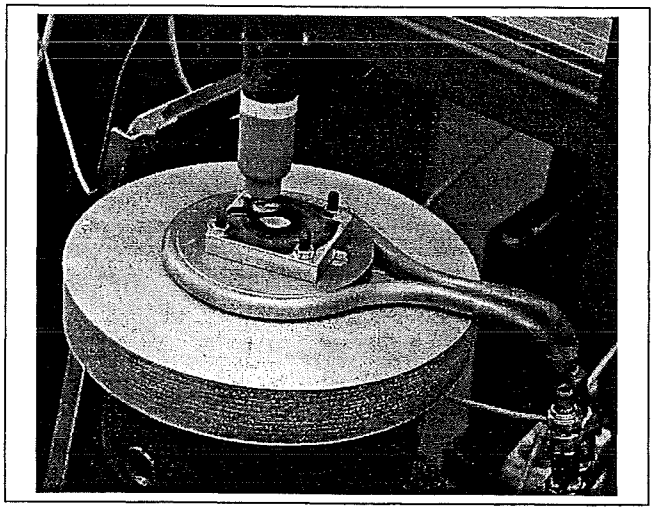

Fig. 3.2. CPT apparatus used in this study

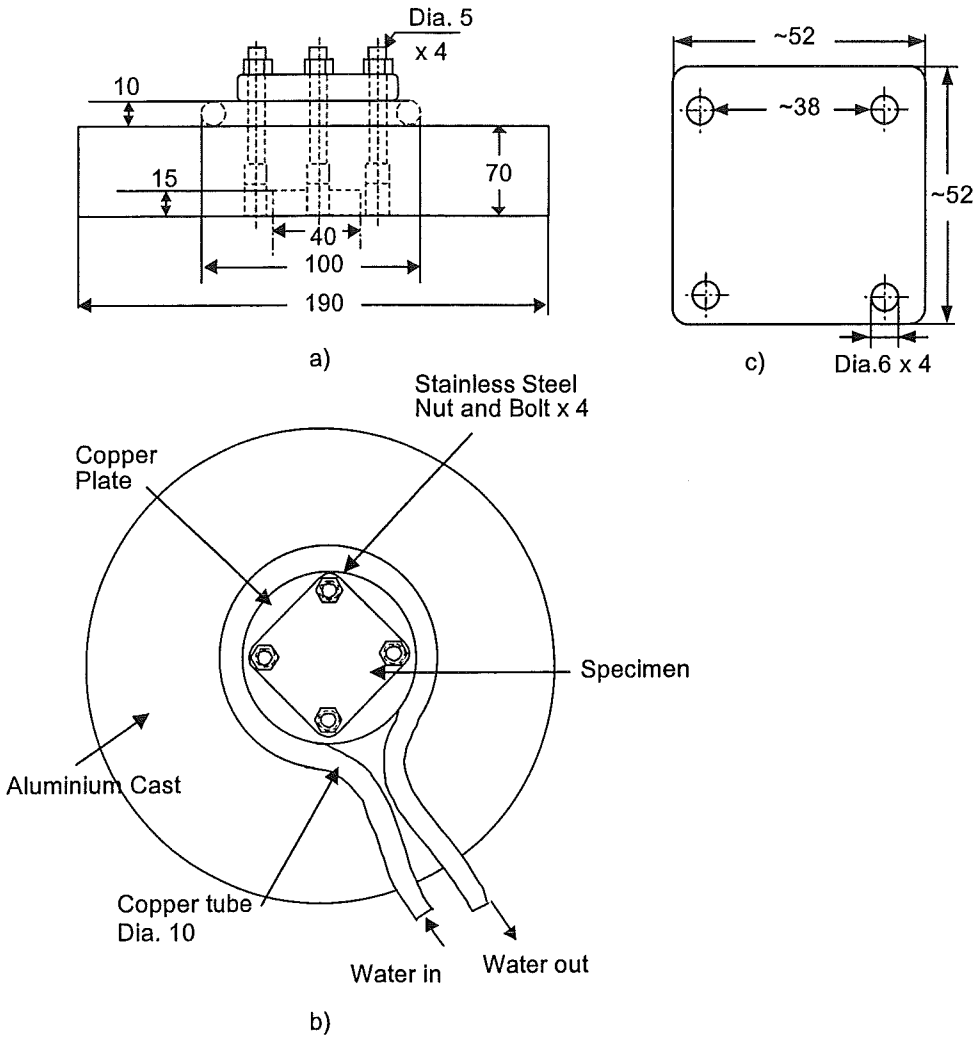

Fig. 3.3. Detail of the CPT equipment a) side view, b) top view and c) the CPT specimen. All dimensions are in mm.

During welding, the specimen was put on a water-cooled copper plate, which was placed on an aluminium plate. To hold the specimen on its place, a stainless steel bolt (5 mm in diameter) was used on each corner of the specimen. The bead on plate welds were then made by rotating the specimen under a fixed welding torch. For this purpose, DCEN TIG welding was utilised. The electrode used was a thoriated tungsten electrode of 2.4 mm in diameter with a 45° conical tip. The electrode sticks out about 5 mm from the ceramic cup, which has an internal diameter of 11 mm. The distance between the electrode tip and the specimen (the arc length) was maintained at 2.4 mm. Commercially pure helium shielding gas was used with an output

pressure of 1.2 bar. Other welding and stirring parameters are given in Table. 3.3 of Section 3.5. A Migatronic LDE 400 welding power source provided the current. The welding arc was ignited manually with the use of a carbon stick. Before the specimen is overcrossed, it was kept stationary for a couple of seconds to form a proper and stable weld pool. During the experiments, the welding current and the arc voltage were monitored with the help of a LabVIEW card.

3.3. Electromagnetic Coil

In this project, two types of coil have been made. In the preliminary stage of the project, a low-current coil without core was made of two copper wires (0.9 mm in diameter, each of 75 m long) wound simultaneously. The windings were intended to produce a magnetic field in opposite direction (polarity). This would be attained by using a pulsed direct current in such a way, so that when the current in one of the winding is maximum, in the other it is zero. By supplying a 16 A constant DC, a 14 mT magnetic field could be produced. Since this magnitude was too low for the experiment, a high-current coil (Fig. 3.4) was developed in the later stage of this project.

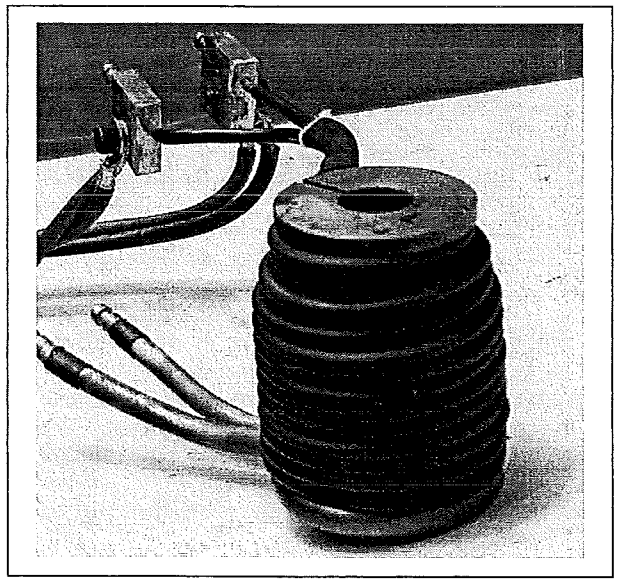

Fig. 3.4. Assembly of the electromagnetic coil used in this project.

The high-current coil was made of copper tube (5 mm diameter) with a soft magnetic material used as a core. The benefit of using a copper tube to construct the coil is that the heat generated by the high current can be removed by flowing cooling water through it.

Acting as the coil house was a copper pipe (25 mm inner diameter), both end being welded to a copper plate. A circular copper tube (8 mm dia.), welded to the bottom plate, was used as a cooling system for the construction, absorbing the heat radiated by the arc. A core (5 mm thick) surrounding the housing pipe was constructed of 7 layers of soft magnetic material sheets. The tube was covered by a crimp-isolator to prevent any contact between the different windings. An AC-DC welding power supply, Elma Technik, Hybrid 400 AD/DC, was used to supply the current to the coil. The capability of the power source to produce square wave alternating current (with a frequency of 1 to 1000 Hz) eliminated the need to use a frequency generator and an amplifier, as required for the low-current coil.

3.3.1. Magnetic Field Strength Calculation

To design the high-current electromagnetic coil, calculations to determine the magnitude of the magnetic field were first carried out. A suitable equation to calculate the magnetic field strength has been suggested by Boldyrev [35] as follows:

$$B = i\omega(0.266 - 0.011z); \tag{3.1}$$

where B is the magnetic field strength (Gauss), i the current (Ampere), ω the number of coil turns and z the distance from the base of the coil along the coil axis (mm) as shown in Fig. 3.5.

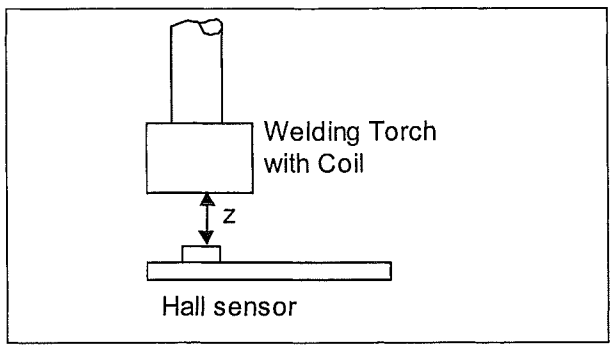

Fig. 3.5. Schematic diagram representing the z value used in equation 3.1 [35].

The problem with Boldyrev's equation is that B will change from positive to negative with increasing z, which is very unlikely to happen physically. Therefore, in this project, the magnetic field strength produced by the coil was determined by using an equation to calculate the magnetic field strength of a single wound coil without a core [after 36]:

$$B = \frac{\mu_o i}{2} \frac{a^2}{\left(a^2 + b^2\right)^{3/2}} \tag{3.2}$$

where B is the magnetic field strength (Tesla), $\mu_0 = 1.2566x10^{-6} Hm^{-1}$ for copper, i the electric current (Ampere), l the copper tube length per turn (m), a the coil radius (m), b the distance between the measurement point to the coil centre along the coil axis (m) and r the distance between the measurement point to the copper tube (m). For a multiple turns coil, each turn gives an additional magnetic field which magnitude is dependent on a and b. Hence, the changes in a and b of each turn need to be incorporated and equation 3.2 becomes:

$$B = \frac{\mu_o i}{2} \sum_{a_o}^{a_n} \sum_{b_o}^{b_n} \frac{a^2}{\left(a^2 + b^2\right)^{3/2}} \tag{3.3}$$

A schematic diagrams showing the definition the variables used in equation 3.2 is given in Fig. 3.6.a while a cross section of multiple turns copper tube coil and the definition of the variables used in equation 3.3 are given in Fig. 3.6.b.

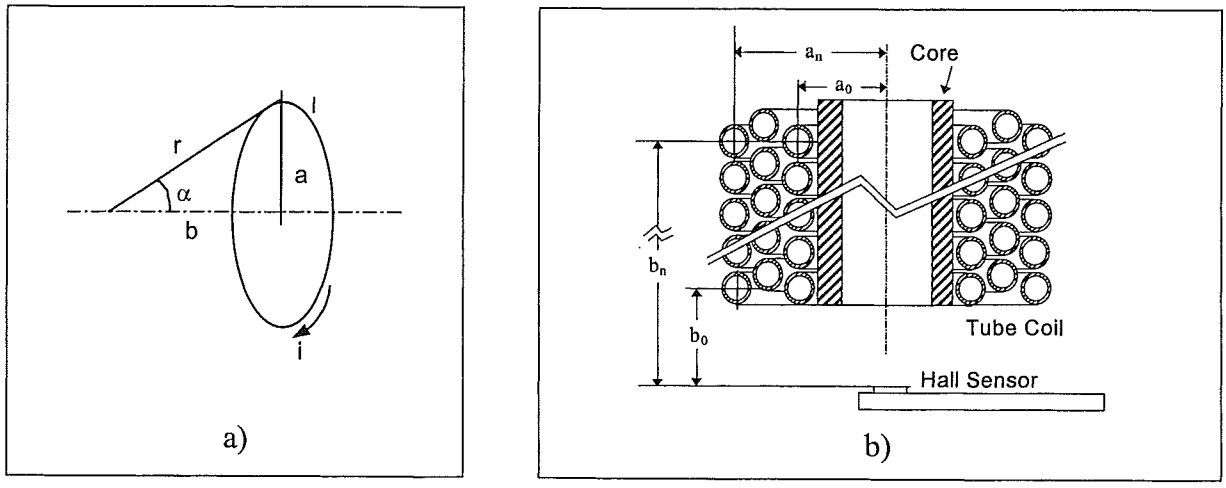

Fig. 3.6. Definition of variables used to calculate the magnetic field strength a) of a single wire coil (equation 3.2) [after 36] and b) in equation 3.3.

Before building the coil, preliminary measurements were carried out to verify whether there is agreement between the calculated magnetic field strength and the measured value. For this purpose a cylindrical coil of a single 9 turns copper tube (tube diameter 4 mm) was made. Taking b_o = 26 mm, and a = 16 mm, B was calculated by using equation 3.3. As a comparison the B at 26 mm underneath the coil at the coil axis was measured with a Lohet Hall-probe. In this measurement a DC electric current was fed to the coil. In addition, seven layers of soft magnetic sheet materials were used to simulate the influence of a soft magnetic core on the generated magnetic field strength. The results showed that the calculated B of a coil without core is slightly higher compared to the measured B (about 1.3 x). Furthermore, employing a core dramatically increases B. In this experiment the B of the cored-coil was found to be about 4 x higher than the calculated B of the coil without core. From these results, it appears that a suitable design can be made. In order to get a relatively high B, it is then necessary to utilize a soft magnetic core.

3.3.2. Coil Calibration

After building the core, the alternating magnetic field was calibrated with a Lohet Hall-probe. The measurement was carried out by placing the Hall-probe 2.4 mm under the electrode and 25 mm below the base of the coil (see Fig. 3.7).

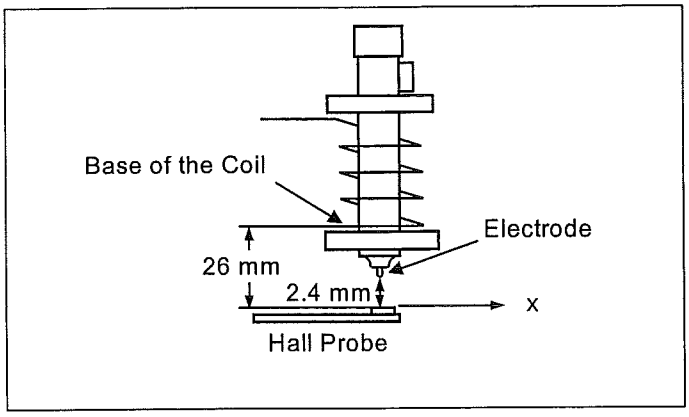

Fig. 3.7. Illustration of magnetic field strength calibration set up, x is the distance of the probe to the electrode axis.

Firstly, the magnetic field strength was determined as a function of the current and the frequency. For this measurement a square wave alternating current was provided to the coil. A Nicolet 410 data acquisition instrument was used to monitor both the current fed to the coil and the voltage generated by the Hall-probe. Fig. 3.8.a and Fig. 3.8.b show the signal of the coil current (100 Ampere) and the magnetic field produced at a frequency of 2 Hz and 30.3 Hz, respectively, measured at b_0=25mm.

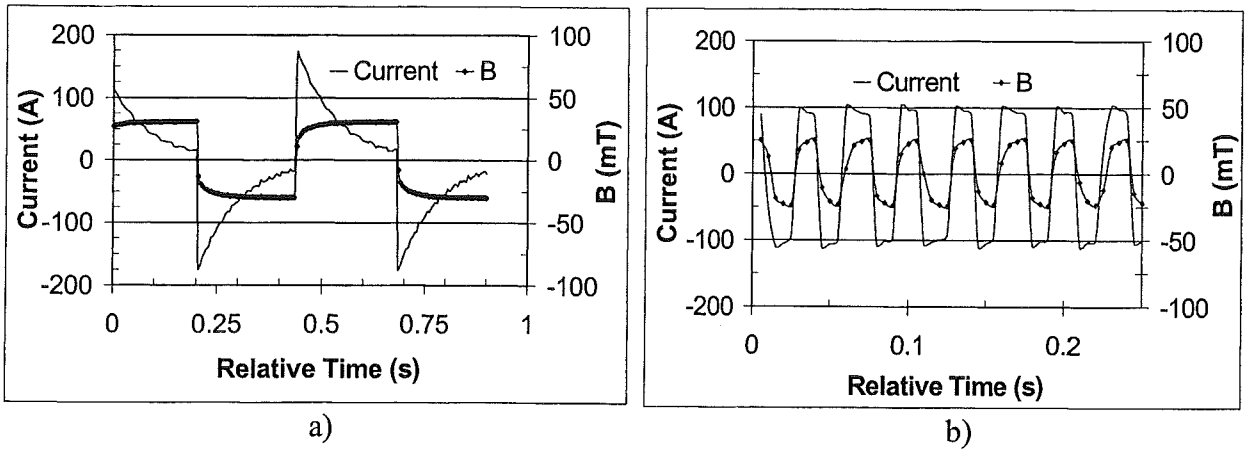

Fig. 3.8. Typical shape of alternating current (100 A) and the corresponding magnetic field signals for a) f = 2 Hz and b) f = 30.3 Hz.

Fig. 3.8 shows that the shape of the current signal as well as that of the magnetic field was not exactly square. However, for the sake of analysis simplicity, the magnetic field is considered to have a square waveform. The limit of the coil current (AC) used in this work was about 100 A. Beyond that value, the current became unstable.

The measured magnetic field strength was found to be about 2x of the calculated field strength of a coil without core. This is somewhat less than that was indicated above (about 4x). The use of different current mode (AC instead of DC as used before) might be responsible for this.

Fig. 3.9 and Fig. 3.10 present the magnitude of the magnetic field strength (B) as a function of the current and as a function of the frequency, respectively.

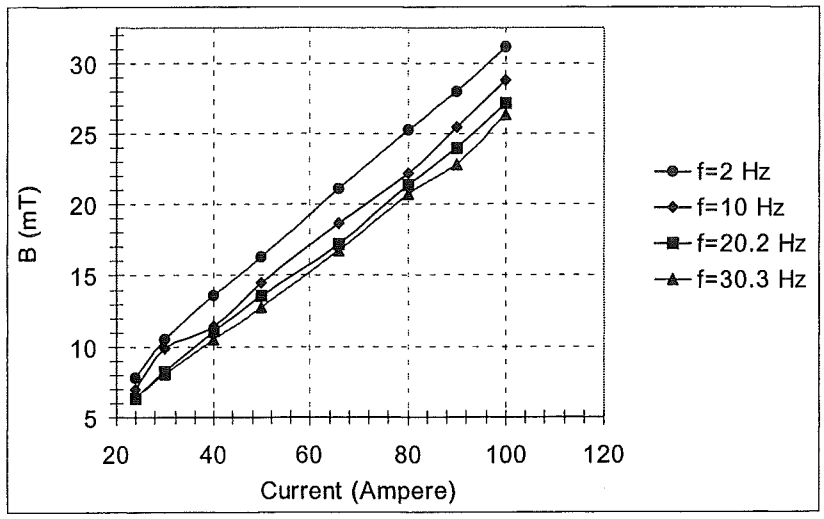

Fig. 3.9. Magnetic field strength (B) as a function of current (AC) for different frequencies.

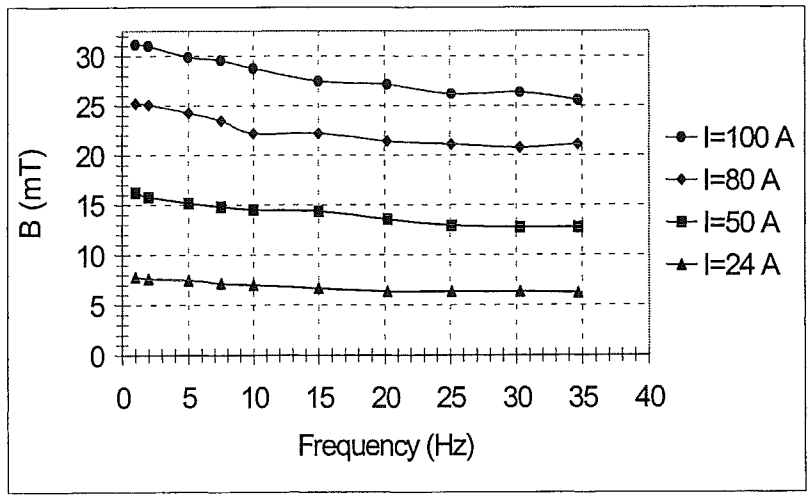

Fig. 3.10. Magnetic field strength (B) as a function of frequency for different coil currents (AC).

Shown in Fig. 3.9, up to 100 A, the coil does not reach a saturation level. In other words, it is still possible to obtain a higher magnetic field strength (B>31 mT) if a higher current could be supplied. Both figures show that at a certain current, B is decreasing with increasing frequency. Therefore, to investigate the influence of the frequency during the EMS experiments, with increasing frequency, the current needs to be increased in order to get a constant B.

Further calibration was aimed to observe the field homogeneity. For this purpose a constant direct current of 50 A was applied to the coil. The magnetic field was measured 25 mm below the coil base using a Hall-probe, in such a way that the probe was shifted in the horizontal (x) direction as shown in Fig. 3.7. The results, shown in Fig. 3.11, indicate that up to a distance of about 10 mm from the coil axis, the magnetic field is relatively homogenous.

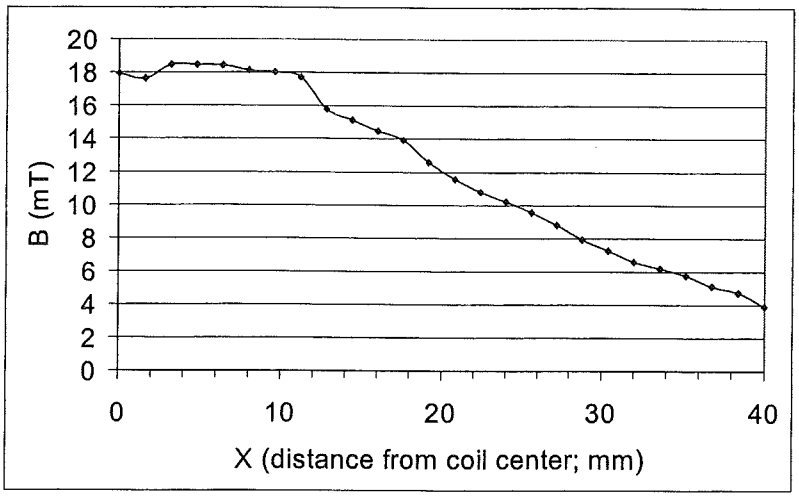

Fig. 3.11. Homogeneity of the magnetic field strength. X is the distance from the coil centre as shown in Fig. 3.7.

3.4. Straight Bead on Plate Weld

Beside CPT, bead on plate straight TIG welding was also carried out in this work. As in CPT, DCEN mode with He shielding gas was utilised. The welding and the stirring parameters are given in Table. 3.3 of Section 3.5. The basic part of the experimental set-up for bead on plate straight welding is shown schematically in Fig. 3.12. The specimens were fixed on a travel bench by a pneumatic clamp. During welding, the specimen was moved on the traverse underneath the welding torch. Both partial and full penetration autogenous TIG welds were produced with this set up. In the case of full penetration welding, a ceramic backing plate was used.

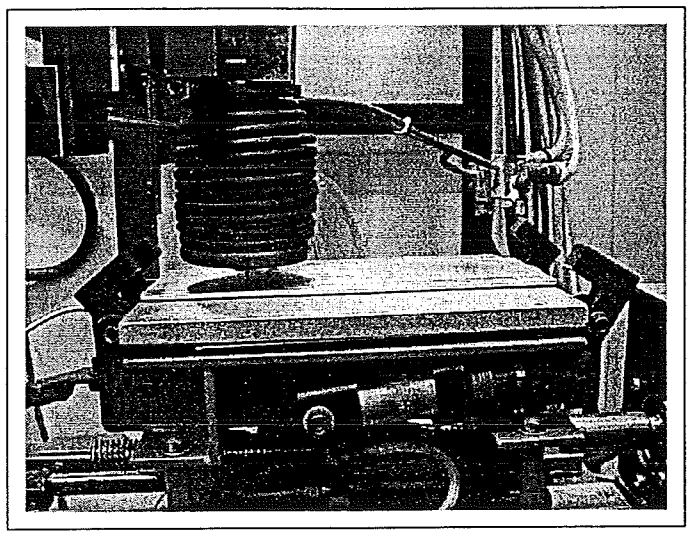

Fig. 3.12. Basic part of the experimental set-up for straight bead on plate welding with electro-magnetic coil attached to the welding torch.

3.5. Electromagnetic Stirring during welding

To use the equipment for the EMS experiments during welding, a LabVIEW program was developed. The program was aimed to activate the magnetic field automatically after a certain period of time and to monitor the welding current as well as the welding voltage. In most cases, the magnetic field was turned on about 10 seconds after igniting the arc. The current to generate the magnetic field was monitored separately by using the Nicolet. The parameters used in the stirring experiment are given in Table. 3.3.

Table. 3.3. Welding and electromagnetic stirring parameters used.

	CPT	Straight bead on thick plate	Straight bead on thin plate
Welding Current	120 A	125 A	80 A
Arc length	2.4 mm		
Travel Speed	2 mm/s	3 mm/s	4 mm/s
Shielding Gas/pressure	He, 1.2 bar		
Electrode	Thoriated Tungsten (W-2%ThO_2)		
Electrode Diameter	2.4 mm		
Magnetic Field Strength (nominal)	7, 11, 15, 20 and 25 mT		
Stirring Frequency (nominal)	2, 5, 7.5, 10, 15, 20 and 30 Hz		

The schematic diagram of the complete experimental set up with the CPT apparatus is shown in Fig. 3.13.

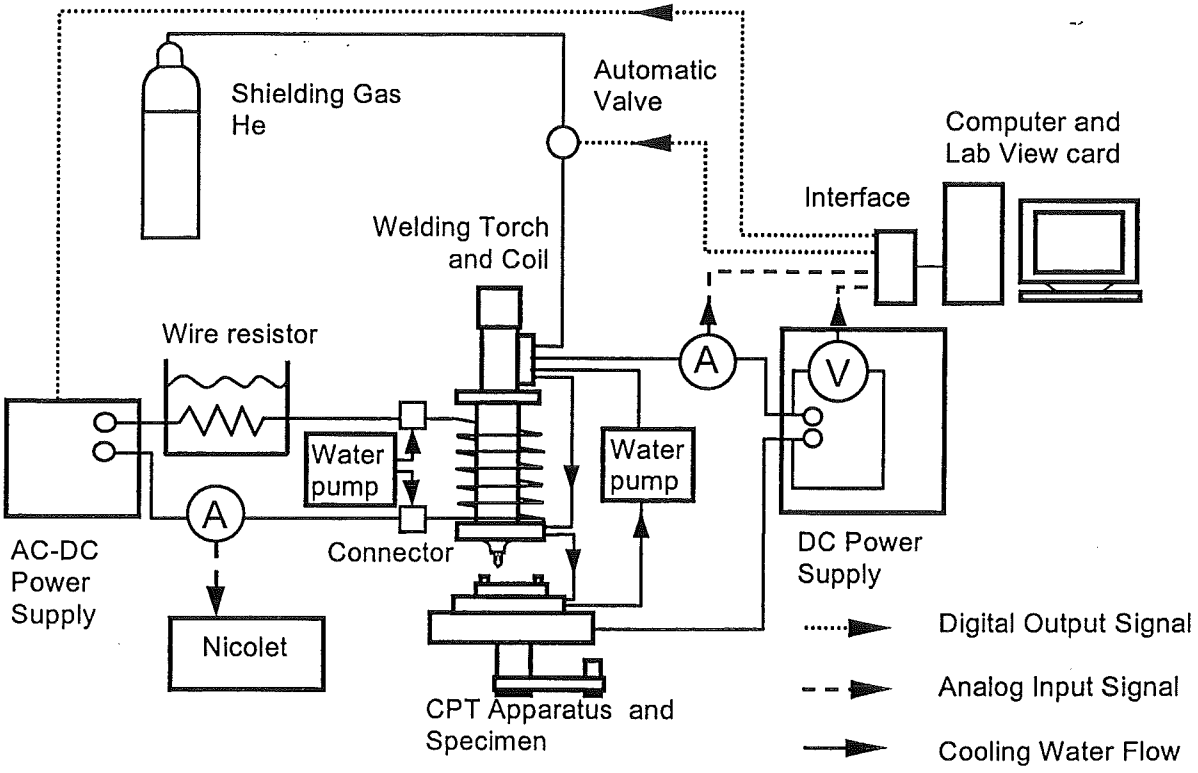

Fig. 3.13. Schematic diagram of the experimental set up with the CPT apparatus.

3.6. Microstructural Examination

The microstructure of the welded specimens was evaluated by using an Olympus BX60MF5 microscope equipped with a CCD camera Olympus DP10 and 'analySIS' imaging system software. To reveal the grain boundaries, polarised light was used. Before analysis under the microscope, the specimen (transverse cross section and top surface of the weld) were ground down to 600 grit and cotton-polished down to 1 μm, using a Struers manual specimen-preparation apparatus. Subsequently, the specimens were anodised with Barker solution (5 % HBF_4 in distilled water) using Struers Electropol operated at 20 V for about 180 second. After the samples were anodised, they were quickly washed with water to remove the anodising solution left and blown dry by pressurised air. In the case of cross sections of thin AA 6060

plate welds (specimen type 3), a cold curing resin (Technovit 4071) was used to facilitate the holding of the specimen.

To observe cracks in the weld, particularly the crack length, a Leica stereo microscope was used with a magnification of 40 x. In conjunction with this, the crack surface was examined using a Scanning Electron Microscope JEOL JSM6400F, with magnification up to 500 x. No special sample preparation was carried out for examining the crack length, whilst for SEM examination, the samples were cleaned by using acetone followed by iso-propanol. To reproduce a macrograph of the sample an Adimec MX12 digital camera equipped with a long focus length and Leica Qwin Pro V2.0 Imaging System was used.

3.7. Temperature Measurement

The influence of electromagnetic stirring on the distribution of the temperature on the weld pool was studied by measuring the temperature by means of thermocouple type K (chromel-alumel). The temperature measurement was carried out at certain locations in the weld pool, representing the fusion boundary and the centreline of the weld on AA 6082 sheets. For this purpose, thermocouples were attached to the backside of the specimen (see Fig. 3.14).

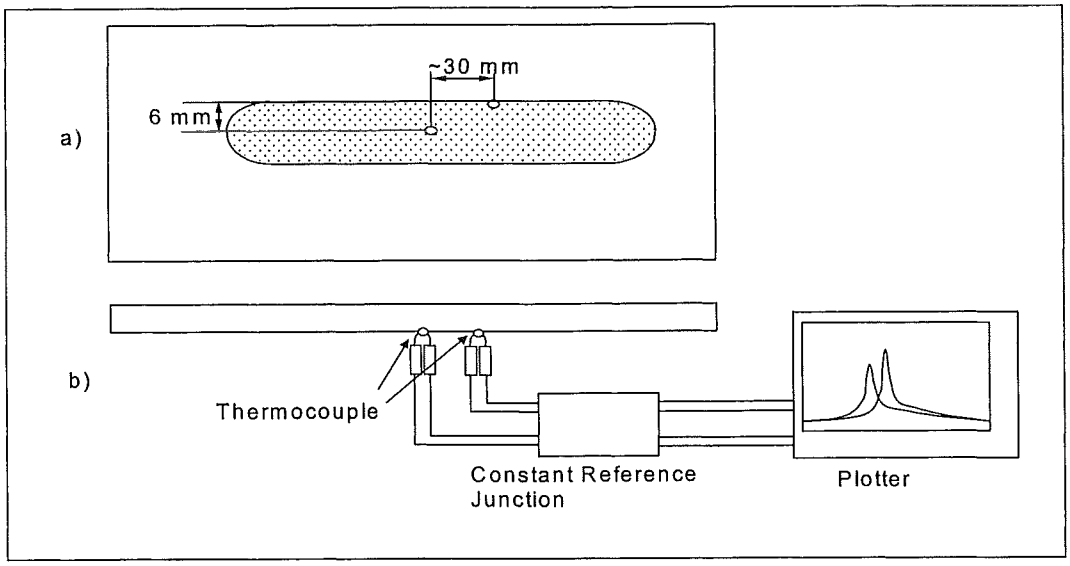

Fig. 3.14. Schematic illustration of a) thermocouple location and b) temperature measurement set-up.

The distance from the fusion boundary to the weld centreline was determined first by measuring the width of both an unstirred and a stirred weld bead without attaching any thermocouple. During measurement, the thermocouples were connected to a constant reference junction to compensate the room temperature and to a plotter to display the measurement results. A reference table, was used to convert the measured value (generated voltage) to a temperature. The welding and the stirring parameters are summarised in Table. 3.4.

Table. 3.4. Parameters used in the experiment to measure the temperature of the weld pool.

Welding Current	100 A
Arc length	2.4 mm
Travel Speed	4 mm/s
Shielding Gas/pressure	He, 12 bar
Electrode	Thoriated Tungsten
Electrode Diameter	2.4 mm
Magnetic Field Strength (nominal)	7 mT
Stirring Frequency	7.5 and 30 Hz

Chapter 4. Results and Discussion

4.1. Observations of Circular Welds

4.1.1. Unstirred AA 6060-T6 Circular Welds

Sets of unstirred-circular bead-on-plate welds were made on specimen type 1, to find welding parameters that give a continuous centreline hot crack by means of the Circular Patch Test, as defined in Chapter 3. The diameter of the bead circle was 30 mm at a rotational displacement equal to about 340°. The subsequent experiment was then aimed to find the optimum stirring parameters to refine the weld grain structure.

4.1.1.1. General observations

It was found that a welding current of 120 A and a travel speed of 2 mm/s gave the most continuous crack in this experiment. The width of the weld bead was found to be about 5.5 mm and the penetration depth was about 2.5 mm. The weld was characterised by the presence of a black layer substrate on either side of the weld boundary, which might be related with the aluminium oxide film on the specimen that produced by the arc. However, the detail mechanism of this phenomenon remains unclear and is not subject of investigation in this study.

4.1.1.2. Grain Structure

The macrostructure of the unstirred CPT weld showed epitaxial and competitive growth for the grains initiating from the fusion boundary towards the centreline of the weld. In addition, a band of fine or more correctly thin grains was found along the weld centreline. Fig. 4.1 shows (a) a transverse cross-section and (b) a top view of a CPT weld on AA 6060-T6.

It has been suggested that the formation of the fine equiaxed grains in the weld centreline is associated with a high constitutional undercooling concurrently with a proper nuclei supply (Chapter 2). This might be also the case in this study, though the grains were not exactly equiaxed. Besides, it might also be due to surface nucleation, since the fine grains were only present on the weld surface (Fig. 4.1.a).

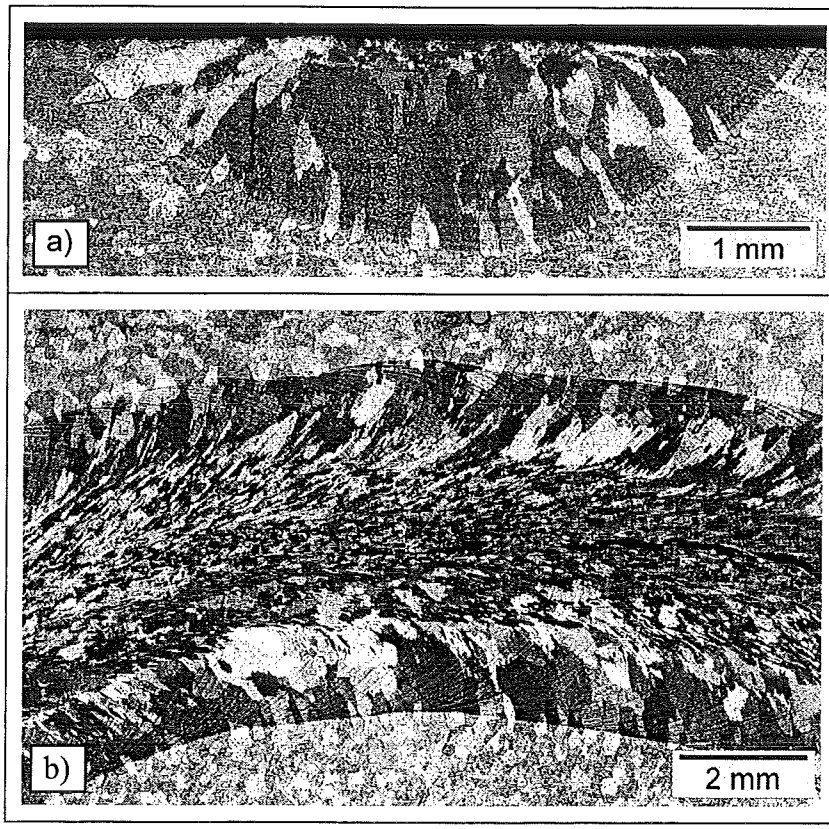

Fig. 4.1. Photomicrograph of AA6060-T6 unstirred CPT weld (welding current I = 120 A, travel speed v = 2mm/s), showing a) transverse cross-section and b) top view.

As shown in Fig. 4.1.b, circular striation lines appear along the weld. Observation under a higher magnification (200x) revealed that the striation line is related with dendrite cells which become thicker and thinner sequentially. Fig. 4.2 shows the microstructures (a) at the fusion boundary and (b) at the weld centreline. Note the change of the grain structure to cellular dendritic in the fusion boundary and a periodically change of dendrite cell that creates the striation lines shown in Fig. 4.1. According to David and Vitek [18], the change of the cell or dendrite spacing is due to sudden changes in the growth rate. The growth rate changes may result from thermal fluctuations that arise during welding, which can be due to fluctuations in currents, fluctuations in voltage, erratic welding or fluctuations in travel speed [6].

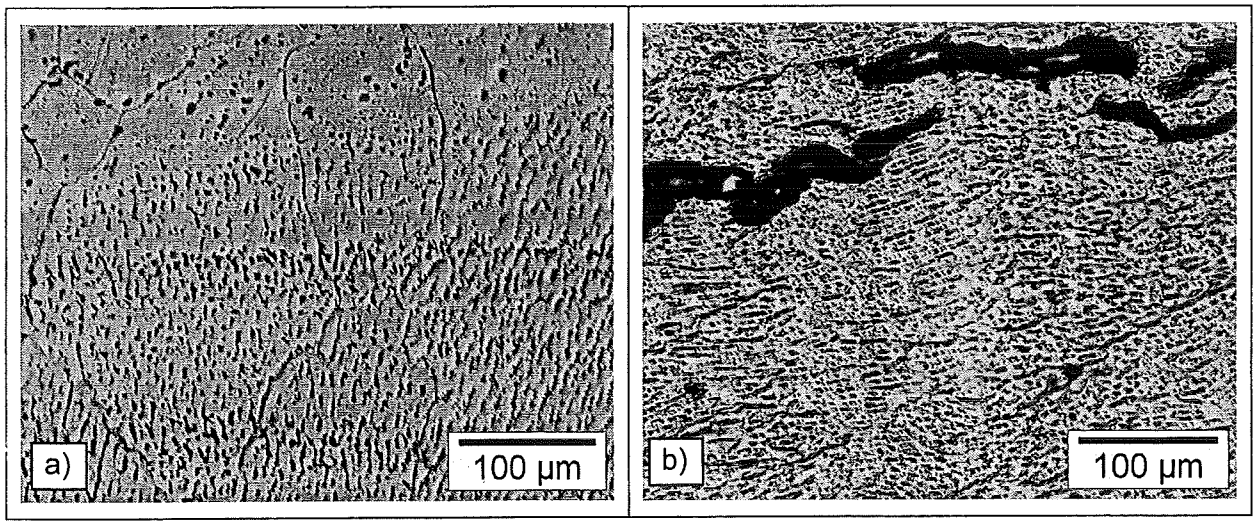

Fig. 4.2. Photomicrograph of the same weld shown in Fig. 4.1 at 200 x magnification of a) the fusion boundary and b) the centreline.

4.1.1.3. Hot Cracking

The welded specimen showed a relatively long and continuous crack, though sometimes short discontinuous cracks were also present. The cracks started mainly from the fusion boundary and grew towards the centreline. This is in agreement with the suggestion that the circumferential strains in CPT are larger than the radial strains at any instant (Chapter 3). It was observed that the cracks developed all along the weld. Furthermore, it was found that the cracks were not only developed as a surface crack but also as a sub surface crack and even developed at the weld root.

The crack is marked as an intergranular crack, a typical characteristic of hot cracking. Verified by SEM, the hot crack surface had a smooth surface representing the grain boundary with broken flakes-like substances spread on it [Fig. 4.3]. A spot semi-quantitative composition analysis using an Energy Dispersive Spectroscopy (EDS) indicated that the flakes-like substance contain more Si (6.05%) in comparison with the grain boundary (0.43%). This result supports the explanation that hot cracking takes place at the grain boundary on which a film of low melting-point eutectic or solute-rich liquid is formed but is not enough to backfill the incipient cracks. The grain surface follows a wavy pattern, which is most likely, related with

perturbation of dendrite growth on the grain boundary. This suggestion is confirmed by observing the microstructure adjacent to the crack on an unstirred CPT weld (see Fig. 4.4).

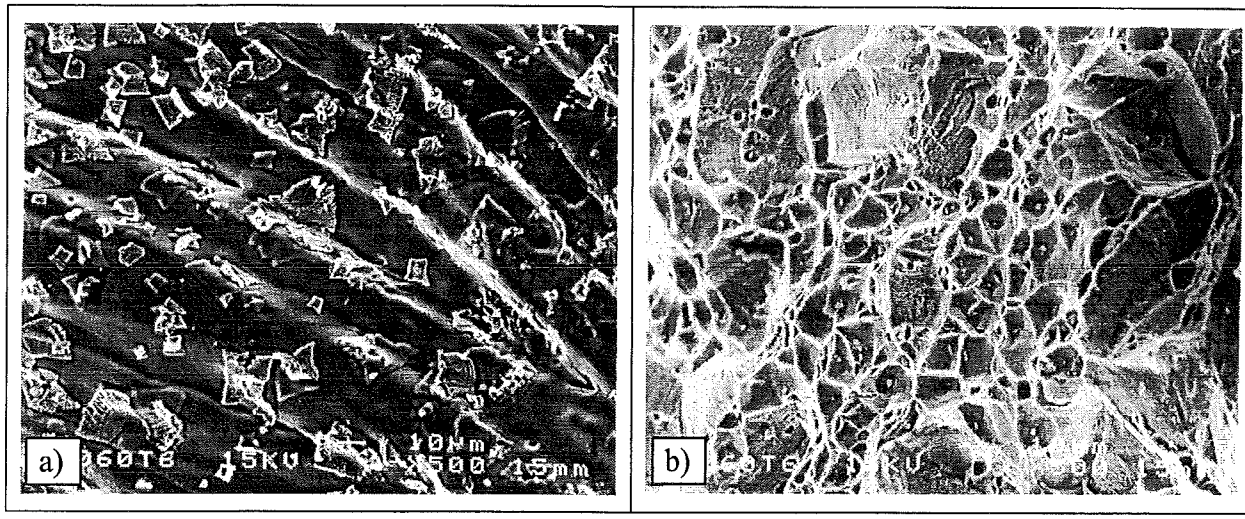

Fig. 4.3. SEM images at 500x magnification of a) hot cracking surface on CPT weld of AA 6060-T6 and b) base metal fracture surface of the same material due to overloading during sample preparation. Note the difference between the smooth surface on the hot crack and the rough-dimpled surface on the overload fracture.

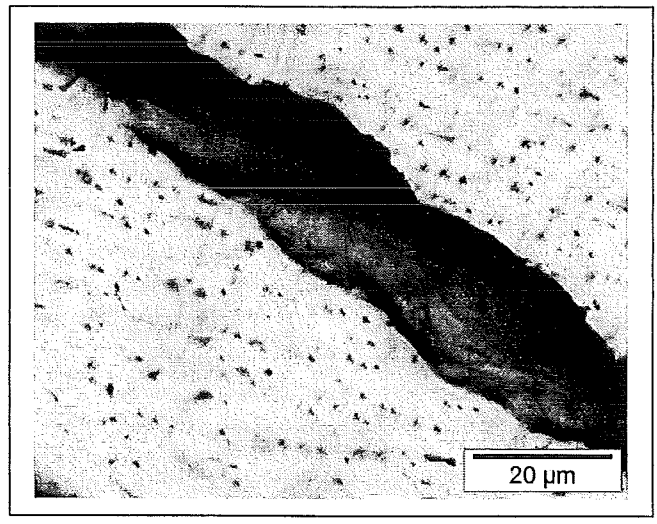

Fig. 4.4. Perturbation of dendrite growth on the grain boundary that leads to the formation of wavy grain boundary surface on an unstirred AA6060-T6 CPT specimen. The structure was observed on the weld surface (perpendicular to the crack surface) by using a light microscope at a high magnification (1000x).

4.1.2. Observations of Stirred AA 6060-T6 Circular Welds

By using the same welding parameters as defined above, EMS circular patch welds were made on specimen type 1. To investigate the optimum stirring parameter for grain refining, the magnetic field strength was varied from about 7 mT to about 25 mT, while the stirring frequency was varied from 2 Hz to 30 Hz. In most cases the magnetic field was turned on after the welding arc paved about 100^{o} of the circle.

4.1.2.1. Influence of EMS on the Grain Structure

The obtained results show that the grain structures of the stirred welds change significantly in comparison with that of the unstirred weld. In general, the microstructures developed during welding under various combination of stirring frequency and magnetic field strength can be grouped into two distinct types, columnar and equiaxed or refined. Examples of these typical grain structures are shown in Fig. 4.5. A more complete map of photomicrographs of the CPT stirred weld grain structure is given in Appendix 1.

It should be noted here that the grain structure around the centreline and on the surface of the stirred weld is somewhat coarser compared to that of the unstirred weld. However, transverse cross-section views of the stirred welds revealed that the grains below the surface, down to a certain distance, are finer compared to the unstirred weld. On the contrary, the grains below the surface in the case of the columnar structure type are relatively similar in scale to that in the unstirred weld.

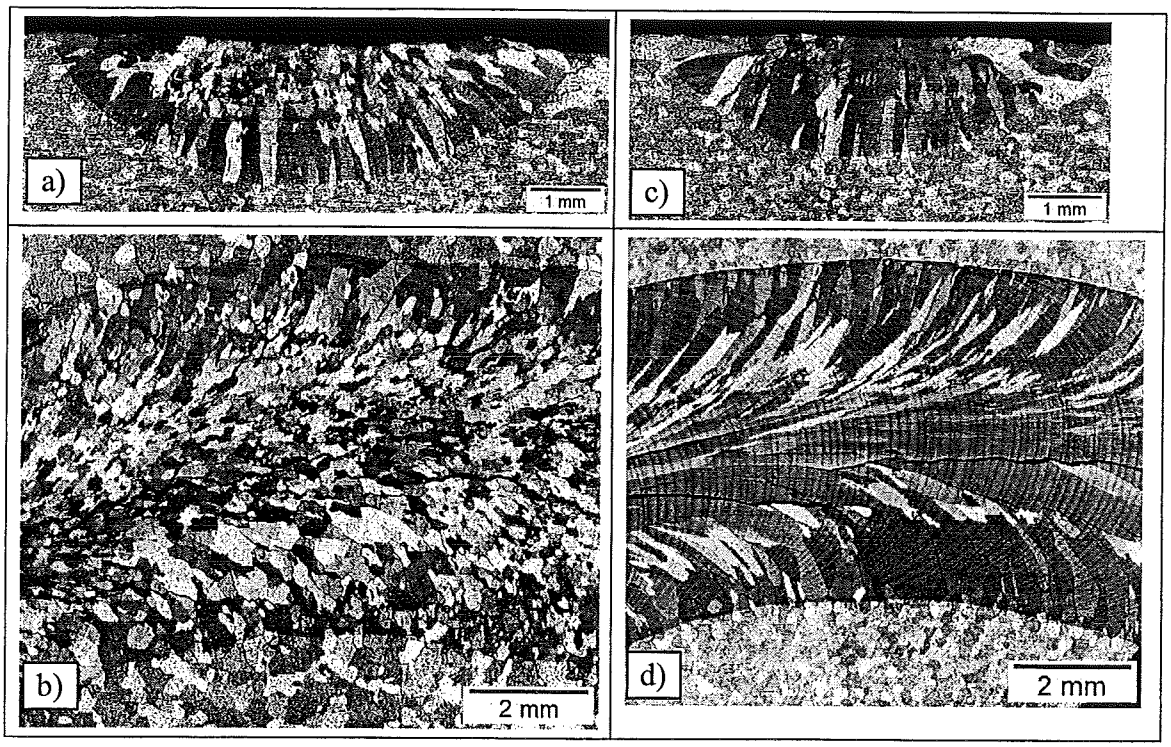

Fig. 4.5. Photomicrograph of the grain structure on a stirred AA 6060-T6 CPT weld f = 7.5 Hz, B = 14.8 mT a) transverse cross-section and b) top view; and f = 15 Hz, B = 14.5 mT, c) transverse cross-section and d) top view.

It appears that a low stirring frequency and/or high magnetic field strength produce the equiaxed or refined structure. Meanwhile, a high stirring frequency and/or low magnetic field strength yield a columnar structure. This relationship between the stirring parameters (stirring frequency f and magnetic field strength B) and the developed microstructures are depicted in Fig. 4.6. Different structures and different extent of grain refinement are presented by different greyscale of the marks. At f = 10 Hz, B = 11.4 mT and at f = 20 Hz, B = 8.3 mT and 13.6 mT, equiaxed structures occur but only on the weld surface. In addition, the structure of the weld stirred at f = 15 Hz and 20 Hz with B of about 25 mT were partially refined. These structures are considered as unrefined. Furthermore, it is seen in Fig. 4.6 that the grain refining effect is somewhat reduced when the magnetic field becomes too high at low stirring frequency.

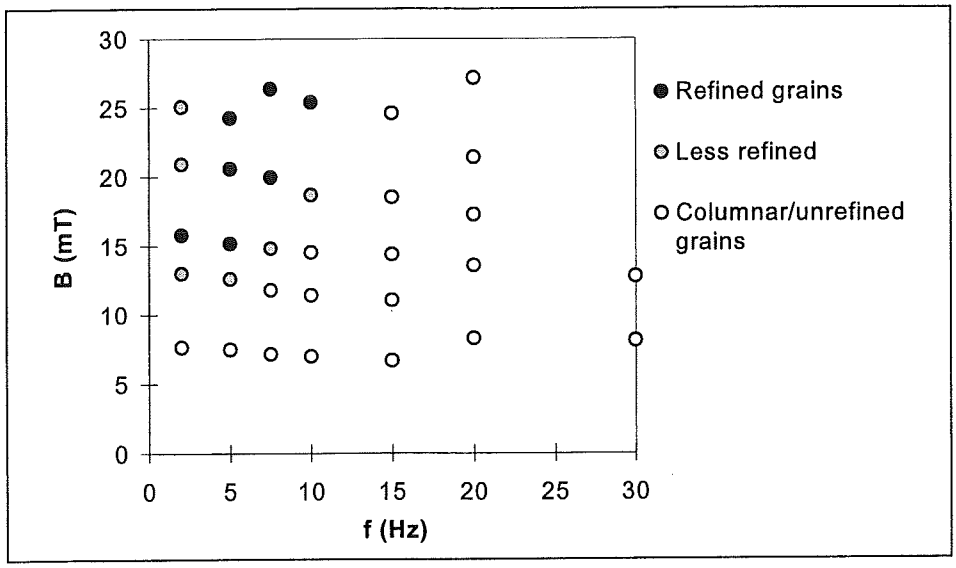

Fig. 4.6. The change in grain structure due to EMS during CPT of 10 mm thick AA 6060-T6.

As was explained, the formation of different microstructures in an unstirred weld is associated with constitutional undercooling. A higher constitutional undercooling (low G/R ratio) with proper nuclei supply leads to the formation of an equiaxed structure, while a lower constitutional undercooling (high G/R ratio) yields a columnar (dendritic) grain structure. Similar to the development of different microstructure in an unstirred weld, the G/R ratio of a low f and high B stirred weld should be lower compared to the G/R ratio of a high f low B stirred weld. It is believed that EMS reduces the temperature gradient in the weld pool [27]. On the basis of constant R, the G of a weld pool stirred with low f and/or high B is reduced more compared to the G of a weld pool stirred with high f and low B.

The stirred weld beads show apparent ripple lines along the weld. As an example Fig. 4.7 shows the ripple lines on a weld stirred with f = 2Hz and B = 15.8 mT (welding travel speed v = 2 mm/s and welding current I = 120 A). It has been reported [3, 4] that there is a relationship between the frequency and the striation line, in which the distance between each ripple line represents one half stirring cycle. In contrast with these results, the distance between striation lines in this experiment (CPT) represents one full stirring cycle. In Fig. 4.7, 1 mm of distance represents 1 full stirring cycle. Closer study of Fig. 4.7.b reveals that there are two regions between two ripple lines, shown as a darker region and a lighter region. Each region may then be associated with one half-stirring cycle.

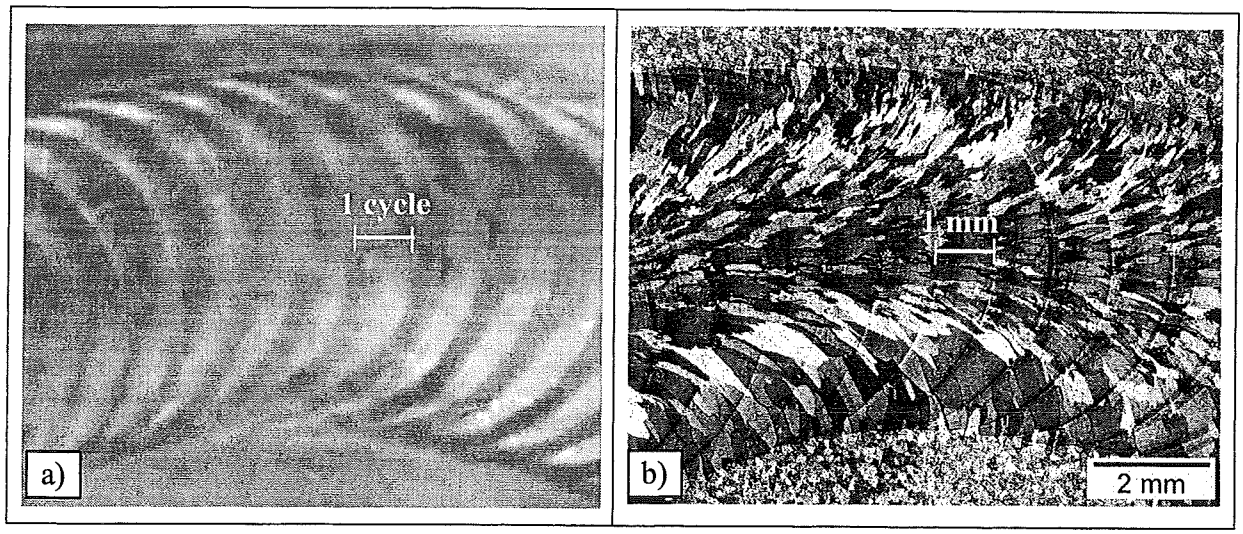

Fig. 4.7. Ripple lines on a stirred AA6060-T6 weld (f = 2 Hz and B = 15.8 mT) a) unpolished and b) polished and anodised.

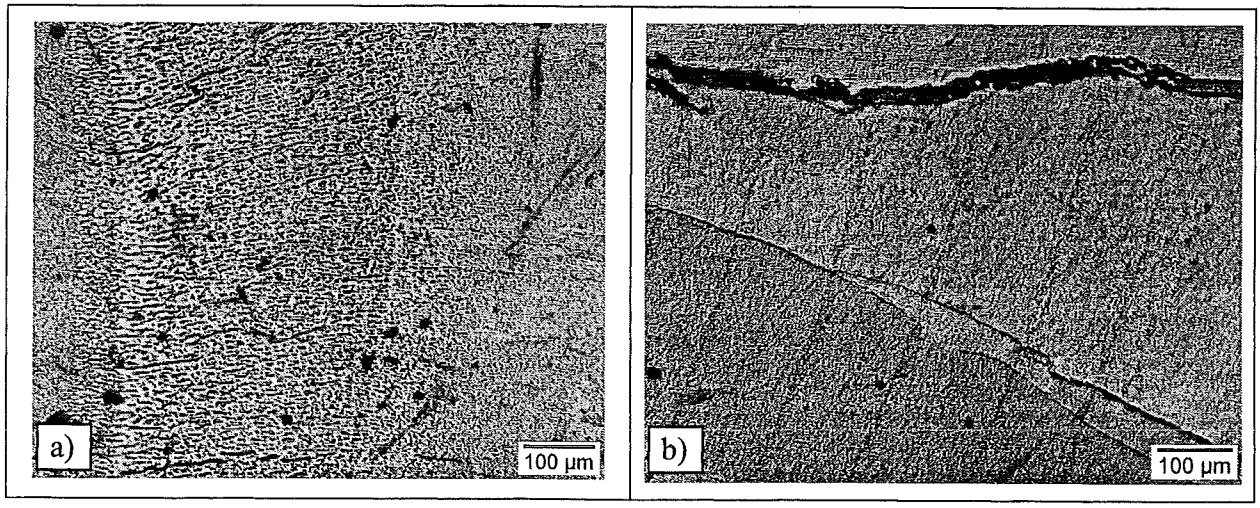

Fig. 4.8. Observed substructures in the weld centreline of AA 6060-T6 stirred at a relatively constant B = 15 mT with a) f = 2 Hz, and b) f = 15 Hz. The welds were made by means of CPT.

Microstructural observation under a higher magnification (100x) revealed that the dendrite cell thickness in the lighter region is finer compared to the dendrite cell thickness in the darker region. The ratio between the area of the coarser and that of the finer dendrite cell is increasing with decreasing stirring frequency and increasing magnetic field strength. This trend

is shown in Fig. 4.8, which shows photomicrographs of solidified weld metals stirred with stirring frequencies of 2 Hz and 15 Hz at a relatively constant magnetic field strength (B= 15 mT nominal). The occurrence of the different dendrite cell thickness between ripples has not been reported before. At this stage it is still a question whether this phenomenon was caused by the nature of CPT or by another cause.

4.1.2.2. Influence of EMS on the Hot Crack Nature during CPT

As far as hot cracking is concerned, it appears that EMS does not reduce or stop the CPT cracks. Though some degree of grain refining was found at certain conditions, all specimens experienced hot cracking all along the weld. This is most likely due to the relatively high restraint in CPT and the chemical properties of AA 6060, which is known to be highly susceptible to hot cracking. However, the crack nature in the stirred weld is different from the one in the unstirred weld. While the crack in the unstirred weld is relatively long and continuous at the weld centreline, the crack in the stirred weld becomes less continuous and spread to either side of the weld boundary. In many cases parallel cracks were found to grow simultaneously near the weld shoulders. The change of the crack nature could be related to the weld pool tail that shifts alternatingly to both sides of the weld boundary during EMS. However, the detail of the mechanism remains unclear and need to be studied further.

4.1.2.3. Other Remarks

It is observed that the welding voltage tends to increase when a magnetic field is applied. Fig. 4.9 depicts arc voltage and welding current during CPT welding under EMS (B = 25 mT nominal and f = 15 Hz). It is shown in Fig. 4.9 that the arc voltage increases about 10 second after the welding arc is ignited (at which the magnetic field was activated). The increase of arc voltage during stirring might be due to the change in arc length as a result of the broadening effect, as was reported by Malinowski et al. [24]. Besides that, it might also be associated with the behaviour of the arc that prefers the hottest part of the weld pool. During each half-stirring cycle one side of the weld pool is hotter than the other side [3]. Therefore, as the stirring proceeds, the arc will change side periodically. When the arc is bent and elongated aside towards the hotter liquid, its voltage increases. Different from the arc voltage that shows

an evident change due to electro-magnetic stirring, the welding current was found to be relatively constant during the experiment. This is very likely due to the use of the constant current power source.

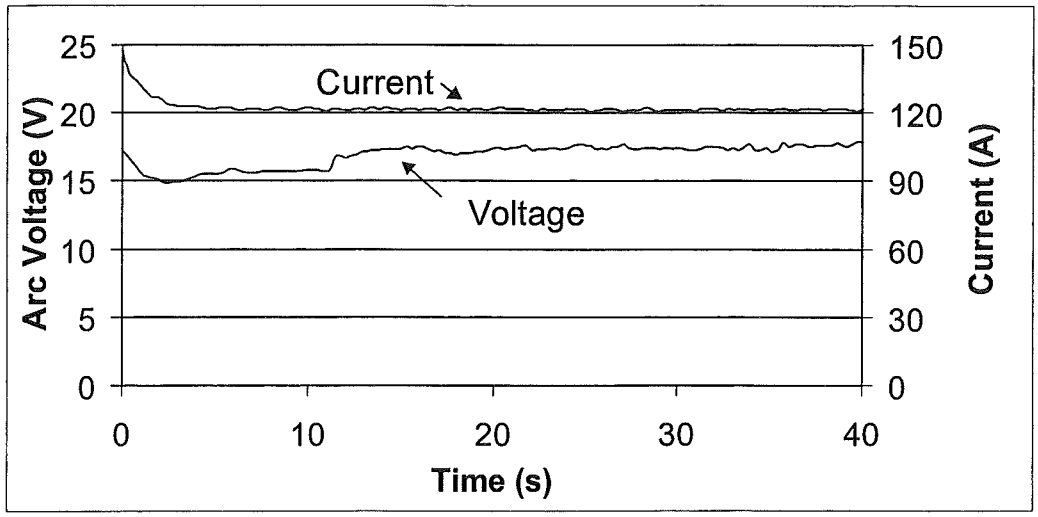

Fig. 4.9. Arc voltage and welding current during CPT welding under EMS (B = 25 mT and f = 15 Hz).

4.2. Observations of Straight Bead on Plate Welds

4.2.1. Bead on Plate Weld in AA 6060 Thick Plate (Specimen Type 2)

EMS during straight welding of AA 6060 thick plate (10 mm thick) was carried out using a welding current of 125 A and a travel speed of 3 mm/s. The experiment was aimed to investigate whether the formation of different regions of dendrite cell thickness as observed during weld pool stirring in CPT could also be found during straight welding. The magnetic field used was constant (B = 15 mT nominal) but the stirring frequency was varied (2 Hz to 15 Hz). Fig. 4.10 shows the microstructure of an unstirred and stirred (f_s = 2 Hz, B = 14.8 mT) straight TIG weld in an AA 6060 thick plate.

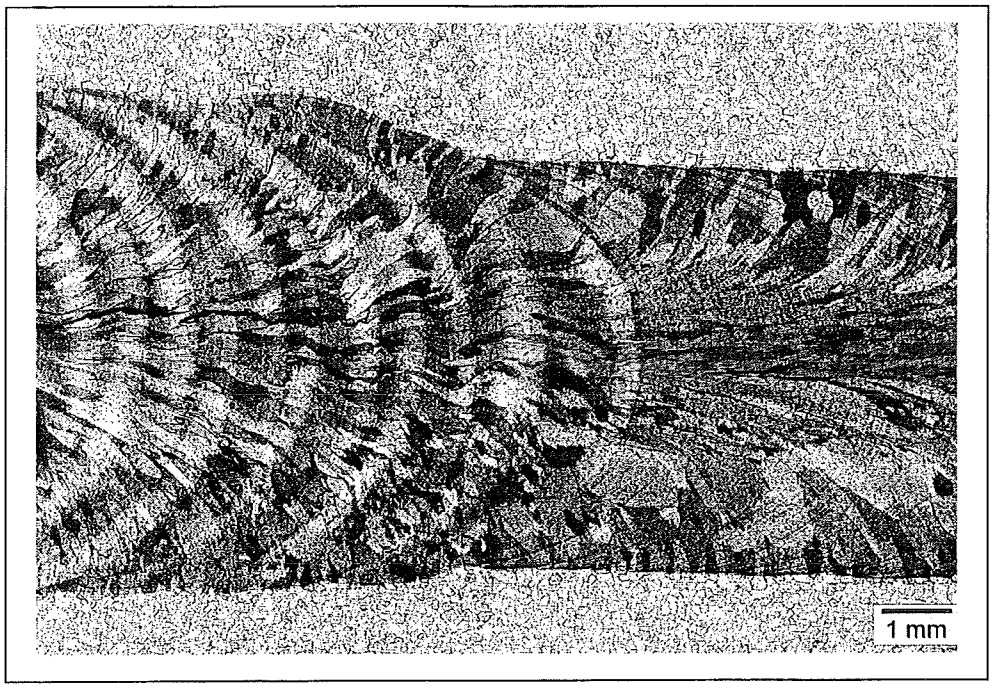

Fig. 4.10. Microstructure (top view) of a straight TIG weld in AA 6060-T6. The microstructure of the unstirred weld is shown on the right side, while the microstructure of the stirred weld (f = 2 Hz, B = 14.8 mT, v = 3 mm/s, I = 125 A) is shown on the left side.

As can be seen in Fig. 4.10, the distance between the ripple lines (about 0.75 mm) represent one stirring direction or one half stirring cycle. This is different from the phenomenon observed during CPT, in which the distance between the ripple lines represents one full stirring cycle. No clear explanation for this different behaviour is available.

Closer observation of the structure in Fig. 4.10 reveals that each half stirring cycle produces two regions of different dendrite cell thickness as was found in the experiment with CPT (see Fig. 4.11). As will be shown in the following section, this phenomenon does not occur during stirring of a full penetration weld. Based on this observation, it is likely that the formation of the finer and coarser dendrite region might be related with the size of the weld pool or the inhomogeneity of the arc. However, the details of the mechanism remain unclear.

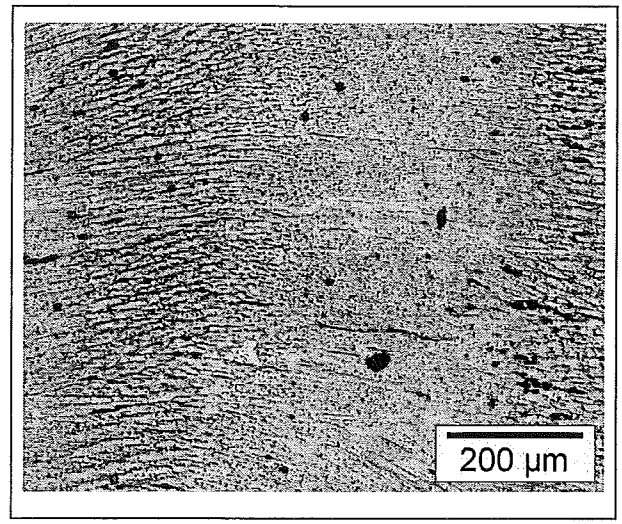

Fig. 4.11. Observed substructures around the centreline of an AA 6060 straight weld stirred at a stirring frequency f = 2 Hz with B= 14.8 mT.

4.2.2. Hot Cracking in AA 6060 Thick Plate Straight Welds

Similar to the results obtained with CPT, straight welding of AA 6060 thick plate also exhibits hot cracking. However, with the welding parameters used during straight welding, the cracks were less severe, i.e. less continuous and less opened than those in CPT. No solid evidence of reduction on hot cracking sensitivity due to EMS during straight welding of AA 6060 thick plate (partially penetrated) has been found.

4.2.3. Bead on Plate Weld in AA 6060 Thin Plate (Specimen Type 3)

The experiments with AA 6060-T6 thin plate were carried out in order to study the effect of EMS on the microstructure of fully penetrated welds. The welding current was 80 A and the travel speed was 4 mm/s. With these welding parameters, an axial grain structure as shown in Fig. 4.12 was developed. The structure seems to display columnar epitaxial grains growing from both weld boundaries and elongated grains growing around the weld centreline parallel with the weld travel direction.

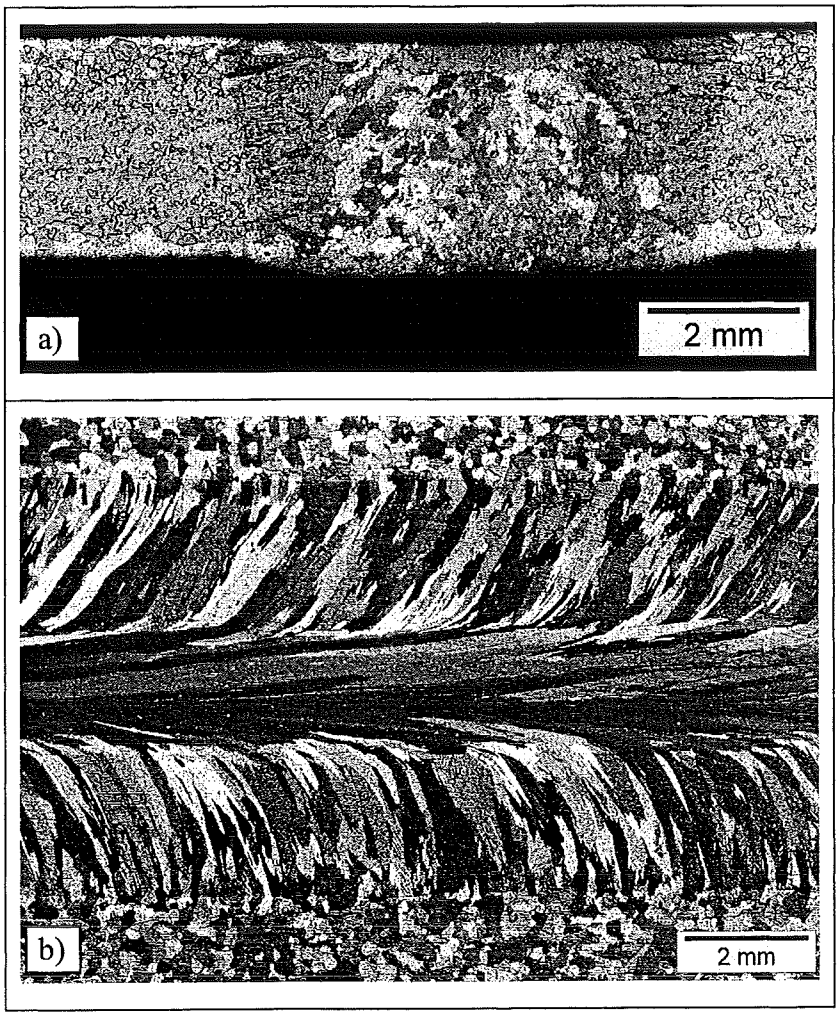

Fig. 4.12. Photomicrograph of fully penetrated straight bead on plate weld in AA 6060-T6 unstirred (I = 80 A, v = 4mm/s), showing a) transverse cross-section and b) top view.

Generally speaking, the experimental results of EMS on thin plate welds show an agreement with the results obtained in the case of CPT under EMS. This means that stirring with low f and high B leads to a reduction in grain size, while stirring with high f and low B produces coarse columnar grains. At a relatively high B, some specimens were experienced burn-through. Fig. 4.13 summarises the development of different weld microstructure due to EMS during straight TIG welding of AA 6060 thin plate (specimen type 3).

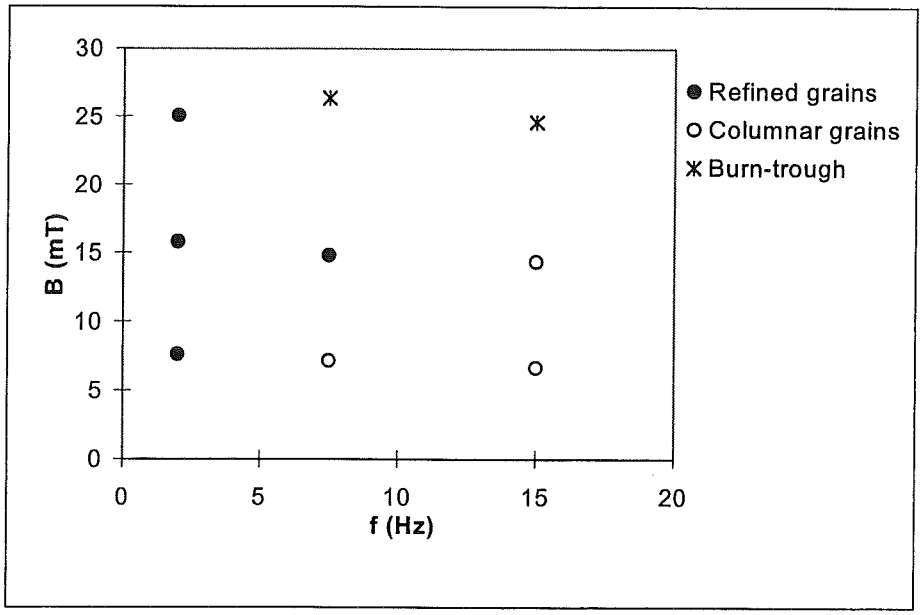

Fig. 4.13. Grain structures changes due to EMS during straight full penetration TIG welding of 3 mm thick AA 6060-T6.

It was observed that the shape of the refined grains due to EMS in a thin plate weld (full penetration) is different from that produced in the stirred thick plate weld (partial penetration). In the case of the full penetration weld, the reduction of the grain size takes place in such way that the columnar grains become thinner. In addition, new grains are developed when the magnetic field reverses its direction. This effect has been reported earlier by Matsuda et al. [20]. In agreement with their results, it was also found in this experiment that the new developed grains form a zigzag pattern in the weld, following the direction of the maximum temperature gradient. Examples of different microstructures developed due to different stirring parameters in AA 6060-T6 full penetration welds are shown in Fig. 4.14. A complete map of the different microstructures developed at different stirring frequency and magnetic field strength is given in Appendix 2.

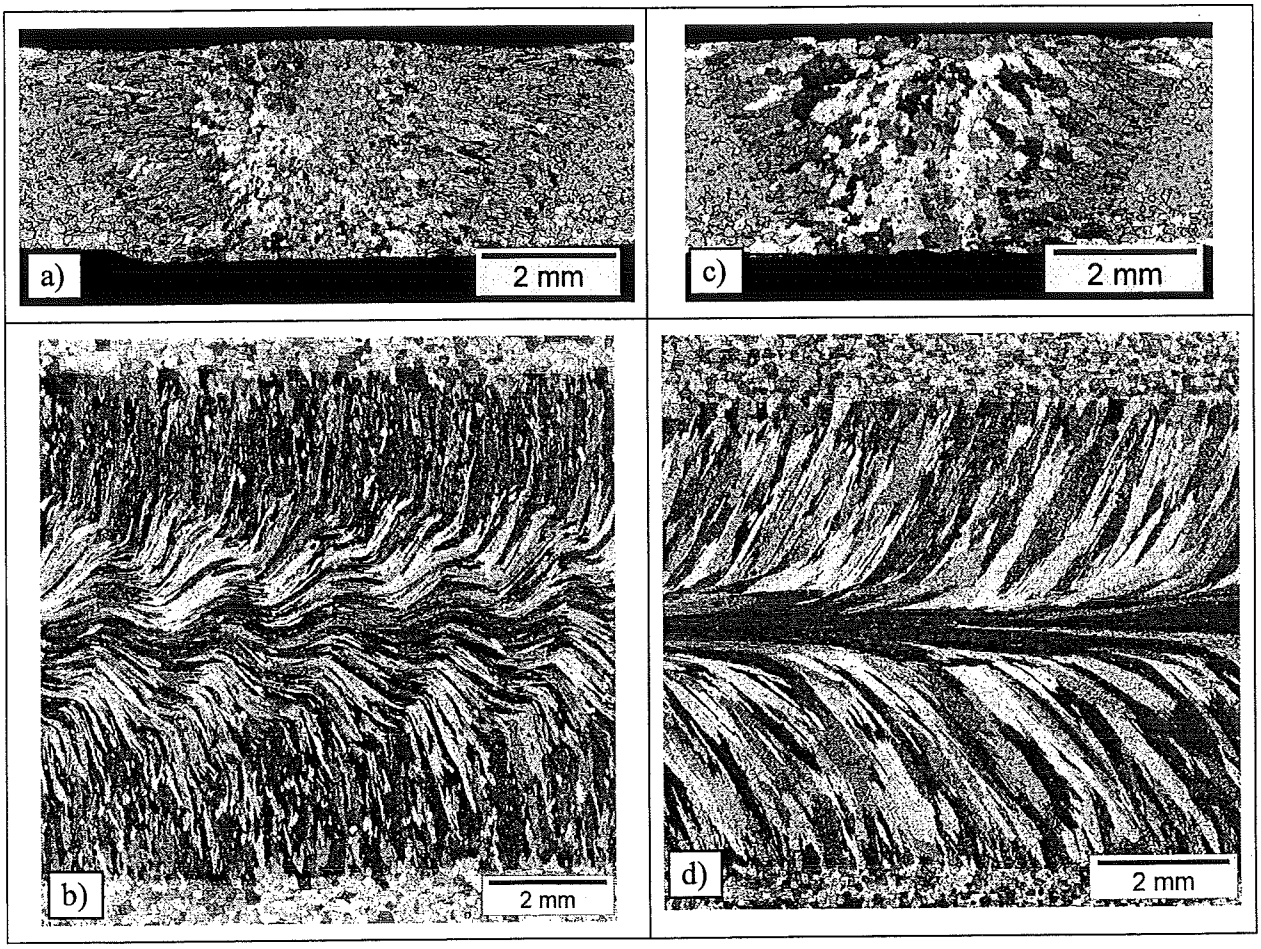

Fig. 4.14. Photomicrograph of stirred fully penetrated AA 6060-T6 weld. Fine structure (f = 2 Hz, B = 14.8 mT) is shown in a) transverse cross-section and b) top view and coarse structure (f = 15 Hz, B=7 mT) is shown in c) transverse cross-section and d) top view.

It can be seen from the cross-section views in Fig. 4.14.a and Fig. 4.5.a that the grain refining by EMS in the partial penetration weld only reaches to a certain depth below the weld surface, while in the full penetration weld, it can reach the bottom of the weld. This is obviously due to the shape of the weld pool. In the case of a partial penetration weld (thick plate welding), the shape of the weld pool is spherical. In this situation, the direction of the welding current (normal to the weld pool boundary) at the bottom of the weld is relatively parallel with the magnetic field vector ($\alpha \cong 0^{o}$). Thus, $\sin \alpha$ (in equation 2.9) $\cong 0$, and hence the Lorentz force is minimised.

In the case of a full penetration weld, the weld pool is cylindrical. The cylindrical weld pool makes the current at the bottom of the weld to flow almost perpendicular to the vertical magnetic field vector ($\alpha \cong 90^{o}$ or $\sin \alpha$ (in equation 2.9) $\cong 1$). Therefore, the Lorentz force extends to the bottom of the weld pool.

Observations of the microstructure of the weld under higher magnification (100x) shows that there are no changes in the dendrite cell thickness due to EMS in a full penetration weld (see Fig. 4.15).

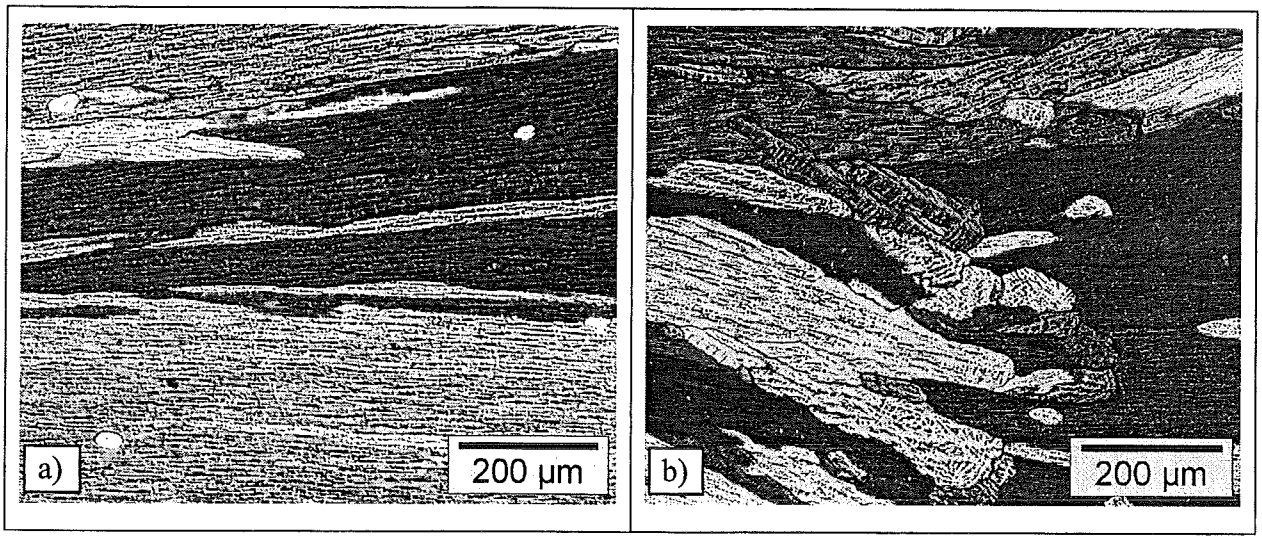

Fig. 4.15. Observed substructures around the centreline of a straight AA 6060 full penetration weld a) unstirred and b) stirred with f = 2 Hz with B = 14.8 mT. Note the formation of new grains when the magnetic field changes its polarity in b).

4.2.4. Hot Cracking in AA 6060-T6 Thin Plate Weld

Hot cracking was not found during straight welding of AA 6060 thin plate (I = 80 A, v = 4 mm/s). However when the welding parameters were changed to I = 100 A with the same travel speed, hot cracking was displayed. With this particular set of welding parameters, in comparison with the cracks on the unstirred thick plate welds (CPT and straight welding), the cracks in unstirred thin plate welds were less continuous and relatively short. An indication of the reduction of the sensitivity to hot cracking, due to EMS (f = 7.5 Hz, B = 14.8 mT) in thin

plate welds (I = 100 A) was found (see Fig. 4.16). However, since it is difficult to create a reproducible hot crack in the straight thin plate welds, further study is required at this point.

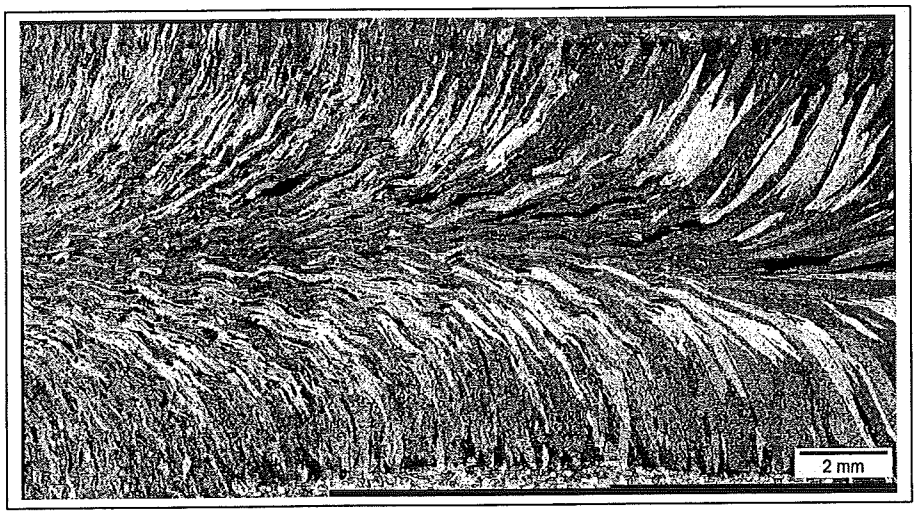

Fig. 4.16. Microstructure (top view) of a straight TIG weld in an AA 6060-T6 thin plate. The microstructure of the unstirred weld is shown on the right side, while the microstructure of the stirred weld (f = 2 Hz, B = 7.64 mT, travel speed 4 mm/s, I = 100 A) is shown on the left side. Note that cracking stops when the weld is stirred.

4.2.5. Bead on Plate Weld in AA 6061 Thick Plate (Specimen Type 4)

Welding of AA 6061 thick plates (15 mm thick) with EMS was carried out to study the effect of weld pool stirring on the microstructure of different alloy. The welding current was 125 A and the travel speed was 3 mm/s. The structure of an unstirred weld produced with these parameters, is shown in Fig. 4.17.a. The structure is very similar to the structure of the AA 6060 CPT unstirred weld specimen (Fig. 4.1), i.e. a band of fine grains has developed around the weld centreline.

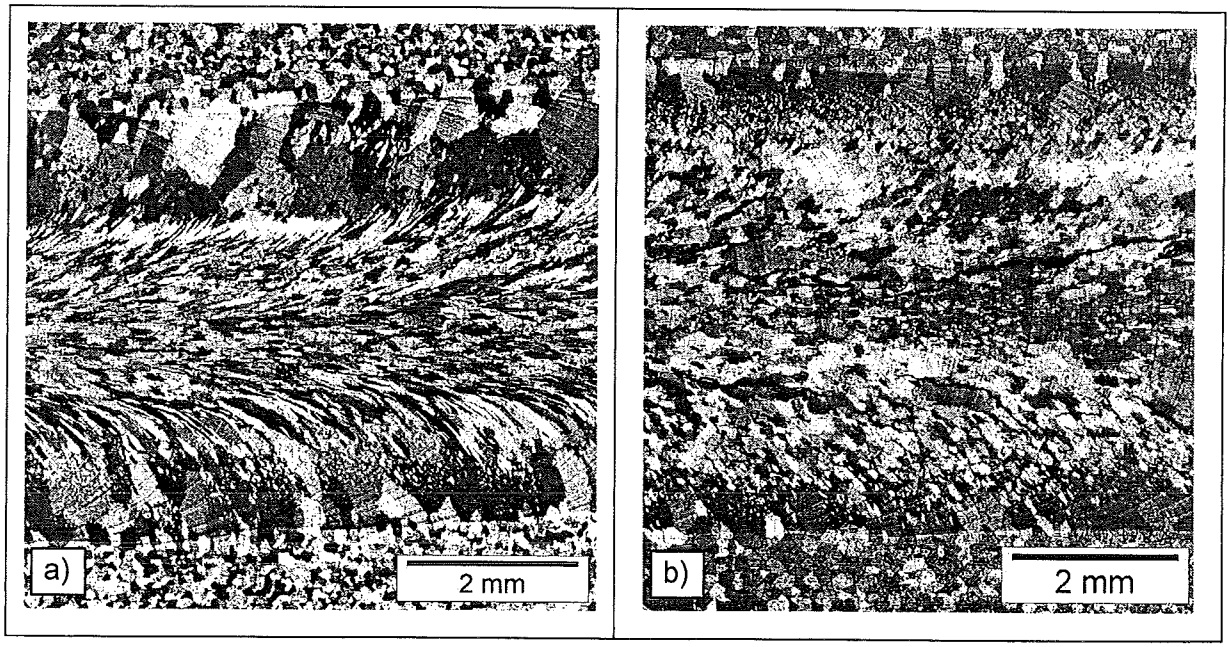

Fig. 4.17. Photomicrograph (top view) of grain structure of a) unstirred and b) stirred (f = 7.5 Hz, B = 26.4 mT) straight AA 6061 partially penetrated weld (I = 125 A, v = 3 mm/s).

Using the same welding parameters, EMS was applied at various magnetic field strengths (7 mT, 15 mT and 25 mT nominal) as well as stirring frequencies (2 Hz, 7.5 Hz and 15 Hz). Strictly speaking, the results of this experiment confirm the results of weld pool stirring with CPT and straight welding of 6060 given previously, that coarser grains are produced at high f-low B, while fine grains are produced at low f-high B. The refined grain structure of a stirred AA 6061 weld (stirring frequency f = 7.5 Hz with B= 26.4 mT) is shown in Fig. 4.17.b.

A complete map of microstructures developed in AA 6061 partial penetration welds under different conditions is given in Appendix 3.

4.3. Temperature Gradient

The measurement of the temperature of the weld pool was aimed to study the exact influence of EMS on the temperature gradient within the weld pool. Fig. 4.18 shows the thermocouple position at the backside of the 3 mm thick AA 6082 specimen (specimen type 5). The welding current used was 100 A and the travel speed was 4 mm/s. Unstirred and stirred (f = 2 and 30 Hz, B = 7 mT nominal) weld pool temperatures were measured.

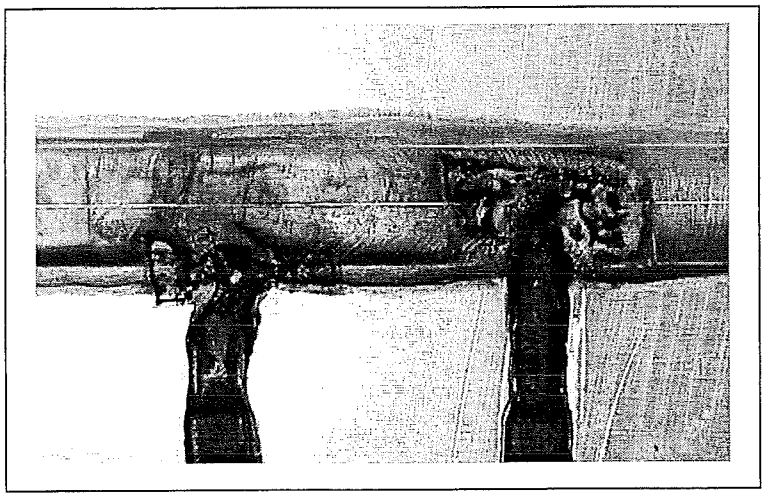

Fig. 4.18. Thermocouple position to measure the temperature of the weld pool at the backside of the AA 6082 specimen.

The thermocouple on the right side in Fig. 4.18 gives the temperature at the weld centreline (T_c). The other thermocouple was fixed at 6 mm from the weld centreline. In the case of an unstirred weld pool, the temperature given by this thermocouple (T_f) represents the temperature at the fusion line. However, in the case of a stirred weld pool, this thermocouple yields the temperature in the weld pool near the fusion line. This is because the width of the weld pool becomes somewhat larger when EMS is applied. The phenomenon of the increase of the weld pool width due to EMS is shown already in Fig. 4.10 and has been reported earlier by

other investigators (3, 24). A nominal temperature gradient (G_n) between the weld centreline and the point 6 mm from it towards the fusion boundary, can be obtained by simply dividing T_c-T_f by 6. Table. 4.1 shows the results of the temperature measurement and their corresponding nominal temperature gradient.

The results given in Table. 4.1 indicate that the temperature gradient of the weld pool stirred with a higher frequency is smaller than the temperature gradient of an unstirred weld pool but larger than the temperature gradient of the weld pool stirred with a higher frequency. It should be noted, however, that the data were obtained from single measurements and that more measurements are needed to achieve more exact results.

Table. 4.1. Nominal temperature gradient in the weld pool of AA 6060-T6 full penetration welds.

Sample	**T_c (°C) Centerline**	**T_f (°C) Fusion Line/ Near Fusion Line**	**ΔT**	**G_n (°C/mm)**
Unstirred	934	584	350	58.4
f = 2 Hz, B = 7 mT	836	602	234	39
f = 30 Hz, B = 8 mT	901	588	313	52.2

4.4. Fluid Flow

The mechanism of grain refinement during welding using EMS has been ascribed to the increase of constitutional undercooling (decreasing G/R), grain detachment, dendrite fragmentation or the change in the direction of the maximum temperature gradient (Chapter 2). It is very likely that increasing the velocity of the liquid metal flow in the stirred weld pool causes those mechanisms. Matsuda et al. [25] suggested that at a given magnetic field the fluid flow will decrease with increasing stirring frequency. Besides, an increase in magnetic field strength increases the Lorentz force and consequently the fluid flow in the weld pool.

The liquid flow in the weld pool during EMS can be further analysed by solving the Navier-Stokes equation given in Chapter 2 (equation 2.11). As was mentioned earlier, de Vries

[4] proposed a simplified solution of this equation in the case of unidirectional stirring in a steady state situation. His work led to an equation which describes the fluid velocity in the weld pool at any distance r from the weld pool centre as follows:

$$v_\phi = \frac{BI_w}{16\pi d\eta}\left(r - \frac{r^3}{R^2}\right) \qquad (4.1)$$

where η is the viscosity of the liquid metal and I_w the welding current, R the radius of the weld pool and d the plate thickness.

During stirring, the fluid velocity at the centre of the weld pool (r = 0) as well as at the weld boundary (r = R) is zero. If equation 4.1 is valid for a steady state situation ($t \cong \infty$), then the fluid flow at any value of r ($0 < r < R$) might be described as increasing from 0 at time t = 0 to a value given by equation 4.1 when time is reaching infinity. Hence, the fluid flow in the weld pool v_ϕ at a certain r ($0 < r < R$) under unidirectional stirring conditions might be depicted as a function of time t as in Fig. 4.19.

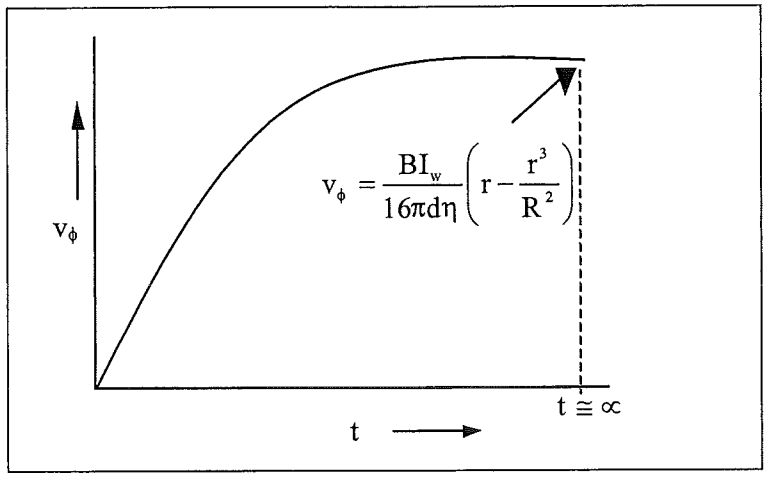

Fig. 4.19. Illustration of the estimated fluid flow v_ϕ in the weld pool during unidirectional stirring as a function of time t.

An approximation of the fluid flow in the case of alternating stirring can be obtained by solving the fluid flow problem in the transient state. An analytical approach and MapleV software were used to solve the problem. To obtain the solution of the fluid flow in the transient

state, the same assumption as used by de Vries [4] has been adapted here too, i.e. the weld pool has the shape of a cylinder with radius R and height d. Furthermore, the current distribution can be regarded to have a form as schematically depicted in Fig. 4.20 The current density is assumed to be constant over the top surface of the weld pool.

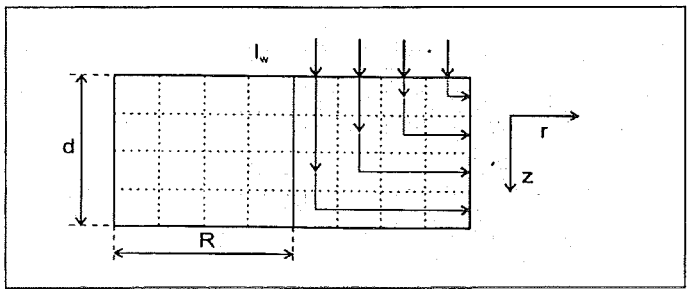

Fig. 4.20. Current distribution in a cylindrical weld pool in axial (z) and radial (r) direction [4].

Since in the case of unidirectional stirring the magnetic field is constant in magnitude and direction, the Lorentz force acting on a volume element of liquid metal can be written as [4]:

$$F_L = j_r x B = \frac{BI_w}{2\pi R^2 d} r \qquad (4.2)$$

Substituting equation 4.2 into equation 2.11 (the momentum equation in the azimuthal component of a cylindrical co-ordinate) results in the following expression:

$$\rho\left(\frac{\partial v_\phi}{\partial t} + \frac{v_r}{r}\frac{\partial r v_\phi}{\partial r} + v_z\frac{\partial v_\phi}{\partial z} + \frac{v_\phi}{r}\frac{\partial v_\phi}{\partial \phi}\right) = -\frac{1}{r}\frac{\partial p}{\partial \phi} + \frac{BI_w}{2\pi R^2 d} r + \eta \nabla^2 v_\phi \qquad (4.3)$$

Assuming that the azimuthal component of the fluid velocity as well as the arc pressure are homogeneous ($\partial v_\phi / \partial \phi = 0$ and $\partial p / \partial \phi = 0$) and neglecting the radial and the axial component of the fluid velocity (v_r and v_z are considered to be zero), equation 4.3 can be reduced to:

$$\rho\left(\frac{\partial v_\phi}{\partial t}\right) = \eta \frac{\partial}{\partial r}\frac{1}{r}\frac{\partial (r v_\phi)}{\partial r} + \frac{BI_w}{2\pi R^2 d} r \qquad (4.4)$$

To solve the above partial differential equation, it is assumed that the rotational fluid flow $v_\phi(r,t)$ in the weld pool due to EMS is a summation of the fluid flow in the steady state $s_\phi(r)$ and the fluid flow in the transient state $u_\phi(r,t)$ or:

$$v_\phi(r,t) = s_\phi(r) + u_\phi(r,t) \tag{4.5}$$

Substitution of equation 4.5 into equation 4.4 yields:

$$\rho\left(\frac{\partial(s_\phi(r)+u_\phi(r,t))}{\partial t}\right) = \eta\frac{\partial}{\partial r}\frac{1}{r}\frac{\partial(r(s_\phi(r)+u_\phi(r,t)))}{\partial r} + \frac{BI_w}{2\pi R^2 d}r \tag{4.6}$$

In the steady state ($t \cong \infty$), $u_\phi(r,t)$ becomes 0 and thus equation 4.6 can be simplified to:

$$0 = \eta\frac{\partial}{\partial r}\frac{1}{r}\frac{\partial(r(s_\phi(r))}{\partial r} + \frac{BI_w}{2\pi R^2 d}r \tag{4.7}$$

Using the boundary conditions $s_\phi(r) = 0$ at $r = 0$ and at $r = R$, equation 4.7 can be solved and yields:

$$s_\phi(r) = \frac{BI_w}{16\pi d\eta}\left(r - \frac{r^3}{R^2}\right) \tag{4.8}$$

which is in fact the solution derived by de Vries for the steady state fluid flow (equation 4.1). Substitution of equation 4.8 into equation 4.6, leads to:

$$\rho\left(\frac{\partial u_\phi(r,t))}{\partial t}\right) = \eta\frac{\partial}{\partial r}\frac{1}{r}\frac{\partial(r(u_\phi(r,t))}{\partial r} \tag{4.9}$$

To solve equation 4.9, the separation of variables method can be used [37]. In this method $u_\phi(r,t)$ is considered as a product of an unknown function X(r) which depends only on r and T(t) which depends only on t, so that:

$$u_\phi(r,t) = X(r)T(t) \tag{4.10}$$

After substitution of equation 4.10 into equation 4.9 and by using the boundary conditions $X(r) = 0$ at $r = 0$ and $r = R$ the partial differential equation can be solved which leads to:

$$T(t) = C_1 e^{-\lambda^2 t} \text{ and} \tag{4.11}$$

$$X(r) = C_2 J_1(\lambda R\sqrt{\rho/\eta}) \tag{4.12}$$

where C_1 and C_2 are unknown constants, λ is equal to $(3.83/R)(\eta/\rho)^{1/2}$ and $J_1(\lambda R\sqrt{\rho/\eta})$ is the Bessel function of the first kind of order one for $\lambda R\sqrt{\rho/\eta}$. With the initial condition $v_\phi(r,t)=0$ at $t=0$, C_1 and C_2 can be found which results in:

$$u_\phi(r,t) = \frac{BI_w}{16\pi d\eta}(-r + \frac{r^3}{R^2})e^{-\lambda^2 t} \tag{4.13}$$

and, hence,

$$\boxed{v_\phi(r,t) = \frac{BI_w}{16\pi d\eta}\left(r - \frac{r^3}{R^2}\right)\left(1 - e^{-\lambda^2 t}\right)} \tag{4.14}$$

Equation 4.16 expresses the fluid velocity in the weld pool in the case of unidirectional stirring during stationary welding. It gives the solution for both the transient state ($t < \infty$) and the steady state ($t \cong \infty$). As an example calculations of the fluid flow velocity in the weld pool of a thin plate (specimen type 3) were carried out, using equations 4.14, the materials properties given in reference 4, and the welding parameters used in this study (Table. 4.2 for thin plate). The results, presented in Fig. 4.21, show the fluid flow velocity as a function of r at different time t.

Table. 4.2. Values used to calculate the fluid flow in a stirred weld pool thin plate of aluminium alloys (fully penetrated weld).

Welding current	I = 80 A
Magnetic induction	B = 15 mT
Weld pool radius	R = 6 mm
Plate thickness	d = 3 mm
Viscosity [1)]	η = 1.5 mPa.s
Density [1)]	$\rho = 2.3 \times 10^3$ kg.m^{-3}

[1)] Data from reference 4.

From Fig. 4.21, it can be extracted that for $t > 0$ the maximum fluid velocity is obtained at a certain distance r* from the weld centre. The value of r* can be obtained by taking $dv_\phi (r,t)/dr = 0$, which yields

$$r^* = 0.58R \qquad (4.15)$$

or about 3.5 mm for the weld pool in the case of thin plate as used in this work. The fluid velocities at r* were calculated as a function of time and the results are presented in Fig. 4.22.

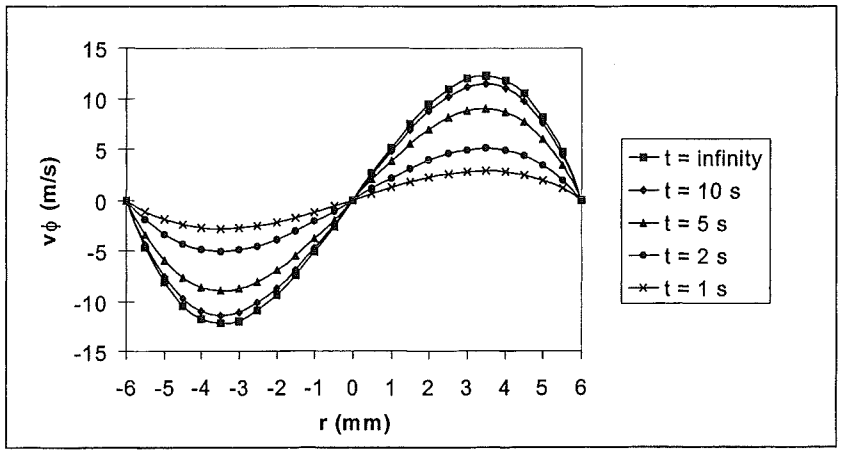

Fig. 4.21. Calculated fluid velocity v_ϕ in a static weld pool of a thin plate under EMS. The fluid velocity is presented as a function of the distance from the weld pool centre r at different elapsed time t during unidirectional stirring.

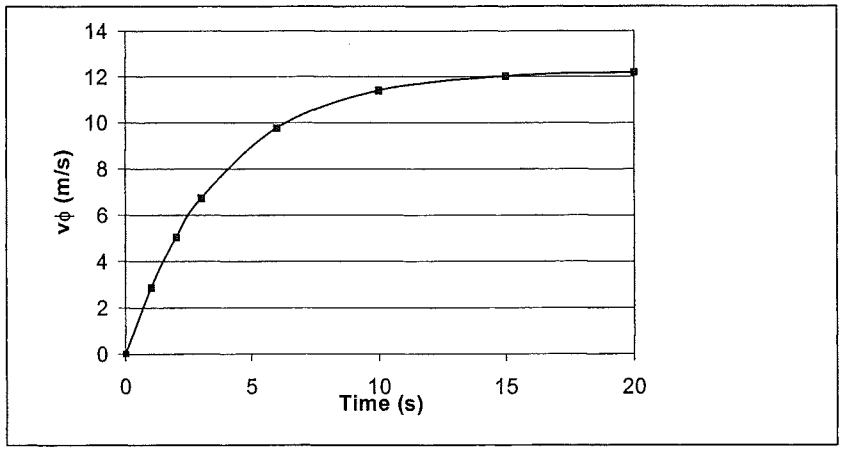

Fig. 4.22. Calculated fluid velocity at the distance r* = 3.5 mm from the weld pool centre in AA 6060 thin plate under EMS as a function of time.

From Fig. 4.22 it can be seen that the fluid velocity in the weld pool under unidirectional stirring conditions increases with time and reaches a maximum value of about 12 m/s.

In the case of alternating stirring, the relationship between a square waveform magnetic field and the fluid flow profile across a weld pool may be schematically illustrated as in Fig. 4.23:

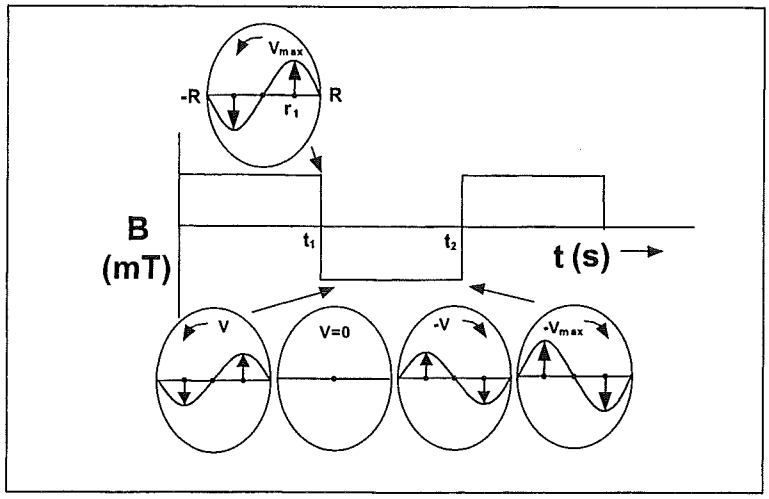

Fig. 4.23. Schematic illustration of the fluid velocity changes due to the changing of the magnetic field polarity or direction.

At time = t_1, when the magnetic field is just about going to alter its polarity, the velocity of the fluid is maximum in an anticlockwise direction. When the magnetic field direction is altered, the direction of the Lorentz force generated will follow. Consequently, the fluid flow will also change its direction, but not as abruptly as the Lorentz force does. The anticlockwise fluid flow first decreases until its velocity is zero, alters into a clockwise direction and reaches the maximum velocity at time = t_2. This process is repeated sequentially as the magnetic field alters its direction periodically. Assuming that the velocity of the fluid at a certain r as a function of time has a sinusoidal form, the velocity profile and its relationship with the magnetic field signal can be illustrated as in Fig. 4.24.

From Fig. 4.24, it can be deduced that during alternating stirring, the required time for the fluid to reach the maximum velocity from 0 is equal to a quarter of its one cycle stirring period T; $t = 0.25T$ or $t = (4f)^{-1}$. Using this assumption, the maximum fluid velocity during

alternating stirring can then be predicted using equation 4.14. Fig. 4.25 shows the comparison between the profile of the fluid flow in the weld pool due to unidirectional stirring and due to alternating stirring.

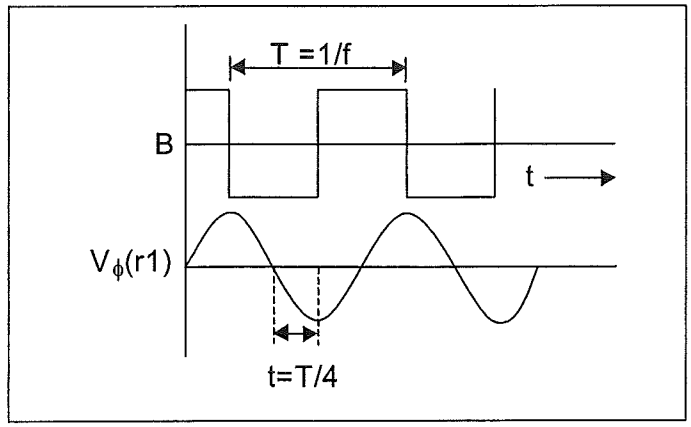

Fig. 4.24. Schematic illustration of the relationship between the magnetic field signal and the fluid flow in the weld pool under alternating stirring conditions. T is the period of one complete stirring cycle.

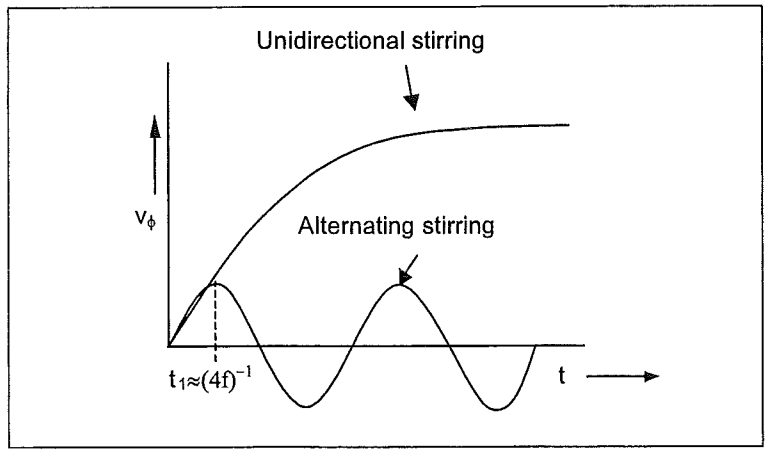

Fig. 4.25. The fluid velocity in an alternatingly stirred weld pool and the fluid velocity in a unidirectionally stirred weld pool.

Calculations of the maximum fluid velocities for alternating stirring, with different stirring variables, in a fully penetrated weld pool in a thin plate have been carried out. The thin plate is chosen since its weld pool has a nearly cylindrical shape on which the model is based. The material properties, the welding parameters and the weld pool size used in these

calculations were the same as those listed in Table. 4.2. The maximum fluid velocity was calculated at r* = 3.5 mm. The results are presented in Fig. 4.26 and Fig. 4.27.

Fig. 4.26 shows the fluid velocities in the weld pool of a thin plate as a function of stirring frequency for various values of the magnetic field strength. The results proves that at a given magnetic field strength and welding current, the velocity of the fluid in the weld pool decreases with increasing stirring frequency. For instance, at B = 15 mT, the maximum fluid velocity at stirring frequency 2 Hz, 7.5 Hz and 15 Hz are about 0.4 m/s, 0.1 m/s and 0.05 m/s, respectively. The higher fluid velocity obtained at low stirring frequency is due to the longer time available for the Lorentz force to accelerate the fluid.

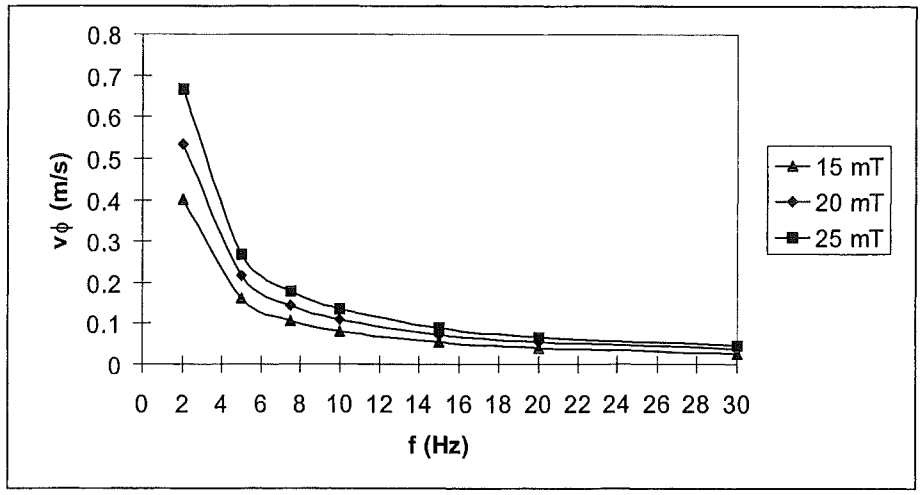

Fig. 4.26. Calculated fluid velocity at r* in the weld pool under electro-magnetic stirring conditions as a function of stirring frequency for different magnetic field strength. Data used for the calculation are given in Table. 4.2.

Fig. 4.27 shows the fluid velocities in the weld pool of thin plate as a function of magnetic field strength at different stirring frequency. The results presented in Fig. 4.27 show that for a certain stirring frequency, the fluid velocity v_ϕ increases linearly with magnetic field strength B. As can be seen in equation 4.14, this linear proportional relationship is also valid for the fluid velocity and the welding current. These facts are due to the higher Lorentz force produced with either higher magnetic field and/or welding current.

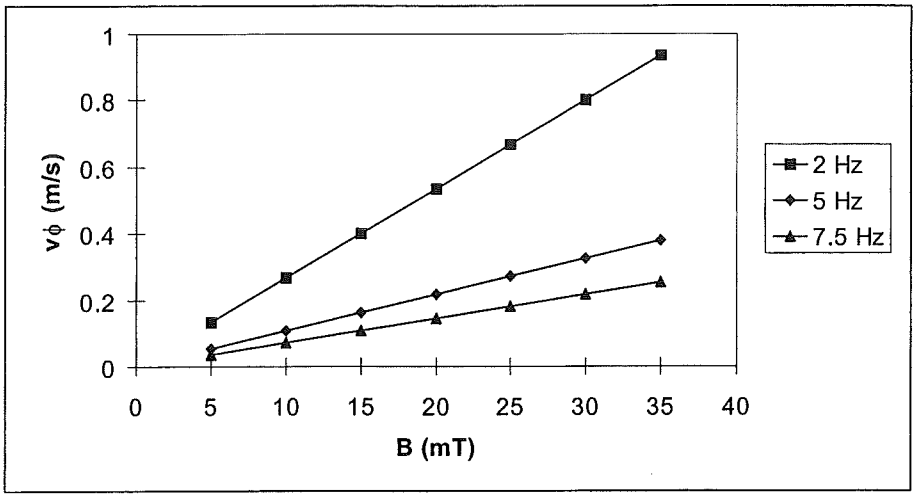

Fig. 4.27. Calculated fluid velocity at r* in the weld pool stirred with different magnetic field strength at frequency 2, 5 and 7.5 Hz. Data used for the calculation are given in Table. 4.2.

It is interesting to consider the influence of increasing welding current on the fluid velocity in the weld pool. As was just explained, the fluid velocity can be linearly increased with welding current. However, it is also known that the weld pool size is increasing with the heat input (for instance due to increasing welding current). According to equation 4.14, the weld pool size also influences the fluid velocity in the weld pool. As a result, when the changes in the weld pool width is also taken into account, the fluid velocity may not increase linearly with increasing welding current.

It is also interesting to see whether the fluid flow in the weld pool is laminar or turbulent. A rectangular open channel system has been considered as a model to characterise the fluid flow in the weld pool. In this approach, the weld pool is considered as consisting of two channels, each having an opposite flow direction to the other.

The Reynolds number (Re) for open channel flow is then defined by the equation 4.16 (after ref. 38):

$$Re = \frac{\rho v R_h}{\eta} \qquad (4.16)$$

Laminar flow occurs when Re < 500. The range from 500 to 2000 is the transition region and turbulent flow occurs when Re > 2000. R_h is defined as hydraulic radius which value is determined by [38]:

$$R_h = \frac{A}{WP} \tag{4.17}$$

where A is the cross sectional area, and WP is the wetted perimeter. The wetted perimeter is defined as the sum of the length of the boundaries of the section actually in contact with the fluid. Figurative expressions for the area A and the wetted perimeter WP are given in Fig. 4.28 [after ref. 38].

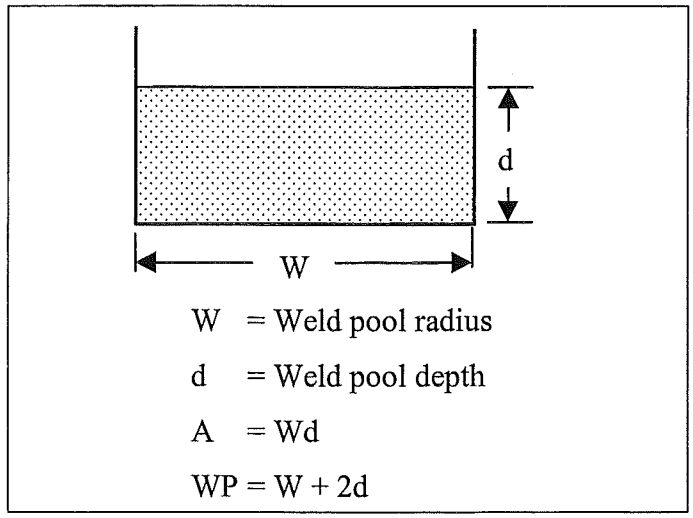

Fig. 4.28. Definition of area A and wetting perimeter WP used to characterise the fluid flow in the weld pool.

Taking η = 1.5 mPa.s, $\rho = 2.3 \times 10^3$ kg.m^{-3} and W = R = 6 mm (thin plate specimen case), the transition from laminar to turbulent flow (Re = 500) is reached when the fluid velocity is about 0.22 m/s. In a similar way, it can be shown that the turbulent flow (Re = 2000) occurs when the fluid velocity is about 0.87 m/s. Substituting these values into equation 4.14, yields combinations of magnetic field strength and stirring frequency that give the transition from laminar to turbulent flow as well fully turbulent flow conditions during welding of thin plate (I=80 A, d = 3 mm and R = 6 mm). These results are depicted in Fig. 4.29. The weld

microstructures that were produced by different combination of stirring parameters obtained in this study are also indicated.

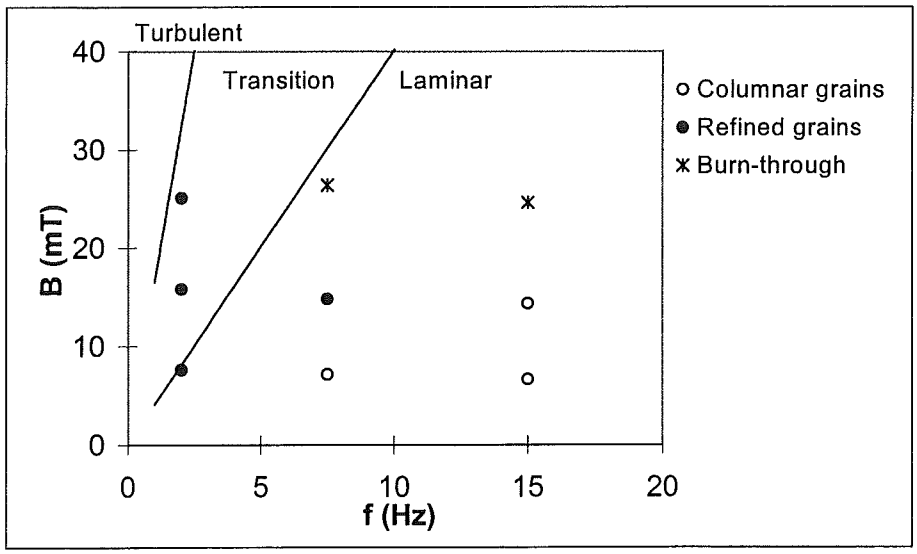

Fig. 4.29. The relationship between the magnetic field strength and the stirring frequency that gives the different modes of fluid flow. The corresponding microstructures of the stirred AA 6060 thin plate welds are also shown.

From Fig. 4.29, it can be seen that the formation of equiaxed or refined grains is starting to take place when the fluid flow becomes turbulent (transition from laminar to turbulent).

By neglecting the spherical shape of the weld pool in partial penetration CPT welds and using similar steps to characterise the fluid flow as in the foregoing discussion, a similar trend is shown in the case of thick plate specimens. The data used to characterise the fluid flow in the weld pool of CPT thick plate under EMS conditions are given in Table. 4.3, while the results are presented in Fig. 4.30. From Fig. 4.30, it can be seen that there is also an indication that grain refining due to EMS takes place at certain stirring frequency and magnetic field strength which correspond to the transition from laminar to turbulent flow. Since different assumptions have been made in the development of this model, further study to observe the exact fluid flow pattern in the weld pool is necessary to verify this suggestion.

Table. 4.3. Data used to characterise the fluid flow in the weld pool of CPT thick plate under EMS conditions.

Welding current	I = 120 A
Weld pool radius	R = 3 mm
Weld pool depth	d = 3 mm
Viscosity	η = 1.5 mPa.s
Density	$\rho = 2.3 \times 10^3$ kg.m^{-3}

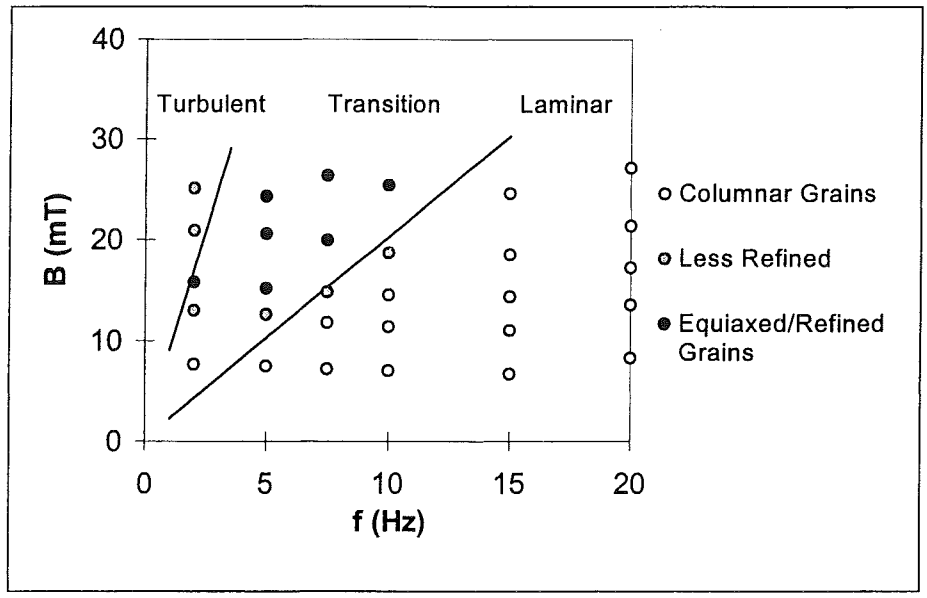

Fig. 4.30. The relationship between the magnetic field strength and the stirring frequency that gives different modes of fluid flow and its corresponding microstructure of the stirred AA 6060 thick plate CPT welds.

Chapter 5. Conclusions and Recommendations

5.1. Conclusions

In this thesis, a systematic study dealing with the influence of electro-magnetic stirring (EMS) on the weld microstructure of AA6xxx series is presented. On the basis of the results obtained from both the experiments and the proposed fluid velocity model, the following conclusions can be drawn:

1. EMS of the weld pool in the AA 6xxx series lead to a grain refining effect. In agreement with the results of other studies, optimal grain refinement was obtained in a particular range of stirring frequency and magnetic field strength.

2. The optimal results of grain refining were indicated to be obtained when the fluid flow in the weld pool becomes turbulent. The model proposed indicates that to get an optimum grain refining effect and thus an effective fluid flow, besides stirring frequency and magnetic field strength, welding current and weld pool radius are also important.

3. There is a strong indication that the shape of the weld pool determines the depth of the grain refining effect of EMS. In a cylindrical weld pool (fully penetrated weld), the grain refining effect could be found from the weld surface down to the bottom of the weld pool while in a spherical weld pool (partially penetrated weld) the effect is limited only to a certain distance from the weld pool surface.

4. The Circular Patch test (CPT) can create reproducible hot cracking. The cracks were not only developed as a surface crack but also as a sub-surface crack and even developed at the weld root.

5. Straight welding of thick AA 6060 plates also displayed hot cracking even though not as severe as that demonstrated in CPT. Furthermore, it was found that hot cracking in straight welding of AA 6060 thin plates was welding parameter dependent. However, on the AA 6060 thin plate welds that experience hot cracking, it appears that EMS improves the hot

cracking resistance. Further investigation on the relationship between the stirring parameter and the hot cracking sensitivity is required.

6. As far as hot cracking in AA 6060 and AA 6061 is concerned, EMS did not demonstrate reduction of hot crack sensitivity in CPT though some degree of grain refining was found. This is most likely due to the relatively high restraint in CPT.

7. Verified by SEM, the hot cracking was marked as an intergranular crack. The weld crack surface had a smooth grain boundary with broken flakes-like of solute-rich or eutectic substance spread on it.

8. Temperature measurements of the weld pool indicated that the nominal temperature gradient G of the weld pool stirred with low stirring frequency was more reduced than the nominal G of the weld pool stirred at high frequency. This might prove that during high frequency stirring, the fluid velocity in the weld pool is lower (the mixing of the hotter and the cooler liquid is less extensive) compared to that at low frequency.

5.2. Recommendations

As discussed in this thesis, the grain refinement effect due to electro-magnetic stirring during TIG welding might be obtained when the fluid flow in the weld pool becomes turbulent. Further research should therefore be focused on the following topics:

1. Investigate the exact flow patterns within the weld pool as a means to verify the model proposed. The use of a mercury bath [20] and a high-speed camera might prove to be useful.

2. Solve the fluid flow model in the weld pool by taking into account the alternating magnetic field (B as a function of r and t). Besides, a solution of the three dimensional Navier-Stokes equation might give a more precise prediction of the fluid flow in the weld pool.

3. Study whether grain detachment or dendrite fragmentation does exist during EMS. A method used by Kou [15] might be beneficial to use.

4. Study the possibility of using a constant magnetic field during AC welding (where f = 50 Hz) with high magnetic field strength.

5. Continue to study on the relationship between the hot cracking and the stirring parameters.

6. Study the effect of EMS on the local temperature gradient G at the fusion boundary, i.e. where the solidification proceeds.

Reference

1. D.C. Brown, F.A. Crossley, J.F Rudy and H. Schwartzbart, *The Effect of Electromagnetic Stirring and Mechanical Vibration on Arc Welds*, Welding Journal, 41, pp. 241s-250s, 1962.
2. G.J. Davies and J.G. Garland, *Solidification Structures and Properties of Fusion Welds*, Int. Metall. Rev., 20, pp. 83-106, 1975.
3. C.H.J. Gerritsen, *Low Frequency Electro-Magnetic Stirring during AC Tig Welding of AA6082*, Master's Thesis, Delft University of Technology, March 1999.
4. Hindrik de Vries, *Weldability of Aluminium-Matrix Composites*, Ph.D. Thesis, Delft University Press, 1998.
5. R.L. O'Brien, *Welding Processes, Welding Handbook*, Vol. 2, AWS, Miami FL, 1995.
6. R.W. Messler Jr., *Joining of Advanced Material*, Butterworth-Heineman, Stoneham, MA, 1993.
7. G. den Ouden, *Lastechnologie*, Delft University of Technology, 1990.
8. M.G. Mousavi, *Grain Refinement and Hot Cracking Resistance of Aluminium Weldments*, Ph.D. Thesis, The Norwegian University of Science and Technology (NTNU), 1999.
9. R.W. Messler Jr., *Principle of Welding*, Butterworth-Heineman, Stoneham, MA, 1993.
10. S. Kou, *Welding Metallurgy*, John Wiley & Sons Inc., New York, 1987.
11. T. Ganaha, B.P. Pearce, and H.W. Kerr, *Grain Structures in Aluminum Alloy GTA Welds*, Metallurgical Transactions A, 11A, pp. 1351-1359, August 1980.
12. W. Kurz, D.J. Fisher, *Fundamentals of Solidification*, Trans Tesch Publications Ltd., Switzerland, 1992.
13. W.F. Savage, *Solidification, Segregation and Weld Imperfection*, Welding in the World, 18, 5/6, pp. 89-114, 1980.

14. Øystein Grong, *Metallurgical Modelling of Welding,* Second Edition, The Institute of Materials, The Univesity Press, Cambridge, 1997.

15. S. Kou and Y. Le, *Nucleation Mechanism and Grain Refining of Weld Metal*, Supplement to the Welding Journal, pp. 305s-146s, December 1986.

16. S. Kou and Y. Le, *Welding Parameter and the Grain Structure of Weld Metal-A Thermodynamic Consideration*, Metallurgical Transaction A, 19A, pp. 1075-1082, April 1988.

17. J.C. Villafuerte and H.W. Kerr, *Electromagnetic Stirring and Grain Refinement in Stainless Steel GTA Welds*, Supplement of the Welding Journal, pp. 1s-13s, January 1990.

18. S.A. David and J.M. Vitek, *Correlation between Solidification Parameters and Weld Microstructure*, International Material Reviews, 34, 5, pp. 213-245, 1989.

19. B.T.J. Stoop, T. Luyendijk and G. den Ouden, *Structure and Properties of GTA Welds in Aluminium Alloys*, Welding & Metal Fabrication, pp. 420-423, October 1989.

20. F. Matsuda, H. Nakagawa, K. Nakata and R. Ayani, *Effect of Electromagnetic Stirring on Weld Solidification Structure of Aluminum Alloys (Report I) – Investigation on GTA Weld Metal of Thin Sheet*, Transaction of JWRI, 7, 1, pp. 111-127, 1978.

21. Matsunawa, *Modeling of heat and fluid Flow in Arc Welding*, In: *International Trends in Welding Science and Technologically,* Proceeding of the 3rd International Conference on Trends in Welding Research, Gatlinburg, pp. 3-16, June 1992.

22. Sindo Kou, *Transport Phenomena and Materials Processing*, John Wiley & Sons Inc., 1996.

23. D.R. Poirier and G.H. Geiger, *Transport phenomena in Materials Processing*, TMS, Warrendale, Pennsylvania, 1994.

24. M. Malinowski-Brodnicka, G. den Ouden and W.J.P Vink, *Effect of Electromagnetic Stirring on GTA Welds in Austenitic Stainless Steel*, Welding Journal, 69, 2, pp. 52s-59s, 1990.

25. F. Matsuda, K. Nakata, N. Sano, *Effect of Electromagnetic Stirring on Weld Solidification Structure of Austenitic Stainless Steels*, Transaction of JWRI, 15, 2, pp. 155-166, 1986.

26. B.P. Pearce and H.W. Kerr, *Grain Refinement in Magnetically Stirred GTA Welds of Aluminium Alloys*, Metallurgical Transaction B, 12B, pp. 479-486, September 1981.

27. V.P. Chernysh, V.D. Kuznetsov and E.V.Turyk, *Variation in the Temperature State of the Weld Pool during Electromagnetic Stirring*, Avt. Svarka, 7, pp. 3-6, 1976.

28. T. Watanabe, H. Nakamura and K. Ei, *Solidification Control of Austenitic Stainless Steel Weld Metal by Electromagnetic Stirring*, Transaction of the Japan Welding Society, 21, 2, pp. 37-43, 1990.

29. F. Matsuda, K. Nakata, K. Tsukamoto and T.Uchiyama, *Effect of Additional Element on Weld Solidification Crack Susceptibility of Al-Zn-Mg Alloy (Report III)-Enhancement of Beneficial Effect of Zirconium on Improvement of Crack Susceptibility by Application of Electromagnetic Stirring*, Transaction of JWRI, 13, 1, pp. 57-66, 1984.

30. F. Matsuda, K. Nakata, Y. Miyanaga, T. Kayano and K. Tsukamoto, *Effect of Electromagnetic Stirring on Weld Solidification Structure of Aluminum Alloys (Report II) – Investigation on GTA in DSCP Weld Metal 8 mm Thick plate*, Transaction of JWRI, 7, 2, pp. 181-193, 1978.

31. E.L. Rooy, *Properties and Selection: Non Ferrous Alloys and Special Purpose Materials*, ASM Handbook, Vol 2, ASM International, 1998

32. B. Irving, *Welding the Four Most Popular Aluminium Alloys*, Welding Journal, 51, pp. 31-41, February 1997.

33. J.C. Borland, and J.H. Rogerson, *Examination of the Patch Test for Assessing Hot Cracking Tendencies of Weld Metal*, British Welding Journal, 8, pp. 494-499, 1963.

34. T.W. Nelson, J.C. Lippold, W. Lin, and W.A. Baeslack III, *Evaluation of the Circular Patch Test for assessing Weld Solidification Cracking, Part 1- Development of a Test Method*, Welding Research Supplement, pp. 110s-119s, 1997.

35. A.M. Boldyrev and E.B.Dorofeev, *The Selection of the Design of the Solenoid for the Electromagnetic Treatment of the Weld Pool*, Svar. Proiz., 10, pp. 48-50, 1977.

36. E.M. Purcell, *Electricity and Magnetism*, Berkeley Physics Course, McGraw-Hill Company, 1985.

37. W.E. Boyce and R.C. DiPrima, *Elementary Differential Equation and Boundary Value Problems*, John Wiley & sons, Inc. New York, 1997.

38. R.L. Mott, *Applied Fluid Mechanics*, Prentice Hall, NJ, Ohio, 1990.

Appendix 1
Photomicrographs of CPT AA6060-T6 Weld

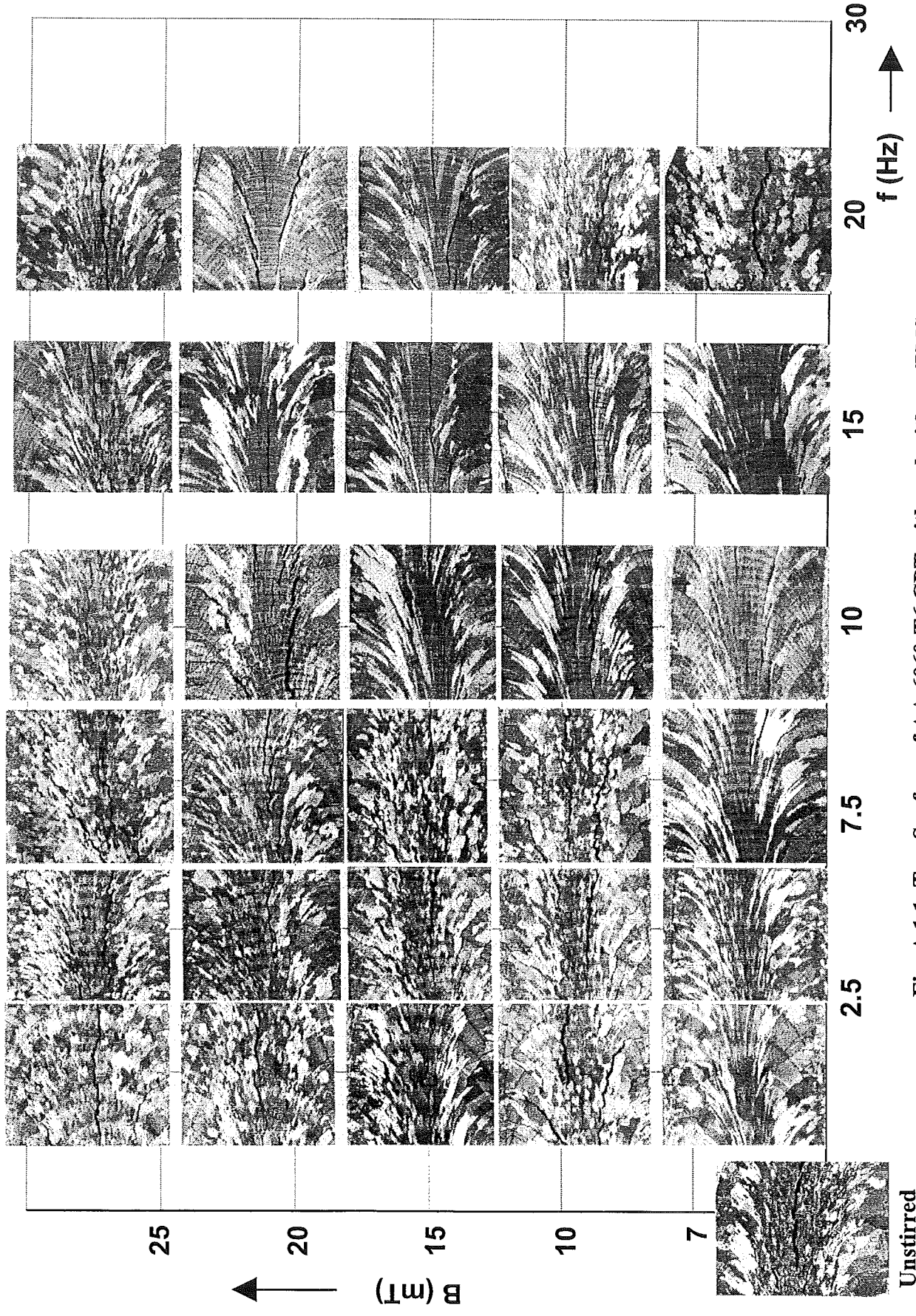

Fig. A.1.1. Top Surface of AA 6060-T6 CPT with and without EMS.

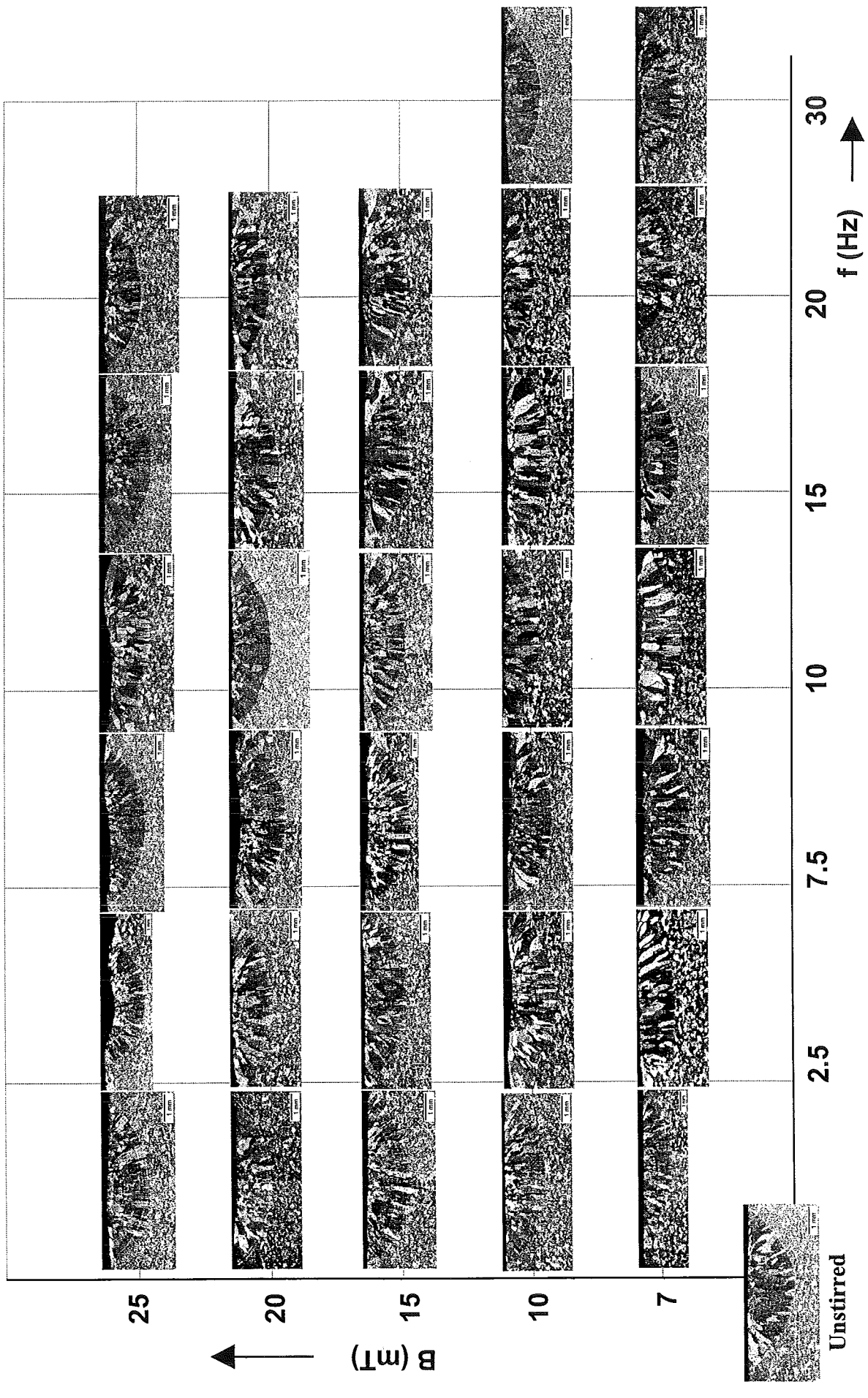

Fig. A.1.2. Transverse Cross Section of AA 6060-T6 CPT with and without EMS.

Appendix 2

Photomicrographs of Straight Weld of AA6060-T6 Thin Plate

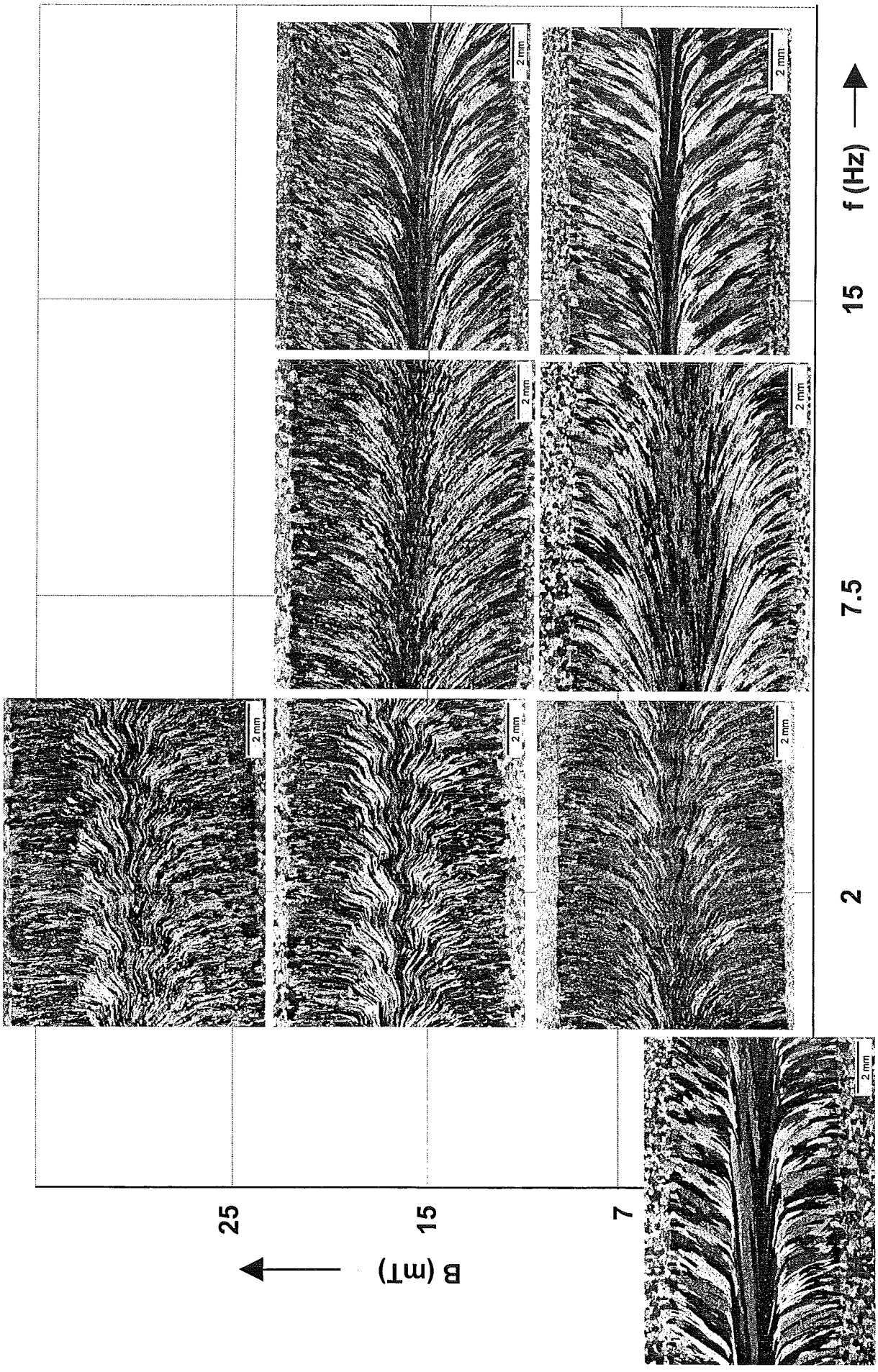

Fig. A.2.1 Top surface of AA 6060-T6 thin plate welds with and without EMS.

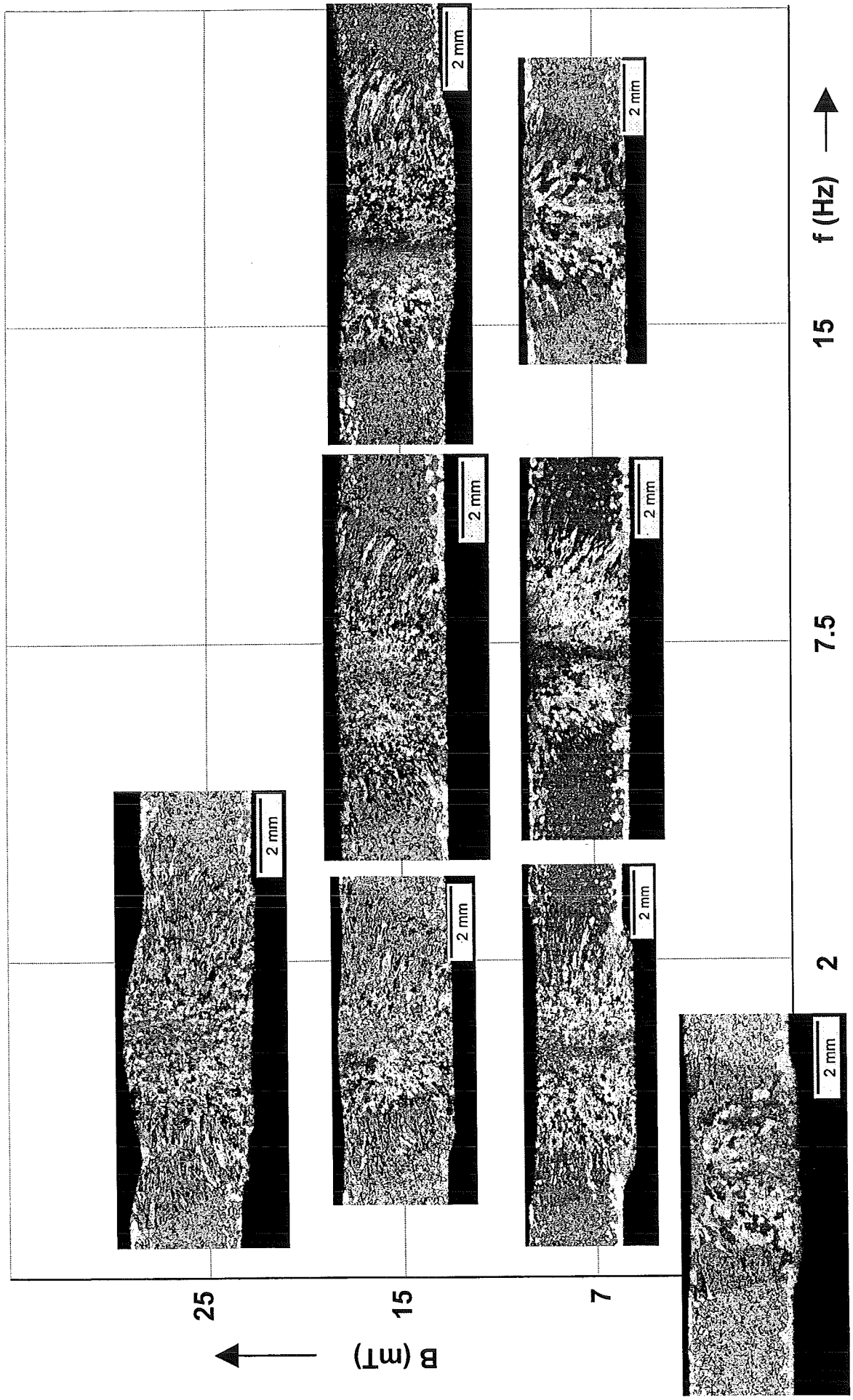

Fig. A.2.2. Transverse cross section of AA 6060-T6 thin plate weld with and without EMS.

Appendix 3
Photomicrographs of Straight Weld of AA6061 Thick Plate

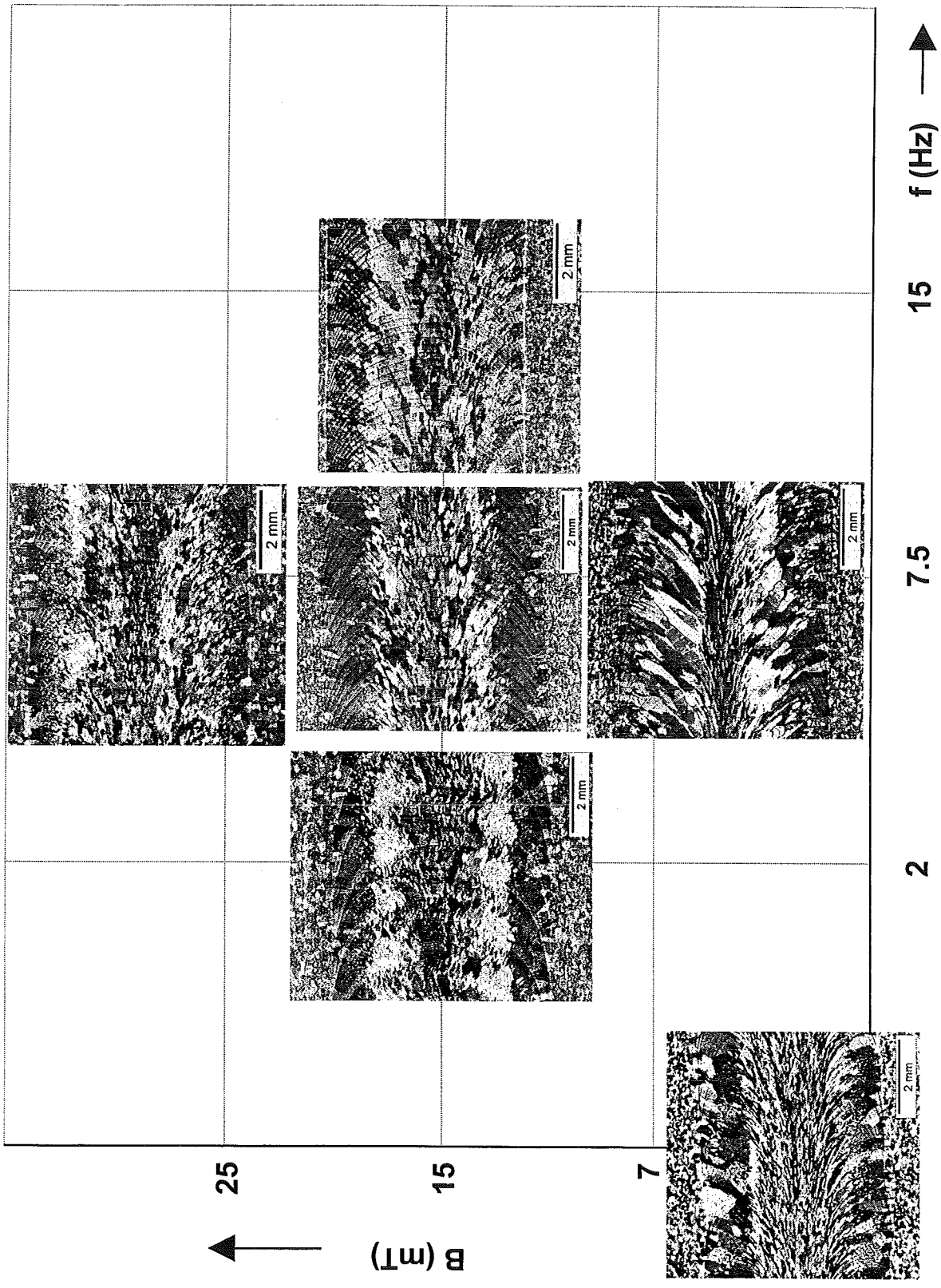

Fig. A.3.1. Top surface of AA 6061 thick plate welds with and without EMS.